Experimental Determination of the ^{8}B Neutrino Spectrum

by

Wesley Thomas Winter

B.S., Physics (University of Illinois) 1998
B.S., Mathematics (University of Illinois) 1998
M.A., Physics (University of California) 2000

A dissertation submitted in partial satisfaction
of the requirements for the degree of

Doctor of Philosophy

in

Physics

in the

GRADUATE DIVISION

of the

UNIVERSITY OF CALIFORNIA, BERKELEY

Committee in charge:

Professor Stuart J. Freedman, Chair
Professor Hitoshi Murayama
Professor Eugene E. Haller

Spring 2007

The dissertation of Wesley Thomas Winter is approved.

_____
Chair   Date

_____
Date

_____
Date

University of California, Berkeley

Spring 2007

Experimental Determination of the ^{8}B Neutrino Spectrum

Abstract

Experimental Determination of the ^{8}B Neutrino Spectrum

by

Wesley Thomas Winter

Doctor of Philosophy in Physics

University of California, Berkeley

Professor Stuart J. Freedman, Chair

Knowledge of the energy spectrum of ^{8}B neutrinos is an important ingredient for interpreting experiments that detect energetic neutrinos from the Sun. The neutrino spectrum deviates from the allowed approximation because of the broad alpha-unstable ^{8}Be final state and recoil order corrections to the beta decay. I have measured the total energy of the alpha particles emitted following the beta decay of ^{8}B. The spectrum measured here is inconsistent with a previous measurement of comparable precision, but is in good agreement with a subsequent measurement. The alpha energy spectrum is fit using the R-matrix approach, which gives a functional form for the beta decay strength function for the transition from ^{8}B to the ^{8}Be resonance. The with

Professor Stuart J. Freedman
Dissertation Committee Chair

1

Contents

3   The ^{8}Be Final State: An R-matrix Description   58

4   Previous Measurements of the ^{8}B β-delayed Alpha Spectrum   69

5   The Alpha Spectrum Measurement   87

List of Figures

List of Tables

Chapter 1

Solar Neutrinos: Origin and Detection

Over a half century has passed since scientists first detected neutrinos emitted by the Sun. Unlike photons, which are easily detectable and scatter repeatedly as they traverse the solar volume, neutrinos are weakly interacting. Neutrinos pass mostly unhindered from the Solar core to detectors deep within the Earth, where only a tiny fraction of the neutrino flux is observed. Originally, it was thought that these neutrinos would be unchanged from the moment of their creation as byproducts of the nuclear fusion processes that drive the Sun. By studying these neutrinos scientists would, in essence, be looking directly into the solar core.

Using solar neutrinos to study the process of solar fusion is simple in principle. However, the experimental implementation was difficult and the initial results were inconclusive. The desire to solve these problems fueled a massive effort across several branches of physics. Laboratory measurements of nuclear reactions were performed with ever-increasing precision. Theoretical models of the Sun, using experimental nuclear data as inputs, became more sophisticated. Helioseismology, the study of surface sound waves on the Sun, was developed and from it came measurements that verified the solar models. Concurrently, solar neutrino detection advanced as experimental techniques were improved and new detection methods were implemented. Despite the advances, results from solar neutrino detection experiments remained inconsistent with theoretical

predictions. Even more puzzling, experiments with different neutrino energy thresholds were inconsistent with one another. These discrepancies became known as the **solar neutrino problem**.

Considering the effort devoted to solving the solar neutrino problem, it is gratifying that the solution is nontrivial; it has changed scientists' views of neutrinos themselves and the fundamental theories that describe their behavior. The problem is not fully solved; new questions have been raised and discoveries in the area of neutrino physics continue to be made.

This thesis deals primarily with a new laboratory measurement involving the nuclear decay of ^{8}B, an isotope produced in the Sun. This decay provides a majority of the neutrinos detected in Solar neutrino experiments so far. Some implications of this measurement are discussed. This initial chapter provides a description of the solar nuclear fusion reactions from which neutrinos are created, various methods of detecting these neutrinos, and an introductory look at the ^{8}B isotope and its decay.

1.1 Nuclear Fusion and Beta Decay in the Solar Core

The Sun, 150 million kilometers from Earth, is the dominant source of energy for all atmospheric and surface activity on the planet. Its enormous energy output, 4×10^{26} Watts, results from the fusion of light nuclei. Fusion occurs only in the solar core, the central region of the Sun, comprising $\sim$1% of its total volume. Here temperatures reach up to 15 million degrees Kelvin. The particular process responsible for most of the Sun's power, known as hydrogen burning, is a sequence of exothermic fusion reactions that transforms four protons into an alpha particle. Hydrogen burning, and other nuclear fusion processes occurring in the solar core, produce the solar neutrinos detected on Earth.

1.1.1 Fundamental Principles of Solar Fusion Processes

Solar models attempt to describe the many facets of solar energy production in terms of nuclear fusion reactions. They are detailed in both their theoretical construction and experimental

inputs. The basic ideas behind solar fusion and solar neutrino production, however, may be understood employing only a few fundamental principles of physics. These principles, and some of their implications, are listed below:

Conservation of Energy A central tenet of both modern and classical physics, this principle is certainly applicable to solar fusion. In all the nuclear reactions occurring in the solar core, energy is conserved.

Mass-Energy Equivalence Introduced by Einstein in 1905, the relation between mass and energy is crucial to an understanding of solar fusion. As an example, for the reaction that produces an α particle from two lighter ^{3}He nuclei,

$$^3He + {}^3He \rightarrow \alpha + 2p \tag{1.1}$$

the total mass of the ^{3}He nuclei in the initial state ($m_i = 5616.78$ MeV/c^2) is greater than the mass of the α particle and protons in the final state ($m_f = 5603.89$ MeV/c^2) by $\Delta m = m_i - m_f = 12.89$ MeV/c^2. To conserve energy, the final state products must possess kinetic energy of magnitude $\Delta E = \Delta mc^2 = 12.89$ MeV.

Decrease of Nucleon Mass with Increasing Atomic Number The binding between individual nucleons inside a nucleus is provided by the **strong interaction**. The strength of the bond is given by the mass difference between a nucleus and its constituent nucleons, multiplied by c^2. Tightly bound nuclear systems will have a smaller mass per nucleon than more loosely bound systems. An empirical result of nuclear physics is that for a nucleus of mass M and atomic number A there is a general decrease in the mass per nucleon M/A as A increases. This trend holds up to ^{56}Fe, which has the most tightly bound nucleons. The ratio M/A for some nuclei involved in solar fusion is plotted as a function of A in Fig. 1.1.

The decrease of M/A with increasing A shows that when lighter nuclei are fused to form heavier nuclei, an amount of energy (of order MeV) must be released in the form of kinetic or electromagnetic energy. Hydrogen burning, which accounts for the great majority of the Sun's energy output, is a process by which four protons fuse into an α particle. As illustrated in Fig. 1.1, the tightly-bound α particle resides at a local minimum of M/A. Furthermore, all nuclei with
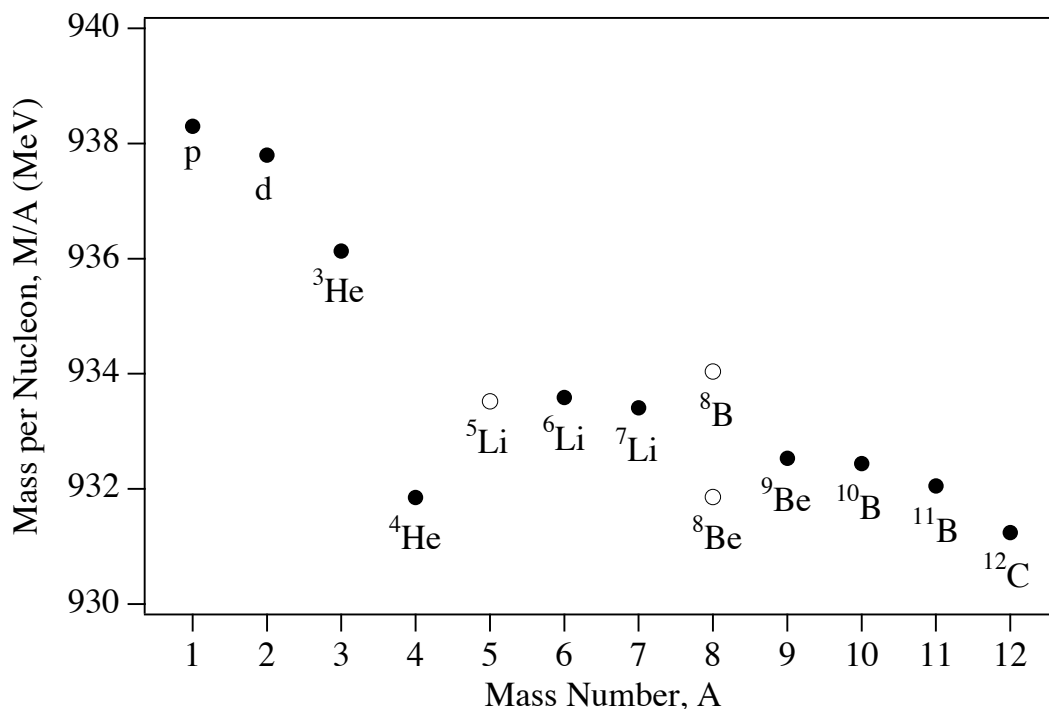
Figure 1.1. The mass per nucleon for many of the nuclei involved in solar fusion processes. Unshaded circles indicate unstable nuclei. Note that there are no stable nuclei for $A = 5$ and 8.

$A = 5$ are unstable (^{5}He and ^{5}Li decay immediately to an α particle and a free nucleon). These properties conspire to make the α particle a waiting point in the solar fusion chain.

The importance of nuclear binding energy in solar fusion reactions can be seen by considering the ^{3}He+^{3}He reaction. All possible nuclear products and the energy release associated with the reaction are shown in Table 1.1. The only exothermic reaction is the α-producing fusion process shown in Eq. 1.1. The reactions with negative energy release represent fission processes, where the ^{3}He nucleus dissociate into smaller constituents. These fission reactions are energetically inaccessible given the relatively small thermal energies (a few keV) of nuclei in the Sun. The important result that fusion processes drive the Sun is a result of the decrease of M/A for increasing A.

Conservation of Baryon Number Baryon number, defined as $+1$ for nucleons and -1 for antinucleons, is a conserved quantity for both the strong and weak interactions. Processes in the Sun

Product Nuclei	Energy Release
^{4}He + 2 p	12.850 MeV
^{3}He + ^{3}He	0 MeV
^{3}He + p + d	-5.50 MeV
t + 3 p	-6.97 MeV
^{3}He + 2 p + n	-7.73 MeV
2 d + 2 p	-10.99 MeV
3 p + n + d	-13.23 MeV
4 p + 2 n	-15.46 MeV

Table 1.1. Possible final states for the reaction ^{3}He+^{3}He, and their associated energy releases. Negative energy releases indicate endothermic reactions.

are generally not energetic enough to produce anti-nucleons (in any case, an anti-nucleon would quickly annihilate with a nucleon), and resonances such as Δ-particles quickly de-excite back to a nucleon. Thus, the conservation of baryon number is equivalent to stating that the number of nucleons in the Sun is conserved.

Conservation of Electric Charge and Lepton Number Electric charge and lepton number are conserved quantities for both the strong and weak interactions. In nuclei, the fraction of nucleons which are protons, Z/A, decreases as A increases. Hence, as lighter nuclei are fused to form heavier nuclei in the Sun, protons are being converted to neutrons.

Conservation of charge requires that a positively charged particle must be emitted when a proton is converted to a neutron. In solar fusion reactions, the mass difference between the initial and final states is of order $1-10$ MeV (as seen in Fig. 1.1). The only positively charged particle light enough to be created in these processes is a positron, with mass 0.511 MeV/c^2, which is an anti-particle.

The conservation of lepton number explains the emission of neutrinos from the sun. Leptons are particles that do not participate in the strong interaction. Uncharged leptons are called neutrinos. The only charged leptons existing in the solar core are electrons and positrons, since heavier leptons are generally not energetically accessible. Lepton number, defined as +1 for leptons and -1 for anti-leptons, is a conserved quantity. Hence, as a proton is converted into a neutron and a positron, a neutrino must be emitted to conserve lepton number.

The fundamental processes of solar fusion, in which protons are converted to neutrons as heavier nuclei are formed, may be expressed as:

$$p \rightarrow n + e^+ + \nu_e \ (\beta \ decay) \tag{1.2}$$

and

$$p + e^- \rightarrow n + \nu_e \ (electron \ capture). \tag{1.3}$$
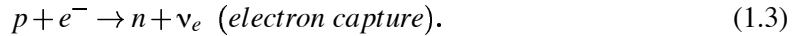
Fusion processes in the solar core utilize the $p \rightarrow n$ reaction and never the inverse. Hence positrons must be emitted to conserve charge, and neutrinos must be emitted to conserve lepton number. By a similar argument, the inverse process $n \rightarrow p$ requires the emission of electrons and *anti*-neutrinos. Note then that the Sun is pure source of neutrinos (no anti-neutrinos).

A further property of beta decay and electron capture is that for each interaction a quantum number called **flavor** is conserved. There are three types of charged leptons with their own individual flavors: electrons, muons, and taus. Electron flavor is defined as $+1$ for electrons and -1 for positrons. Therefore, at the moment of their creation solar neutrinos must have electron flavor $+1$ and they are termed electron-type neutrinos. The heavier charged leptons, with electron flavor 0, have their own quantum numbers and their own associated neutrinos.

The fundamental properties discussed above provide enough background for the basic hydrogen burning process to be understood. Hydrogen burning uses nuclear fusion to convert four protons into an alpha particle while also releasing positrons, neutrinos, gamma rays, and final state kinetic energy. The nuclear reactions contributing to the hydrogen burning process and their corresponding energy releases are shown in Table 1.2. The neutrino energy, which is about 7.5% of the total energy release, does not heat the Sun because nearly all neutrinos pass directly out of the Sun without interacting.

Initial Nuclei	$\longrightarrow$	Products	Energy Release	Average Neutrino Energy
$p + p$	$\longrightarrow$	$d + e^+ + \nu_e$	1.442 MeV	0.265 MeV
$p + p + e^-$	$\longrightarrow$	$d + \nu_e$	1.442 MeV	1.442 MeV
$d + p$	$\longrightarrow$	$^3\text{He} + \gamma$	5.494 MeV	–
$^3\text{He} + {}^3\text{He}$	$\longrightarrow$	$^4\text{He} + 2\,p$	12.860 MeV	–

Table 1.2. The fundamental reactions of the hydrogen burning nuclear fusion process. The energy releases from these reactions account for the vast majority of the Sun's power.

1.1.2 Nuclear Reaction Rates and Solar Time Scales

As described in the previous section, the Sun's massive energy output results from the fusion of light nuclei into heavier ones. For two nuclei to fuse via the strong interaction, the electric Coulomb barrier between the nuclei must be overcome. As an example, again consider the reaction where two ^{3}He nuclei fuse to form an α particle (Eq. 1.1). If the strong interaction overcomes the Coulomb repulsion when the ^{3}He nuclei are separated by distances $r < 2r_3$ (hard-sphere interaction), the height of the Coulomb energy barrier E_{Coul} is,

$$E_{Coul} = \frac{1}{4\pi\varepsilon_0} \frac{(2e)^2}{2r_3} \approx 3 MeV.$$

(1.4)

Where the radius of ^{3}He is taken to be $r_3 = 2$ fm.

The Coulomb energy barrier is much higher than the kinetic energy of ^{3}He nuclei in the Sun. The high temperatures in the Sun are a result of gravitational pressure and they reach $T_{max} = 1.6 \times 10^7$ K in the solar core. A typical energy for ^{3}He nuclei in the core is thus $k_B T_{max} = 1.4$ keV, and the distribution of energy among ^{3}He nuclei is well-described by a classical Boltzmann distribution. The situation in the Sun is markedly different from the conditions at nuclear accelerators, where nuclei are accelerated to energies comparable to the Coulomb barrier. In general, any nuclear reaction occurring in the Sun must result from quantum mechanical tunneling of low energy ($\sim$1 keV) nuclei through the large ($\sim$1 MeV) Coulomb barrier.

There are four main points one must consider in calculating nuclear reaction rates: (1) The probability that a nucleus has a given thermal energy, (2) the rate of collisions that such a nucleus experiences, (3) the probability that this collision leads to penetration of the Coulomb barrier,

and (4) the probability that a reaction takes place after barrier penetration occurs. These steps are discussed in order below:

(1) Maxwell-Boltzmann Distribution As discussed above, the temperatures in the Sun are sufficiently high that a classical Boltzmann distribution may be used. Thus, the probability that a state with energy E will be occupied is proportional to the Boltzmann factor $exp(-E/k_B T)$. Accounting for the density of states at a given energy, the probability $f(E)$ that a particle has energy E is given by

$$f(E) = \frac{2}{\sqrt{\pi}} \frac{1}{(k_B T)^{3/2}} \sqrt{E} exp\left(-\frac{E}{k_B T}\right).$$

(1.5)

(2)Frequency of Collisions Earlier in this section the ^{3}He nucleus was considered to have a radius of 2 fm. This value was assigned on the basis that the nucleon radius is about 1.4 fm and that the nuclear size grows as $A^{1/3}$. For calculations of barrier penetration, this is an appropriate value to use. However, in considering the collision rate between nuclei a different length scale must be invoked. In this approximation the nucleus is given an associated length scale, λ, defined as follows: When nuclei are separated by distances less than λ they experience a collision, thus the possibility of tunneling through the Coulomb must be considered. When nuclei are separated by distances greater that λ, there is no possibility of interaction. It is reasonable to define λ as the de Broglie wavelength,

$$\lambda = \frac{h}{p},$$

(1.6)

where p is the momentum of the nucleus. Note that the de Broglie wavelength of a typical light nucleus in the Sun is of order 0.1 nm, roughly 100 times larger than the nuclear size.

Using the hard-sphere scattering approximation and working in the center-of-mass reference frame, the collision rate per unit time and volume, N, is given by

$$N = \frac{\pi \lambda^2 v n_1 n_2}{1 + \delta_{12}},$$

(1.7)

where v is the relative velocity of the nuclei and $n_{1,2}$ are the number densities of the colliding nuclei. The Kronecker delta function ($\delta_{ij} = 1$ when $i = j$ and $\delta_{ij} = 0$ when $i \neq j$) is included to prevent double counting when collisions between identical nuclei are considered. Incorporating

the Maxwell-Boltzmann distribution (Eq. 1.5) yields the probability that a nucleus has a given energy. Expressing Eq. 1.7 in terms of energy gives

$$\frac{dN}{dE} = \frac{\sqrt{2\pi}\hbar^2 n_1 n_2 exp(-\frac{E}{k_B T})}{(Mk_B T)^{3/2}(1+\delta_{12})}, \tag{1.8}$$

where dN/dE is number density of collisions for a given range of energies in the solar core.

(3) Coulomb Barrier Penetration In general, for two nuclei with charges Z_1 and Z_2, a reduced mass M, and relative energy E, the probability P of tunneling through the Coulomb barrier to nuclear separation R may be calculated using the WKB approximation and by making some simplifying approximations. This method was first employed by Gamow to describe α decay [1]. The result is

$$P = e^{-2\pi\eta}, \tag{1.9}$$

where

$$\eta = \frac{Z_1 Z_2 e^2 \sqrt{2M}}{8\pi\varepsilon_0 \hbar} \frac{1}{\sqrt{E}} - \frac{1}{\hbar}\left(\frac{2MZ_1 Z_2 e^2}{\pi^3 \varepsilon_0}\right)^{1/2}\sqrt{R} \tag{1.10}$$

is called the Gamow penetration factor. The thermal energies in the Sun are sufficiently low so that the first term in Eq. 1.10 is much larger than the second term. The second term is thus ignored to simplify the discussion.

The rate of nuclear interactions as a function of energy is then given by the product of the rate of collisions dN/dE and the probability of barrier penetration $exp(-2\pi\eta)$. Fig. 1.2 shows these exponential functions, one increasing and one decreasing with energy. The resulting product is a broad, nearly symmetric function, also shown in Fig. 1.2. The peak of this function, called the Gamow Peak, is located near 30 keV, well above the average thermal energy $\frac{3}{2}k_B T \approx 1.4$ keV, indicating that most solar fusion events result from interactions between nuclei on the high energy tail of the Maxwell-Boltzmann distribution.

(4)Probability of Nuclear Reaction All that remains in determining the nuclear reaction rate is to calculate the probability that a given reaction occurs once the barrier is penetrated.

To simplify discussion, some new terms will be defined. First, consider the rate of hard-sphere interactions per unit volume, Eq. 1.7, multiplied by the probability of barrier penetration,

9
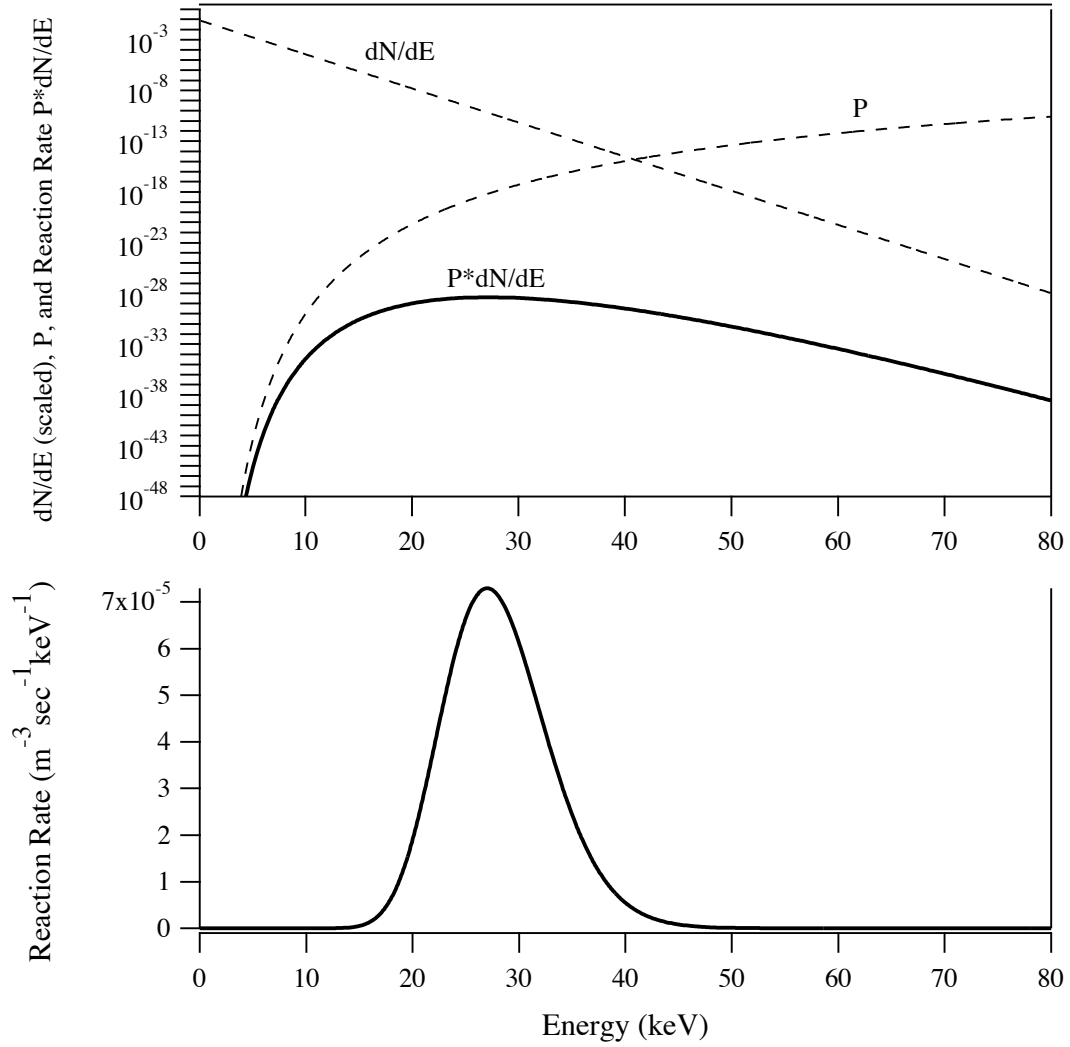
Figure 1.2. (Top panel) The density of nuclear collisions, dN/dE, and the probability of barrier penetration, $exp(-2\pi\eta)$, are shown for the example case of ^{3}He-^{3}He interactions, and their functional forms are indicated. The product of the functions, which gives the rate of nuclear reactions as a function of energy, is shown. (Bottom panel) Here the product is shown on a linear scale to emphasize the features of the curve. The maximum of the curve is called the Gamow peak.

Eq. 1.9,

$$N \cdot P = \frac{\pi\lambda^2 v n_1 n_2}{1+\delta_1\delta_2}e^{-2\pi\eta} = \left(\frac{2\pi^3\hbar^2}{mE}e^{-2\pi\eta}\right)\frac{v n_1 n_2}{1+\delta_1\delta_2}, \qquad (1.11)$$

where the definition of the de Broglie wavelength, Eq. 1.6, is used. The right hand side of Eq.

1.11 suggests that the factors within the parentheses be considered as a cross section, σ, where

$$\sigma = \frac{2\pi^3 \hbar^2}{mE} e^{-2\pi\eta}. \tag{1.12}$$

This cross section contains the physics of both collision frequency and barrier penetration. In literature dealing with nuclear cross sections the replacement

$$\frac{2\pi^3 \hbar^2}{m} \approx 1 \ keV \cdot b \rightarrow S(E) \tag{1.13}$$

is made, so that the cross section appears as

$$\sigma = \frac{S(E)}{E} e^{-2\pi\eta}. \tag{1.14}$$

The newly defined astrophysical S-factor, $S(E)$, contains all the nuclear physics not previously considered. The S-factor is typically measured in laboratory experiments because it is often difficult, or impossible, to calculate. In practice, the Coulomb barrier is so difficult to overcome that the S-factor is typically only determined down to a few hundred keV, and an extrapolation to solar energies must be performed. Models [2] have been suggested to guide the extrapolation process, and it remains an active area in nuclear astrophysics to measure the S-factor for energies as low as possible.

———

Combining the results of the arguments above, the rate density, N_{fusion}, for solar fusion processes is given by

$$N_{fusion} = \frac{\langle \sigma v \rangle n_1 n_2}{1 + \delta_1 \delta_2}, \tag{1.15}$$

where $\langle \sigma v \rangle$ is the mean value of the cross section multiplied by velocity, weighted by the Maxwell-Boltzmann distribution,

$$\langle \sigma v \rangle = \left(\frac{8}{\pi M k_B^3 T^3} \right)^{1/2} f_0 \int_0^\infty dE S(E) exp(-\frac{E}{k_B T} - 2\pi\eta). \tag{1.16}$$

The quantity f_0 is accounts for the increase in reaction rate due to the screening of nuclear charge by free electrons. This quantity was introduced and approximated [3] in 1954 and has recently

Reaction	Q (MeV)	$\langle E_\nu \rangle$ (MeV)	S_0 (keV·barns)	t (years)
$p + p \rightarrow d + e^+ + \nu_e$	1.442	0.265	$(4.07 \pm 0.21) \times 10^{-22}$	10^{10}
$p + p + e^- \rightarrow d + \nu_e$	1.442	1.442		10^{12}
$d + p \rightarrow {}^3He + \gamma$	5.494		2.5×10^{-4}	10^{-8}
${}^3He + {}^3He \rightarrow \alpha + 2\,p$	12.860		$(5.15 \pm 0.98) \times 10^3$	10^5
${}^3He + p \rightarrow \alpha + e^+ + \nu_e$	19.795	9.625	8×10^{-20}	10^{12}
${}^3He + {}^4He \rightarrow {}^7Be + \gamma$	1.442	1.442	0.54 ± 0.03	10^{12}
${}^7Be + e^- \rightarrow {}^7Li + \nu_e$	0.862	0.862		10^{-1}
	0.384	0.384		
${}^7Li + p \rightarrow 2\,\alpha$	17.374		52 ± 25	10^{-5}
${}^7Be + p \rightarrow {}^8B + \gamma$	0.137		0.0243 ± 0.001	10^2
${}^8B \rightarrow {}^8Be^* + e^+ + \nu_e$	17.980	6.710		10^{-8}
${}^8Be \rightarrow 2\,\alpha$				

Table 1.3. Reactions associated with the proton-proton chain. The Q-values, average neutrino energies, S-factors, and time scales of the reactions are indicated. This table was motivated by a similar table in Ref. [5], which also contains references to the experimental data.

been subject to a more thorough treatment involving numerical solutions of the Schrödinger equation [4].

The main result of this section is the rate of fusion, Eq. 1.15. The partial lifetime of a type-1 nucleus, T_1, in the presence of type-2 nuclei follows easily:

$$T_1 = \frac{1 + \delta_{12}}{n_2 \langle \sigma v \rangle_{12}}. \tag{1.17}$$

1.1.3 Solar Fusion Processes and Emitted Neutrinos

In the previous section the plausibility of solar nuclear reactions was established, and the reaction rates were estimated from basic physical arguments. In this section details of the solar fusion chains will be presented, with an emphasis on the nature of the emitted neutrinos.

Specifics of reactions occurring in the *p-p* chain are given in Table 1.3. The cross sections have been determined by experiment and are given as S-factors extrapolated to zero energy, S_0. Approximate timescales of the reactions are calculated using Eq. 1.17. This equation is implicitly dependent on the relative abundances of nuclear species and on the temperature variation throughout the Sun. These variables are determined using the Standard Solar Model [6]. For

Reaction	Q (MeV)	$\langle E_\nu \rangle$ (MeV)	S_0 (keV· barns)	t (years)
$^{12}C + p \rightarrow {}^{13}N + \gamma$	1.943		$(4.07 \pm 0.21) \times 10^{-22}$	10^{10}
$^{13}N + e^+ \rightarrow {}^{13}C + \nu_e$	2.221	0.707		10^{12}
$^{13}C + p \rightarrow {}^{14}N + \gamma$	7.551		2×10^{-4}	10^{-8}
$^{14}N + p + \gamma \rightarrow {}^{15}O + \gamma$	7.297		$(5.15 \pm 0.98) \times 10^3$	10^5
$^{15}O \rightarrow {}^{15}N + e^+ + \nu_e$	2.754	0.997	8×10^{-20}	10^{12}
$^{15}N + p \rightarrow {}^{16}O + \gamma$	12.128		0.54 ± 0.03	10^{12}
$^{15}N + p \rightarrow {}^{12}C + \alpha$	4.966			10^{-1}
$^{16}O + p \rightarrow {}^{17}F + \gamma$	0.600		52 ± 25	10^{-5}
$^{17}F \rightarrow {}^{17}O + e^+ + \nu_e$	2.762	0.999	0.0243 ± 0.001	10^2

Table 1.4. Reactions associated with the CNO chain. The Q-values, average neutrino energies, S-factors, and time scales of the reactions are indicated. This table was motivated by a similar table in Ref. [5], which also contains references to the experimental data.

reactions that emit neutrinos, the average neutrino energy is given. Note that β-decays produce a broad neutrino spectrum because the decay energy is shared between two leptons. In contrast, electron capture reactions produce monoenergetic neutrino lines.

It was previously stated that, with the creation of an α-particle at $A = 4$, the *p-p* chain reaches a waiting point. As seen in Table 1.3, the

$$^3He + {}^4He \rightarrow {}^7Be + \gamma \tag{1.18}$$

reaction allows a path for fusion to continue to heavier elements. This reaction is important in the context of solar neutrinos, since it leads to a concentration of ^{8}B that produces relatively high energy neutrinos.

The CNO cycle is a second fusion chain that, in addition to the dominant *p-p* chain, powers the Sun. Details of the CNO cycle are shown in Table 1.4. In the CNO cycle, as in the *p-p* chain, energy production arises from the fusion of four protons into an α-particle. The presence of C, N, and O nuclei merely act as catalysts for the reaction. In the Sun, the CNO chain is responsible for only about 1-2% of the solar energy production. It is included here because it produces neutrinos which are, in principle, detectable.

The flux of emitted neutrinos resulting from solar fusion processes are shown in Fig. 1.3, taken directly from Ref. [6]. Knowledge of the neutrino flux emanating from the solar core is
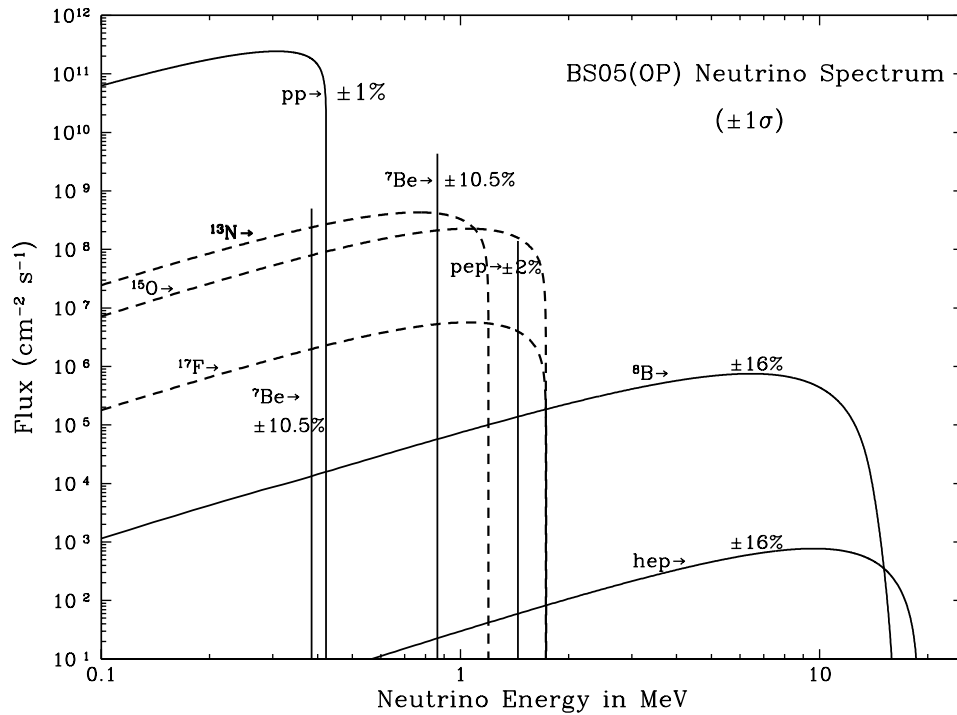
Figure 1.3. The energy spectrum of neutrinos emitted from the solar core. ^{8}B neutrinos provide the dominant flux of neutrinos with energies above 8 MeV. This figure is taken directly from Ref. [6].

a crucial input for the interpretation of experiments which detect solar neutrinos. The Standard Solar Model [6] describes in detail the concentrations of various nuclei throughout the Sun, the frequency of solar fusion reactions, and the flux of neutrinos emitted as byproducts of the fusion reaction chains.

1.2   Solar Neutrino Detection: Methods and Results

A simple argument, based on a few fundamental physical principles, that the Sun acts as a neutrino source was laid out in the previous section. The nuclear processes which power the Sun and produce neutrinos were identified, and a rudimentary description of the cross sections and time scales of these reactions was developed.

Due to the weakly interacting nature of neutrinos, experimental detection of solar neutrinos

14

requires the use of large detectors in an extremely low-background environment. Event rates in solar neutrino detectors are typically on the order of one event per day or less. The realization of these detectors is difficult, and they are generally located deep underground to shield against background from cosmic ray interactions. This section will describe the various methods used to detect neutrinos and the primary results of solar neutrino experiments.

1.2.1 Solar Neutrino Detection Methods

Four distinct classes of reactions have been used to detect solar neutrinos. They are (1) elastic scattering of neutrinos on electrons, (2) neutrino capture on a nucleus, (3) inelastic charged current scattering of neutrinos on deuterons, and (4) neutral current scattering of neutrinos on deuterons.

The section on the solar neutrino problem, Section 1.2.3, will motivate the need to differentiate experimentally between electron-type neutrinos, ν_e, and neutrinos of other flavor, denoted here as $\nu_{\mu,\tau}$. A detailed description of the weak interaction, including interactions of various neutrino flavors with matter, will be given in Chapter 2. However, the four neutrino detection reactions listed above may be understood qualitatively using only basic results of weak interaction physics. The four reactions are discussed in order below.

(1) Elastic Neutrino-Electron Scattering

Elastic ν-e scattering offers an attractive method of detecting solar neutrinos because the neutrino energy spectrum may be inferred from the energy spectrum of the recoil electrons. Additionally, ν_e-e scattering is fundamentally different from $\nu_{\mu,\tau}$-e scattering because the charged current channel is open for ν_e-e scattering. Charged current reactions cannot contribute to $\nu_{\mu,\tau}$-e reactions because solar neutrinos lack the energy to create the heavier μ or τ leptons in the final state.

Diagrams indicating the interactions between the various neutrino flavors and detector electrons are shown in Fig. 1.4. The charged and neutral current contributions to ν_e-e scattering are

$$\sigma_{\mu,\tau} \sim \left| \quad \vcenter{\hbox{Z diagram}} \quad \right|^2$$

$$\sigma_e \sim \left| \quad \vcenter{\hbox{W diagram}} \quad + \quad \vcenter{\hbox{Z diagram}} \quad \right|^2$$
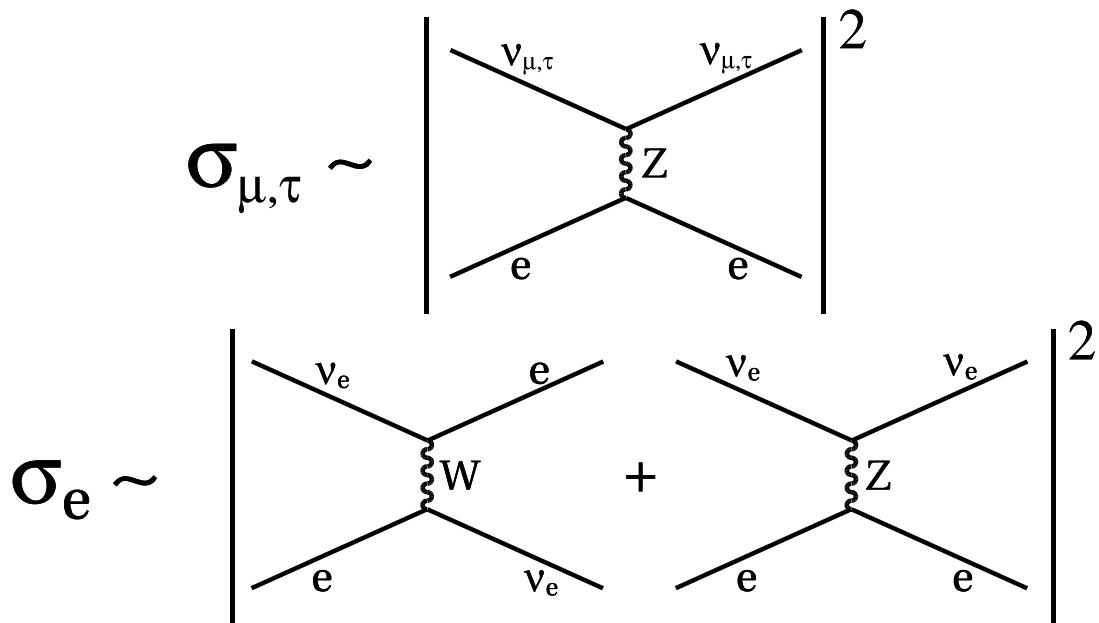
Figure 1.4. A schematic diagram of elastic neutrino-electron scattering reactions. Electron-type neutrinos, ν_e, may interact with target electrons through either the charged or neutral weak current. Mu- or tau-type neutrinos, $\nu_{\mu,\tau}$, may interact only through the neutral current. The cross sections are proportional to the squares of the amplitudes represented by the diagrams.

constructive, that is, the amplitudes for the two processes add in such a way that the probability of interaction is higher than for the neutral current $\nu_{\mu,\tau}$-e scattering. Quantitatively, the probability of ν_e-e scattering is roughly 6 times higher than that for $\nu_{\mu,\tau}$ scattering [7]. The full calculation of Ref. [7] was performed using the charged and neutral current interactions dictated by the Standard Model, outlined in Chapter 2, combined with the complications arising from radiative corrections, which are discussed in the context of nuclear beta decay in Chapter 6. The cross sections [7] for ν_e-e and $\nu_{\mu,\tau}$-e scattering processes are shown in Fig. 1.5. Note that, despite the drastic dependence of the cross sections on neutrino energy, the ratio between ν_e-e and $\nu_{\mu,\tau}$-e cross sections remains roughly constant at a value near 6.

The determination of the solar neutrino energy spectrum from the recoil electron spectrum requires an understanding of the recoil electron spectrum from a monoenergetic neutrino source. For example, the recoil electron spectrum [7] from the dominant ^{7}Be electron capture line, a nearly monoenergetic source of neutrinos with energy 862 keV, is shown in Fig. 1.6. Note that
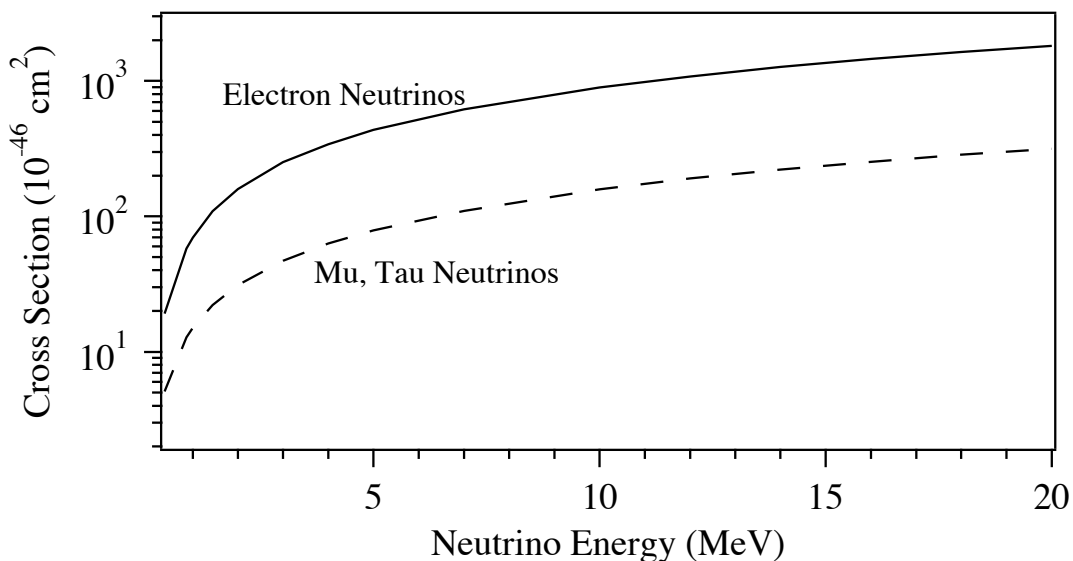
Figure 1.5. The cross sections for ν_e-e and $\nu_{\mu,\tau}$-e scattering as a function of neutrino energy. The lines are interpolations of 15 data values calculated in Ref. [7]. The logarithmic scale used for the cross section indicates the large dependence of cross section on neutrino energy. The energy scale varies between zero and 20 MeV, encompassing the solar neutrino energy spectrum shown in Fig. 1.3.

the shapes of the recoil electron spectra for ν_e-e and $\nu_{\mu,\tau}$-e scattering differ. In principle, then, the flavor components of the solar neutrino flux may be determined experimentally through ν-e scattering. In practice, however, this is nearly impossible since the difference between the normalized ν_e-e and $\nu_{\mu,\tau}$-e recoil spectra are small (1-5%), and this difference is compounded by the factor of 6 between the ν_e-e and $\nu_{\mu,\tau}$-e cross sections (Fig. 1.5).

Experimentally, the ν-e scattering process has been observed using photomultiplier tubes to detect the Cerenkov radiation from recoil electrons in water tanks. Additionally, some proposed neutrino detectors, using methods quite different from water Cerenkov detectors, are designed to be sensitive to ν-e scattering events. These experiments will be outlined briefly in Section 1.2.2.

(2) Neutrino Capture (Inverse Beta Decay)

Neutrino capture was, historically, the first method used to detect solar neutrinos [8]. Neutrino capture is sometimes referred to as inverse beta decay, which differs from beta decay in that
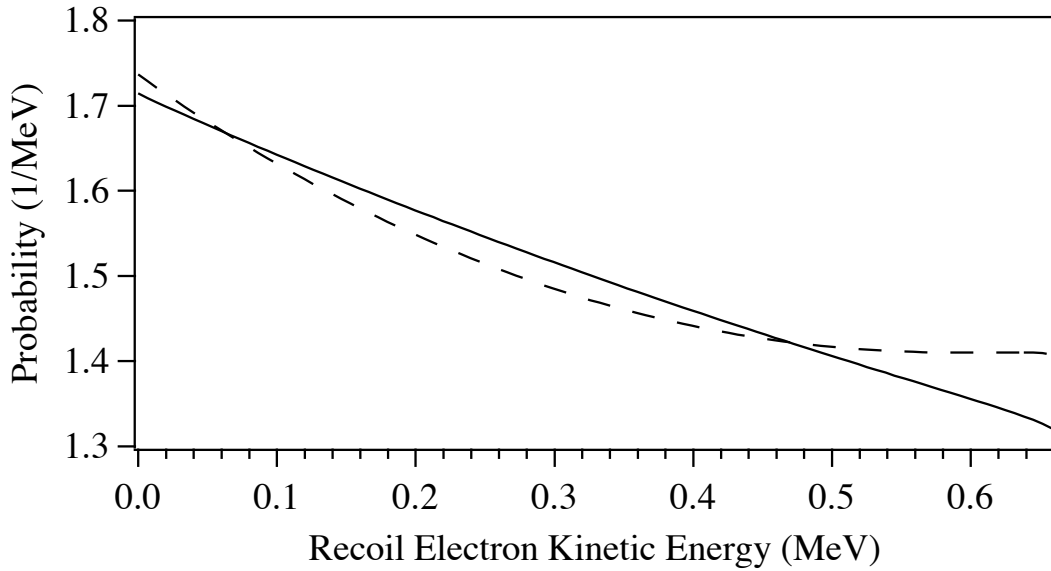
Figure 1.6. The energy spectrum of recoil electrons from elastic ν-*e* scattering due to the monoenergetic (0.862 MeV) neutrinos emitted during the ^{7}Be electron capture process. The solid curve shows the spectrum of recoil electrons from ν_e-*e* scattering. The dashed curve shows the spectrum from ν_μ-*e* scattering. Both spectra are normalized to 1. The spectra drop rapidly to zero as the recoil electron kinetic energy nears 658 keV. The plotted energy spectra were interpolated from 100 data points presented in Ref. [7].

the neutrino is present in the initial state (the analogous beta decay, in this case, would require an *anti*neutrino in the final state). An illustration of the neutrino capture process is shown in Fig. 1.7(a).

Neutrino capture proceeds via the charged weak current to convert an electron-type neutrino into an electron, while increasing the charge of the interacting nucleus by one (transforming a nuclear neutron into a proton). As with charged current ν-*e* scattering, the channel is energetically closed to mu- and tau-type neutrinos.

The final state electron, along with characteristic gamma rays from the possible de-excitation of the final state nucleus, could be detected to signal a neutrino capture event. In practice, however, it is often the radioactive final state nuclei which are detected; the radioactive atoms are chemically separated from the detector and counted as they decay.

18
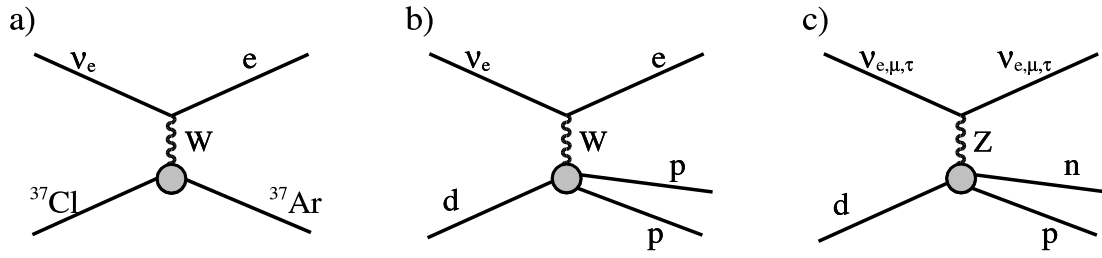
Figure 1.7. Diagrams of the amplitudes of (a) neutrino capture (inverse beta decay) for the special case of a ^{37}Cl target, and (b) charged and (c) neutral current ν-d scattering. Neutral current ν-d scattering is sensitive to all flavors of neutrino, while charged current ν-d scattering and neutrino capture are sensitive only to electron type neutrinos. The shaded gray areas in the figure indicate weak interaction vertices subject to corrections induced by the strong interaction.

The method of radiochemical separation was developed by Ray Davis, Jr. and his collaborators in the Homestake experiment, which reported the first observation of solar neutrinos in 1968 [8]. Descriptions of various neutrino capture experiments are given in Section 1.2.2.

(3) Inelastic Charged Current Neutrino-Deuteron Scattering

The inelastic ν-d charged current reaction, shown in Fig. 1.7(b), dissociates the deuteron while converting the neutron into a proton. The interaction of the neutrino with the deuteron includes vertex corrections arising from the strong interaction [9, 10]. The ν-d charged current scattering process is sensitive only to the electron-type neutrino. In principle, then, detectors observing charged current ν-d scattering should measure the same flux as detectors using neutrino capture, as both are sensitive only to the ν_e flux.

To date, only the SNO heavy water experiment [11] has observed charged current ν-d scattering. SNO uses a water Cerenkov detection scheme to detect the final state electrons. Naturally, this detector is also sensitive to ν-e scattering processes; the two processes may be resolved by their different angular distributions of final state electrons with respect to the Sun [11].

(4) Inelastic Neutral Current Neutrino-Deuteron Scattering

The inelastic ν-d neutral current reaction, illustrated in Fig. 1.7(c), dissociates the deuteron into its component proton and neutron. Again, the effect of the strong interaction on the ν-d

vertex must be considered [12]. The capture of the final state neutrons leads to a gamma ray, providing a unique experimental signature.

The ν-d neutral current interaction has the same cross section for all neutrino flavors. This process thus provides the greatest experimental sensitivity to mu- and tau-type neutrinos (in ν-e scattering, the sensitivity to the $\nu_{\mu,\tau}$ component of the solar neutrino flux was 6 times smaller than the sensitivity to the ν_e flux). Again, SNO [11] is the only experiment utilizing ν-d scattering.

1.2.2 Solar Neutrino Experiments

This section provides a brief overview of solar neutrino detection experiments, in approximate chronological order. For each experiment, the basic methods are discussed, as well as the sensitivity to the various neutrino flavors. A discussion of the main results of these experiments will be postponed until Section 1.2.3, where the history of the solar neutrino problem, and its solution, are outlined.

Homestake (1965-1998) The Homestake experiment [13] consisted of a 615 ton ($\sim$100,000 gallon) tank of perchlorethylene (C_2Cl_4) positioned 4800 feet below the surface in the Homestake mine in South Dakota. The experiment provided the first evidence for solar neutrinos, which interacted via the $^{37}Cl(\nu_e,e)^{37}Ar$ neutrino capture reaction. This reaction has a threshold of roughly 800 keV, and has good sensitivity to the higher energy portion of the solar neutrino spectrum. This is due to transitions to excited states in ^{37}Ar, which increase the capture rate by a factor of 20 compared to what would be expected from transitions to the ground state of ^{37}Ar alone [14].

The final state radioactive ^{37}Ar was chemically extracted from the perchlorethylene where it was identified in proportional chambers as it decayed [13]. The Homestake experiment is of particular importance for several reasons: it verified that solar neutrinos could be detected experimentally, it remained on line for over 30 years and was the only solar neutrino detector operational until 1988, and it remains the only source of ^{37}Cl neutrino capture data.

KamiokaNDE (1988-1996) KamiokanNDE (Kamioka Nucleon Decay Experiment) [15], located

in the Kamioka mine in Japan, was a water Cerenkov detector consisting of 3000 gallons of pure water surrounded by approximately 1000 photomultiplier tubes (PMTs) to detect the Cerenkov light from ν-e scattering recoil electrons. The experiment was originally operated (1983) to search for the decay of protons and bound neutrons; it was upgraded in 1988 to detect solar neutrino events.

Gallex (1991-1997) The Gallex experiment [16] detects neutrinos using the ^{71}Ga(ν_e,e)^{71}Ge neutrino capture reaction. The detector, located at the Gran Sasso National Laboratory in Italy, consisted of roughly 30 tons of gallium in the form of $GaCl_3$ solution in HCl. The threshold for the ^{71}Ga neutrino capture is 233 keV, lower than the Homestake threshold. Gallium detectors are unique in that they are the currently only detectors sensitive to neutrinos from p-p fusion. As in the Homestake experiment, the ^{71}Ge products are chemically separated and their decays counted using proportional chambers.

SAGE (1991-present) SAGE (ruSsian American Gallium Experiment) is a ^{71}Ga neutrino capture experiment [17] located at the Baksan Neutrino Observatory in Russia. Like Gallex, the SAGE experiment utilizes neutrino capture on ^{71}Ga. The gallium is in the form of roughly 50 tons in the (liquid) metal form. The ^{71}Ge products are extracted chemically and counted.

Super-Kamiokande (1996-present) After KamiokaNDE had success detecting solar neutrinos using Cerenkov radiation [15], the larger Super-Kamiokande (SuperK) [18] water Cerenkov detector was constructed in the same underground laboratory. The SuperK detector consists of 50 kilotons of water (22 kilotons fiducial volume), surrounded by over 11,000 PMTs. Increased statistics were obtained from the larger detector, and data on the solar neutrino spectrum and flux was first released in 1998 [19].

GNO (1998-2003) The GNO (Gallium Neutrino Observatory) experiment [20] was the successor of the Gallex experiment, and used the same sample of $GaCl_3$ in HCl solution. The extraction method and data acquisition methods [21] were significantly upgraded from Gallex.

1.2.3 The Solar Neutrino Problem and Solution

The solar neutrino problem originated in 1968 when the Homestake ^{37}Cl capture experiment [8] placed a limit on the solar neutrino flux that was less than half of solar model predictions [22]. As noted in the previous section, additional solar neutrino data have since been collected by the Gallex, SAGE, and GNO ^{71}Ga capture experiments and the Kamiokande, Super-Kamiokande, and Sudbury Neutrino Observatory (SNO) water Cherenkov experiments [23]. These further flux measurements remain inconsistent not only with current solar model predictions [6] but also with each other (when standard electroweak theory is assumed).

Oscillations between neutrinos of different flavor provide the most likely solution to this problem. That is, electron-type neutrinos created by weak processes in the solar core oscillate to different flavor eigenstates as they travel from the solar interior to detectors on Earth. These flavor oscillations are due to a non-zero neutrino mass and are enhanced by the presence of matter, and will be discussed in Chapter 2. The first conclusive evidence that solar neutrinos are indeed changing flavor was provided by measurements of charged- and neutral-current ν-d scattering at SNO [11]. Global analysis of solar neutrino data [23] show that neutrino oscillation scenarios yield good agreement between experiments and solar models. The KamLAND reactor experiment [24], which detects anti-neutrinos created in nuclear power stations, further supports the oscillation interpretation.

1.3 Neutrinos from ^{8}B Beta Decay

The most carefully studied component of the solar neutrino flux is due to neutrinos from the β^+ decay of ^{8}B. As seen in Fig. 1.3, ^{8}B neutrinos account for about 99.9% of the total solar neutrino flux above 1.8 MeV, and are thus accessible to solar neutrino detectors of all thresholds. The ^{8}B neutrinos account for most of the signal in the Homestake ^{37}Cl neutrino capture experiment [13] and nearly all of the solar neutrino events in the Kamiokande [15], Super-Kamiokande [18], and the Sudbury Neutrino Observatory (SNO) [11] water-Cerenkov experiments. Most of the

$$16.922 \text{ MeV} \quad 2^+$$
$$16.626 \text{ MeV} \quad 2^+$$
$$17.979 \text{ MeV} \quad 2^+$$

$$^8\text{B}$$

$$\text{B}^+$$

$$3.0 \text{ MeV} \qquad 2^+$$

$$\text{A}$$

$$0 \text{ MeV} \qquad 0^+$$

$$-0.092 \text{ MeV}$$

$$^4\text{He} + ^4\text{He} \qquad ^8\text{Be}$$
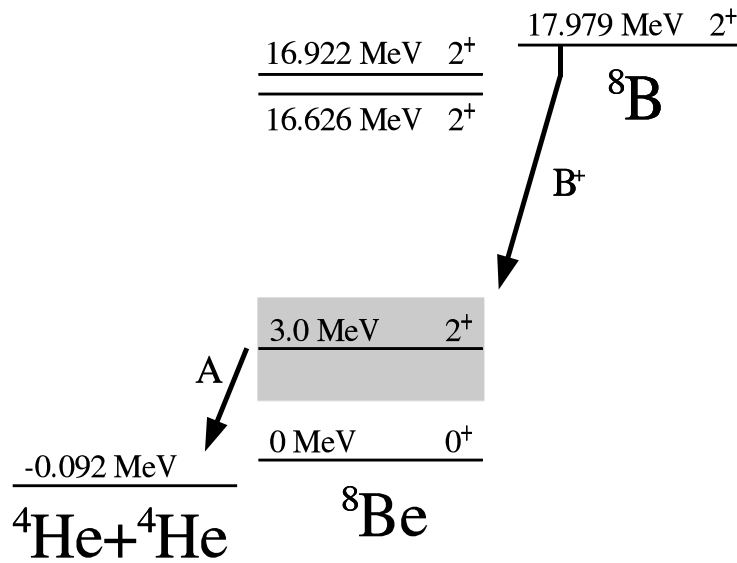
Figure 1.8. Nuclear levels relevant to the ^{8}B decay chain. The β-decay proceeds through the broad 2^+ resonance structure in ^{8}Be peaked at an excitation energy of 3.0 MeV with a width of 1.5 MeV. Decay to the 0^+ ground state in ^{8}Be is second forbidden and is highly suppressed.

signal of ^{71}Ga neutrino capture experiments Gallex [16], GNO [20], and SAGE [17], is due to the p-p fusion neutrinos due to their lower threshold.

As discussed in the previous section, the results from the SNO heavy water detector conclusively demonstrate the existence of a $\nu_{\mu,\tau}$ component of the solar neutrino flux [11]. The solar neutrino data is explained by flavor oscillations and non-zero neutrino mass [25].

Neutrino oscillations are dependent on neutrino energy, hence the neutrino oscillation solution implies that the solar ^{8}B ν_e energy spectrum is distorted. Knowledge of the primary ^{8}B neutrino spectrum is thus a necessary ingredient for the proper interpretation of the solar neutrino data. This is especially true for water-Cerenkov detectors which measure the differential solar neutrino energy spectrum. A distortion of the ν_e component of the spectrum would provide further evidence for neutrino oscillations, and would allow another avenue to determine solar neutrino mixing parameters. No such distortion of the ν_e spectrum has yet been observed [25].

A determination of the physics of leptonic flavor mixing from observations of the solar neutrino spectral shape requires an understanding of the decay of ^{8}B. The ^{8}B ground state ($J^\pi = 2^+$)

undergoes an allowed β^+ transition to a broad range of excitation energies in the ^{8}Be daughter. The width of the ^{8}Be daughter is large since it decays promptly into two α particles. The neutrino spectrum of an allowed β-decay between two *sharp* nuclear states is well-understood; in the case of ^{8}B the neutrino spectrum depends strongly on the excitation energy profile of the α-unstable ^{8}Be daughter, which must be determined experimentally. A diagram illustrating the ^{8}B decay chain is shown in Fig. 1.8. This thesis deals with a determination of the ^{8}B neutrino spectrum based on a new measurement of the alpha spectrum.

I define the ^{8}B β^+ decay **strengthfunction** as the probability that a given differential range of excitation energies in ^{8}Be will be populated by the ^{8}B β^+ decay. The strength function is determined by measurements of the α particle energy spectrum following the breakup of the daughter ^{8}Be nucleus, and is used to construct the neutrino spectrum. A discussion of the levels relevant to ^{8}B β^+ decay and a phenomenological R-matrix description of the strength function is given in Chapter 3. Previous measurements of the α spectrum are discussed in Chapter 4. The primary content and bulk of original work of this thesis consists of a measurement and analysis of the α spectrum. The experiment is described in Chapter 5.

In addition to the strength function, the ^{8}B neutrino spectrum is subject to corrections due to recoil order matrix elements. Angular correlation measurements involving the β decays of ^{8}B and ^{8}Li, along with radiative decay measurements of excited states of ^{8}Be, are used to extract the recoil order matrix elements which contribute to ^{8}B β^+ decay. A general discussion of recoil order effects and a review of past recoil order measurements in the context of their influence on the ^{8}B neutrino spectrum is given in Chapter 6. Finally, the ^{8}B positron and neutrino energy spectra are deduced, using the strength function and applying recoil order and radiative corrections, and presented in Chapter 7.

The following chapter continues the introductory material with a discussion of the weak interaction.

Chapter 2

The Weak Interaction

Neutrinos interact with other particles primarily via the weak interaction. Other possible neutrino interactions, outside of the weak interaction, have important physical implications. For example, neutrinos may interact electromagnetically due to a small magnetic moment. Experiments show the neutrino magnetic moment is very small, at least ten orders of magnitude smaller than the electron magnetic moment [26]. Also, neutrinos posses a small mass that leads to gravitational effects that are astrophysically important [27].

In the context of solar neutrino production and detection, however, electromagnetic and gravitational neutrino interactions may be ignored. The neutrino interactions relevant to this thesis, dealing with the production and detection of solar neutrinos, can be described solely in terms of the weak interaction. This introductory chapter provides an outline of the weak interaction.

In modern physics, the weak interaction is subsumed in the electroweak interaction described by the Standard Model. The first section in this chapter provides a motivation of the Standard Model and describes the fundamental nature of the electroweak interaction. The second section focuses on the behavior of neutrinos themselves and the importance of a nonzero neutrino mass. The final section deals with low energy nuclear processes such as nuclear β decay, which are responsible for both the creation of solar neutrinos and their detection.

2.1 The Standard Model of Electroweak Interactions

A fundamental result of modern physics is that interactions between particles may be constructed by imposing invariance under local symmetry transformations on the field generators for the particles. Local symmetries imposed on field generators are generally referred to as **gauge symmetries**, and theories containing interactions arising from gauge symmetries are called **gauge theories**. Gauge theories are attractive because they are manifestly renormalizable and all facets of the interaction stem from an underlying symmetry.

The Standard Model of electroweak interactions is a gauge theory resulting from a SU(2)×U(1) gauge symmetry. This symmetry is selectively applied to particles based on their chirality in order to describe the parity-violating nature of the weak interaction. Further, a Higgs field is inserted into the theory to break the gauge symmetry and allow particles to have non-zero mass. Before constructing the Standard Model, some simpler examples of gauge theories will be considered.

The Standard Model has been outlined in several textbooks, with its derivation and notation becoming somewhat standardized. This section follows the approach of the two texts [28, 29] from which the author learned the subject.

2.1.1 The U(1) Gauge Theory: Electromagnetism

This section will describe the electromagnetic interaction of Dirac particles in terms of the U(1) gauge symmetry. This example illustrates the basic principles of a gauge theory. The Dirac Lagrangian, $\mathcal{L}_0$, for free non-interacting particles is

$$\mathcal{L}_0 = \overline{\psi}\left(i\gamma^\mu \partial_\mu - m\right)\psi, \tag{2.1}$$

where

$$\overline{\psi} = \psi^* \gamma^0. \tag{2.2}$$

Shifting the wave function by a *global* U(1) phase θ,

$$\psi(x) \rightarrow \psi'(x) = e^{i\theta}\psi(x), \tag{2.3}$$

leaves the Lagrangian unchanged. A well known result of quantum mechanics is that the symmetry of the Lagrangian under global U(1) transformations leads to a conserved current, J^μ, represented in the case of the Dirac Lagrangian by

$$J^\mu = \overline{\psi}\gamma^\mu\psi. \tag{2.4}$$

To create a gauge theory for electromagnetism, a *local* U(1) phase shift $\alpha(x)$ is imposed on the wave function,

$$\psi(x) \rightarrow \psi'(x) = e^{i\alpha(x)}\psi(x). \tag{2.5}$$

The Lagrangian does not remain invariant under the transformation in Eq. 2.5 because it contains a derivative term that transforms as

$$\partial_\mu\psi \rightarrow \partial'_\mu\psi = e^{i\alpha(x)}\Big(\partial_\mu + \big(\partial_\mu\alpha(x)\big)\Big)\psi, \tag{2.6}$$

leading to a new term in the transformed Lagrangian,

$$\mathcal{L}_0 \rightarrow \mathcal{L}'_0 = \overline{\psi}\Big(i\gamma^\mu\partial_\mu - \gamma^\mu\big(\partial_\mu\alpha\big) - m\Big)\psi. \tag{2.7}$$

The Lagrangian may be forced to remain invariant under the U(1) gauge symmetry by substituting the normal derivative, ∂_μ, with the gauge-covariant derivative, $\mathcal{D}_\mu$, defined as

$$\partial_\mu \rightarrow \mathcal{D}_\mu = \partial_\mu + ieA_\mu. \tag{2.8}$$

The introduction of this term requires the existence of a field, A_μ, with which the particles interact. Note that the substitution in Eq. 2.8 is equivalent to the canonical momentum substitution, $p \rightarrow p - eA$, of classical electrodynamics. The new Lagrangian, containing interactions between the original field, ψ, and a vector field, A_μ, is written as

$$\mathcal{L} = \overline{\psi}\big(i\gamma^\mu\mathcal{D}_\mu - m\big)\psi. \tag{2.9}$$

If the field A_μ is forced to transform as

$$A_\mu \to A'_\mu = A_\mu - \frac{1}{e}\partial_\mu\alpha(x), \qquad (2.10)$$

then the gauge-covariant derivative transforms under the U(1) gauge symmetry as

$$\mathcal{D}_\mu \to \mathcal{D}'_\mu = e^{i\alpha(x)}\mathcal{D}_\mu, \qquad (2.11)$$

and the Lagrangian of Eq. 2.9 will remain invariant. The field transformation, Eq. 2.10, is the familiar gauge transformation of the electromagnetic potential. The field, A_μ, introduced to maintain the gauge invariance of the Lagrangian, may then be interpreted as the electromagnetic potential.

Finally, a kinetic term of the electromagnetic field must be included in the Lagrangian. Motivated by classical considerations, the kinetic term is expressed as

$$\mathcal{L}_{EM} = -\frac{1}{4}\mathcal{F}^{\mu\nu}\mathcal{F}_{\mu\nu}, \qquad (2.12)$$

where

$$\mathcal{F}_{\mu\nu} = \partial_\mu A_\nu - \partial_\nu A_\mu \qquad (2.13)$$

is the field strength tensor. Note that the transformation properties of A_μ, Eq. 2.10, imply that $F_{\mu\nu}$, and hence $\mathcal{L}_{EM}$, is invariant under gauge transformation. The complete QED Lagrangian may then be expressed as

$$\mathcal{L}_{QED} = \overline{\psi}\left(i\gamma^\mu\mathcal{D}_\mu - m\right)\psi - \frac{1}{4}\mathcal{F}^{\mu\nu}\mathcal{F}_{\mu\nu}. \qquad (2.14)$$

Using the definition of the covariant derivative, Eq. 2.8, the Lagrangian may be expressed in a more transparent form,

$$\mathcal{L}_{QED} = \overline{\psi}\left(i\gamma^\mu\partial_\mu - m\right)\psi - e\overline{\psi}\gamma^\mu\psi A_\mu - \frac{1}{4}\mathcal{F}^{\mu\nu}\mathcal{F}_{\mu\nu}. \qquad (2.15)$$

where the interaction of the current, $J_\mu = e\overline{\psi}\gamma^\mu\psi$, with the field, A_μ, takes the familiar form.

This exercise, using the U(1) symmetry group, has revealed a relationship between three physical factors that are not obviously related:

- The requirement of a local U(1) gauge symmetry.

- The form of the interaction between particles and the field, given by the covariant derivative, $\mathcal{D}$.

- The familiar gauge transformation behavior of the electromagnetic field.

A quick look back at the preceding argument will show that any two of the factors above can be used to obtain the remaining factor. When building electromagnetism from a U(1) symmetry the result is familiar, the derivation is simple, and the classical theory can be used as a guide. In constructing the full electroweak interaction from a gauge symmetry the process is more systematic: a gauge symmetry is postulated and the covariant derivative is generalized.

2.1.2   The SU(2) Gauge Group

Before moving to a construction of the electroweak Standard Model, some consequences of using a SU(2) gauge group will be discussed. This will serve to introduce the SU(2) group and it will illustrate the basic consequences of using a non-commuting symmetry group. For this case, the wave function, ψ, is an SU(2) spinor containing two Dirac wave functions,

$$\psi = \begin{pmatrix} \psi_1 \\ \psi_2 \end{pmatrix}. \tag{2.16}$$

The Pauli matrices,

$$\sigma_1 = \begin{pmatrix} 0 & 1 \\ 1 & 0 \end{pmatrix}, \quad \sigma_2 = \begin{pmatrix} 0 & -i \\ i & 0 \end{pmatrix}, \quad \sigma_3 = \begin{pmatrix} 1 & 0 \\ 0 & -1 \end{pmatrix}, \tag{2.17}$$

are used as generators of the gauge group. The most general gauge transformation may be expressed as

$$\psi \rightarrow \psi' = G(x)\psi, \tag{2.18}$$

where

$$G(x) = exp\left(\frac{i}{2}\sigma^j\alpha^j(x)\right), \tag{2.19}$$

29

and $\alpha^j(x)$, with $j = 1, 2, 3$, is an arbitrary three-vector transformation parameter.

The implications of SU(2) gauge transformations were studied in 1954 by Yang and Mills in an attempt to create a theory of the strong interaction [30]. The transformations were applied to SU(2) spinors containing wave functions for the proton and neutron. The (isospin) symmetry between protons and neutrons in the strong interaction motivated the gauge requirement. While this approach failed to reproduce experimental details of the strong interaction, the SU(2) gauge transformation eventually became a cornerstone of the Standard Model.

The SU(2) group generators, σ_j, do not commute with each other and, therefore, elements of SU(2) do not generally commute. The non-commutative property leads to behavior not encountered in the simple U(1) example. As in the U(1) treatment, the transformation of the derivative leads to a new term in the Lagrangian that must be balanced by introducing a covariant derivative in order for the Lagrangian to remain invariant under gauge transformations. Explicitly, the derivative transforms as

$$\partial_\mu \psi \rightarrow G \partial_\mu \psi + \left(\partial_\mu G \right) \psi. \tag{2.20}$$

The gauge-covariant derivative is given by

$$\mathcal{D}_\mu = \partial_\mu + i g B_\mu, \tag{2.21}$$

where g is some coupling constant and

$$B_\mu = \frac{1}{2} \sigma^i b^i_\mu, \tag{2.22}$$

and the three b^i_μ, with $i = 1, 2, 3$, represent the interaction fields for each generator of SU(2). For the Lagrangian to remain invariant under SU(2) gauge transformation the covariant derivative must transform as

$$\mathcal{D}_\mu \psi \rightarrow \mathcal{D}'_\mu \psi' = G \mathcal{D}_\mu \psi. \tag{2.23}$$

and the potential B_μ must transform as

$$B_\mu \rightarrow B'_\mu = G \left(B_\mu + \frac{i}{g} G^{-1} \left(\partial_\mu G \right) \right) G^{-1}. \tag{2.24}$$

Eq. 2.24 can be derived from Eq. 2.20 and Eq. 2.21. Using the definition of B_μ in terms of the three fields b_μ^i, Eq. 2.22, yields the gauge transformation law for fields b_μ^i,

$$b_\mu^i \to b_\mu'^i = b_\mu^i - \varepsilon_{ijk}\alpha^j b^k - \frac{1}{g}\delta_\mu\alpha^i. \tag{2.25}$$

Note that the non-commuting nature of the gauge group leads to a gauge transformation, Eq. 2.25, containing a term absent in the gauge transformation for the electromagnetic potential, A_μ of Eq. 2.10.

Finally, a field strength tensor, $F_{\mu\nu}^i$, must be determined for each of the fields b^i such that the Lagrangian of the gauge fields, $\mathcal{L}_{fields}$, takes the form

$$\mathcal{L}_{fields} = -\frac{1}{4}F_{\mu\nu}^i F^{i\mu\nu}. \tag{2.26}$$

The sum runs over both spacetime indices μ and ν as well as the gauge field index i.

The form of $F_{\mu\nu}^i$ may be motivated by a geometrical consideration of the gauge transformation [29]. This also provides a more concrete justification for the existence of the covariant derivative and the interaction fields. The geometrical approach is too advanced for this simple discussion. The result is simply stated here as

$$F_{\mu\nu}^i = \delta_\nu b_\mu^i - \delta_\mu b_\nu^i + g\varepsilon_{ijk}b_\mu^j b_\nu^k. \tag{2.27}$$

The last term in Eq. 2.27 does not appear in the analogous expression for the U(1) field strength tensor, Eq. 2.13. This term vanishes due to the commutative nature of the U(1) symmetry group.

The full Lagrangian of the SU(2) gauge theory may now be expressed as

$$\mathcal{L} = \overline{\psi}(i\gamma^\mu \mathcal{D}_\mu - m)\psi - \frac{1}{4}F_{\mu\nu}^i F^{i\mu\nu}, \tag{2.28}$$

or, expanding the covariant derivative to explicitly show the interaction term,

$$\mathcal{L} = \overline{\psi}(i\gamma^\mu\delta_\mu - m)\psi - \frac{g}{2}b_\mu^i \overline{\psi}\gamma^\mu \tau^i \psi - \frac{1}{4}F_{\mu\nu}^i F^{i\mu\nu}. \tag{2.29}$$

Note that the interaction term takes the form of a field multiplied by a current, as it did in the case of the U(1) gauge symmetry that produced electromagnetism. In this SU(2) case, the current has

the same form as the familiar isotopic current,

$$J_\mu^i = \frac{1}{2}\overline{\psi}\gamma^\mu\sigma^i\psi,$$ (2.30)

which is conserved due to global SU(2) invariance. Each component of the current interacts with one of the fields generated by the gauge transformation.

The full method for generating a gauge interaction theory from the SU(2) group has now been outlined. This process is more complicated than for the U(1) case. There are three interaction fields, one for each group generator. The gauge transformation properties of the fields contain terms not present in the U(1) case that arise from the non-commutative nature of the SU(2) group. The most immediate physical consequence arising from the from the non-commutative gauge group is the presence of the quadratic term in the field-strength tensor of Eq. 2.27. This term leads third and fourth order field terms in the Lagrangian, Eq. 2.29, in addition to the quadratic terms already seen in the U(1) Lagrangian, Eq. 2.15.

When the theory is quantized, Lagrangian terms quadratic in the field lead to propagators for gauge bosons. The U(1) gauge boson (the photon), and the three SU(2) gauge bosons all have associated propagators. Terms that are third and fourth order in the fields, (present in the SU(2) gauge theory) lead to interaction vertices between three and four gauge bosons, a phenomenon absent in first order QED.

As in the U(1) case, the SU(2) gauge transformation requirement for the fields, Eq. 2.25, precludes the existence of a boson mass term. One reason why the Yang-Mills theory failed to accurately describe the strong interaction between nucleons is that the π, ρ, η, etc. bosons that mediate the strong nuclear force are massive and the force is short ranged. The same is true for the weak interaction, and thus the theory must be modified to include massive gauge bosons. In the next section, an example is given where the gauge bosons acquire mass due to a phenomenon known as spontaneous symmetry breaking.

2.1.3 The Higgs Field and Symmetry Breaking

As in the last section, the SU(2) gauge group will be used. Instead of Dirac fields, an SU(2) spinor ϕ, called the Higgs field, containing two complex scalar fields, ϕ_1 and ϕ_2, will be used. Explicitly,

$$\phi = \begin{pmatrix} \phi_1 \\ \phi_2 \end{pmatrix}. \tag{2.31}$$

The Lagrangian for the bare Higgs field without gauge interactions, $\mathcal{L}_0$, is taken to be

$$\mathcal{L}_0 = \delta_\mu \phi^* \delta^\mu \phi - V(\phi), \tag{2.32}$$

where the first term is the usual kinetic term and

$$V(\phi) = -\mu^2 \phi^* \phi + \lambda (\phi^* \phi)^2 \tag{2.33}$$

is a potential representing self-interaction of the Higgs field, and μ and λ are arbitrary constants. If $\mu > 0$, the minimum of the potential $V(\phi)$ lies at some non-zero value of the field ϕ, and ϕ acquires a so-called **vacuum expectation value**, $\langle \phi \rangle$. Due to the freedom of a global SU(2) spinor rotation, the vacuum expectation value may be expressed as

$$\langle \phi \rangle = \frac{1}{\sqrt{2}} \begin{pmatrix} 0 \\ v \end{pmatrix}, \tag{2.34}$$

where

$$v = \frac{\mu}{\lambda^{1/2}}. \tag{2.35}$$

Now the gauge interactions are added by altering the Lagrangian in the usual fashion,

$$\mathcal{L} = \mathcal{D}_\mu \phi^* \mathcal{D}^\mu \phi - V(\phi) - \frac{1}{4} F^i_{\mu\nu} F^{i\mu\nu}. \tag{2.36}$$

Because the SU(2) symmetry is still being used, the covariant derivative and field strength tensor have the same form as in the last section, given by Eqs. 2.21 and 2.27, respectively.

The Lagrangian is no longer invariant under SU(2) gauge transformations because the Higgs field has taken a vacuum expectation value. In fact, even the global SU(2) symmetry is broken. The process by which the symmetry is broken by a Higgs field is called **spontaneous symmetry breaking**.

Expanding the kinetic term of the full Lagrangian, Eq. 2.36, at the vacuum state, $\langle\phi\rangle$, gives

$$\left(\mathcal{D}_\mu\langle\phi\rangle\right)^*\left(\mathcal{D}^\mu\langle\phi\rangle\right) = \left(\partial_\mu\langle\phi\rangle^* + \frac{ig}{2}\sigma^i b^i_\mu\langle\phi\rangle^*\right)\left(\partial^\mu\langle\phi\rangle - \frac{ig}{2}\sigma^i b^{i\mu}\langle\phi\rangle\right) =$$

$$= \frac{g^2}{8}\left(\begin{array}{cc} 0 & v \end{array}\right)\sigma^i\sigma^j\left(\begin{array}{c} 0 \\ v \end{array}\right)b^i_\mu b^{j\mu} + \cdots = \frac{g^2 v^2}{8}b^i_\mu b^{i\mu} + \cdots, \tag{2.37}$$

where the anti-commutator identity $\{\sigma^a,\sigma^b\} = 2\delta^{ab}$ was used in the last step, and the sums are over both the space-time indices μ and the gauge generator indices i and j. Thus, the Lagrangian contains gauge boson mass terms of the form

$$\mathcal{L}_{b-mass} = \frac{m^2}{2}b^i_\mu b^{i\mu}, \tag{2.38}$$

with

$$m_b = \frac{gv}{2}. \tag{2.39}$$

The presence of the Higgs field, with its vacuum expectation value, has been shown to break the SU(2) gauge symmetry and causes the gauge bosons to acquire mass. Further investigation of the Higgs field requires that the kinetic term in the Lagrangian be expanded about the vacuum expectation value. This expansion makes explicitly clear the interaction between the four components of the Higgs field and the gauge bosons. Three degrees of freedom of the Higgs field are shown to be massless, while one possesses mass. Using a suitable gauge transformation it is possible to eliminate the explicit appearance of the three massless Higgs components in the Lagrangian. Instead, those components are absorbed into the Lagrangian of the gauge boson. This is necessary because a massless gauge boson has only two (transverse) degrees of freedom, while a massive gauge boson must have three (two transverse and one longitudinal). Essentially, the massless components of the Higgs field become the longitudinal component of the gauge bosons.

It is a general result that when a symmetry of the Lagrangian is broken, the boson associated with the generator of that symmetry must acquire mass. Since the entire SU(2) symmetry was broken in this example, all gauge bosons acquired mass. In the next section, the Standard Model will be derived. To retain one massless gauge boson, the photon, one symmetry of the Lagrangian must be left unbroken.

2.1.4 The Standard Model of ElectroWeak Interactions

In constructing the Standard Model it is necessary to first define the gauge groups. Next, we define the Higgs field that breaks symmetry and its properties. The part of the Lagrangian associated with the gauge bosons must be determined to reveal their properties. Later, the matter particles that participate in the ElectroWeak interaction will be included, and their coupling to the gauge fields will be defined. Ultimately, the entire interaction Lagrangian, detailing all electromagnetic and weak interactions between matter, will be found.

The Broken Gauge Symmetry The gauge group of the Standard Model is SU(2)×U(1). The three generators of the SU(2) group, taken as the Pauli matrices of Eq. 2.17, together with the U(1) generator that provides a simple phase shift, provide four gauge bosons for the theory. The Higgs field, ϕ, is again taken as a two-component complex scalar field defined to transform as a spinor under SU(2). The Higgs field is assigned a U(1) charge $Y = +1/2$, where the U(1) charge defines the field's transformation properties under U(1) gauge rotations. Thus, the Higgs field transforms as

$$\phi \rightarrow \phi' = exp(\frac{i}{2}\sigma^j\alpha^j)exp(i\frac{\beta}{2})\phi, \tag{2.40}$$

where the α^i and β parameterize the SU(2) and U(1) gauge transformations, respectively.

Again, the Higgs field is constructed to take a vacuum expectation values defined by

$$\langle\phi\rangle = \frac{1}{\sqrt{2}}\begin{pmatrix} 0 \\ v \end{pmatrix}. \tag{2.41}$$

From the definition of the SU(2) generators σ^i, it is easy to see that a gauge transformation satisfying the properties

$$\alpha_1 = \alpha_2 = 0, \quad \alpha_3 = \beta \tag{2.42}$$

will leave $\langle\phi\rangle$, and hence the Lagrangian, invariant. Thus, there is still one gauge symmetry, corresponding to the combination of transformation parameters in Eq. 2.42 that is not broken by the Higgs field. The remaining symmetry will produce a massless boson, the photon.

The Gauge Fields The gauge fields associated with the SU(2) symmetry will be denoted a^i_μ,

and the associated coupling constant as g. The field associated with U(1) will be denoted as B_μ, with a coupling constant g'. The covariant derivative of the Higgs field is then expressed as

$$\mathcal{D}_\mu \phi = (\partial_\mu - \frac{i}{2} g a_\mu^i \sigma^i - \frac{i}{2} g' B_\mu) \phi. \tag{2.43}$$

The gauge boson masses arise from an expansion of the Higgs kinetic term in the Lagrangian, $(\mathcal{D}_\mu)^*(\mathcal{D}^\mu)$. The computation is similar to that in the last section (see Eq. 2.37, and it will not be shown explicitly. The resulting term in the Lagrangian is

$$\mathcal{L}_{boson-mass} = \frac{v^2}{8} \left(g^2 a_\mu^1 a^{1\mu} + g^2 a_\mu^2 A^{2\mu} + (-g a_\mu^3 + g' B_\mu)(-g a^{3\mu} + g' B^\mu) \right). \tag{2.44}$$

The results of this section are better understood in terms of the following combinations of gauge fields:

$$W_\mu^\pm = \frac{1}{\sqrt{2}} (a_\mu^1 \mp i a_\mu^2), \tag{2.45}$$

$$Z_\mu^0 = \frac{1}{\sqrt{g^2 + g'^2}} (g a_\mu^3 - g' B_\mu), \tag{2.46}$$

and

$$A_\mu = \frac{1}{\sqrt{g^2 + g'^2}} (g' a_\mu^3 + g B_\mu), \tag{2.47}$$

where the $W_\mu^\pm$ are identified as the fields of the W-bosons responsible for the charged weak interaction, Z_μ^0 as the field of the Z-boson responsible for the neutral weak interaction, and A_μ as the photon field which produces the electromagnetic field. The gauge boson mass term in the Lagrangian then becomes

$$\mathcal{L}_{boson-mass} = \frac{gv}{4} W_\mu^+ W^{+\mu} + \frac{gv}{4} W_\mu^- W^{-\mu} + \frac{\sqrt{g^2 + g'^2} v}{4} Z_\mu^0 Z^{0\mu}, \tag{2.48}$$

implying gauge boson masses of $m_W = gv/2$ and $m_Z = \sqrt{g^2 + g'^2} v/2$. The photon field, A_μ, results from the one remaining symmetry of the Lagrangian and is, therefore, massless.

It is convenient to think of the relationship between the original gauge fields a_μ^3, B_μ and the physical fields Z_μ, A_μ, given by Eqs. 2.46 and 2.47, as a rotation:

$$\begin{pmatrix} Z \\ A \end{pmatrix} = \begin{pmatrix} cos\theta_w & -sin\theta_w \\ sin\theta_w & cos\theta_w \end{pmatrix} \begin{pmatrix} a^3 \\ B \end{pmatrix}. \tag{2.49}$$

The rotation parameter, θ_w, is called the **Weinberg angle** or the **weak mixing angle** and is evidently related to the gauge coupling constants by

$$cos\theta_w = \frac{g}{\sqrt{g^2 + g'^2}}, \quad sin\theta_w = \frac{g'}{\sqrt{g^2 + g'^2}}. \tag{2.50}$$

Gauge Interactions of Fermions The interaction of matter particles with the gauge fields will now be investigated. Generally, the covariant derivative takes the form

$$\mathcal{D}_\mu = \partial_\mu - gA_\mu^j T^j - ig'YB_\mu, \tag{2.51}$$

where T^i are matrices generating transformations under some representation of SU(2).

In the Standard Model, all matter fields transform under SU(2) as spinors, for which

$$T^i = \sigma^i/2, \tag{2.52}$$

or else they will have no transformation under SU(2),

$$T^i = 0. \tag{2.53}$$

The Higgs field has already been defined to transform as a spinor. The remaining matter fields to consider are the leptons and quark field. These fermion fields represent the fundamental building blocks of nature. In the Standard Model lepton and quark fields are separated into two fields, ψ_L and ψ_R, according to chirality:

$$\psi_L = \frac{1}{2}(1 - \gamma_5)\psi, \quad \psi_R = \frac{1}{2}(1 + \gamma_5)\psi. \tag{2.54}$$

where ψ is a generic Dirac spinor. The chirality of the fields is used to define the SU(2) transformation properties, with left-handed fields transforming as spinors, and right handed fields remaining invariant under SU(2).

Left-handed quarks fields, u_L and d_L, and lepton fields, e_L and ν_L, are denoted by the SU(2) spinors

$$\begin{pmatrix} u_L \\ d_L \end{pmatrix}, \quad \begin{pmatrix} \nu_L \\ e_L \end{pmatrix}. \tag{2.55}$$

Because the left-handed components transform as SU(2) spinors, matter particles must come in pairs. Each pair is referred to as a generation. Experimentally, three generations of quarks and leptons have been observed. The Standard Model does not limit the number of generations of particles. However, upon quantization (a matter beyond the scope of this simple discussion) the theory is only free of anomalies when the number of quark generations is equal to the number of lepton generations.

Having no SU(2) transformation, the right handed matter fields are then denoted as singlets:

$$u_R, \; d_R, \; e_R, \; \nu_R. \tag{2.56}$$

Because the neutrino has near-zero mass, the field ν_R is neglected in the Standard Model. Often it is said that the Standard Model requires zero neutrino mass. This is misleading, since it is possible to include ν_R in the discussion and trivially extend the Standard Model to include neutrino mass. Problems arise only when the neutrino is described as a Majorana particle (as opposed to a Dirac particle). In the case of a Majorana neutrino the extension to the theory is more complicated. Additional aspects of neutrino physics will be discussed in the next section.

Expressing the covariant derivative, Eq. 2.51, in terms of the physical gauge fields, Eqs. 2.45, 2.46, and 2.47, yields

$$\mathcal{D}_\mu = \partial_\mu - \frac{ig}{\sqrt{2}}(W_\mu^+ T^+ + W_\mu^- T^-) - \frac{ig}{cos\theta_W} Z_\mu(T^3 - sin^2\theta_W Q) - ieA_\mu Q. \tag{2.57}$$

The term involving the electromagnetic field, A_μ, take its usual form, the electromagnetic coupling constant e has been defined in terms of the gauge coupling constants,

$$e = \frac{gg'}{\sqrt{g^2 + g'^2}}, \tag{2.58}$$

and the electric charge Q has been defined in terms of the U(1) charge Y and the 3-component of isospin, T^3,

$$Q = T^3 + Y. \tag{2.59}$$

Based on helicity, T_3 is given by the SU(2) transformation properties of the lepton or quark fields. Using the electric charges, it is straightforward to assign a U(1) charge to each of the fields based on Eq. 2.59. The results are shown in Table 2.1.

Fermion Field	Q	T_3	Y
ν_L	0	+1/2	-1/2
e_L	1	-1/2	-1/2
u_L	+2/3	+1/2	+1/6
d_L	-1/3	-1/2	+1/6
e_R	-1	0	-1
u_R	+2/3	0	+2/3
d_R	-1/3	0	-1/3

Table 2.1. The electric charge, Q, the third component of weak isospin, T_3, and the U(1) charge, Y, for each of the fermion fields in the Standard Model.

Having determined the transformation properties of the fermion fields under the Standard Model gauge symmetries, the fermion kinetic terms may be expressed using the covariant derivative of Eq. 2.57,

$$\mathcal{L} = \left(\begin{array}{cc} \overline{u}_L & \overline{d}_L \end{array} \right) (i\gamma^\mu \mathcal{D}_\mu) \left(\begin{array}{c} u_L \\ d_L \end{array} \right) + \left(\begin{array}{cc} \overline{\nu}_L & \overline{e}_L \end{array} \right) (i\gamma^\mu \mathcal{D}_\mu) \left(\begin{array}{c} \nu_L \\ e_L \end{array} \right) +$$

$$+ \overline{u}_R (i\gamma^\mu \mathcal{D}_\mu) u_R + \overline{d}_R (i\gamma^\mu \mathcal{D}_\mu) d_R + \overline{e}_R (i\gamma^\mu \mathcal{D}_\mu) e_R. \tag{2.60}$$

Using the expression for the covariant derivative, Eq. 2.57, and the weak isospin and U(1) charge values of Table 2.1, yields

$$\mathcal{L} = \left(\begin{array}{cc} \overline{u}_L & \overline{d}_L \end{array} \right) (i\gamma^\mu \partial_\mu) \left(\begin{array}{c} u_L \\ d_L \end{array} \right) + \left(\begin{array}{cc} \overline{\nu}_L & \overline{e}_L \end{array} \right) (i\gamma^\mu \partial_\mu) \left(\begin{array}{c} \nu_L \\ e_L \end{array} \right) +$$

$$+ \overline{u}_R (i\gamma^\mu \partial_\mu) u_R + \overline{d}_R (i\gamma^\mu \partial_\mu) d_R + \overline{e}_R (i\gamma^\mu \partial_\mu) e_R +$$

$$+ \frac{g}{\sqrt{2}} (W_\mu^+ J_W^{+\mu} + W_\mu^- J_W^{-\mu} + Z_\mu^0 J_Z^\mu) + e A_\mu J_{EM}^\mu, \tag{2.61}$$

where the charged weak currents, $J_W^{+\mu}$ and $J_W^{-\mu}$, are given by

$$J_W^{+\mu} = \left(\overline{\nu}_L \gamma^\mu e_L + \overline{u}_L \gamma^\mu d_L \right) \tag{2.62}$$

and

$$J_W^{-\mu} = \left(\overline{e}_L \gamma^\mu \nu_L + \overline{d}_L \gamma^\mu u_L \right). \tag{2.63}$$

The neutral weak current, J_Z^μ, is given by

$$J_Z^\mu = \frac{\sqrt{2}}{\cos\theta_w}\left[\overline{\nu}_L\gamma^\mu(\tfrac{1}{2})\nu_L + \overline{e}_L\gamma^\mu(-\tfrac{1}{2}+\sin^2\theta_w)e_L + \overline{e}_R\gamma^\mu(\sin^2\theta_w)\nu_L + \right.$$

$$+\overline{u}_L\gamma^\mu(\tfrac{1}{2}-\tfrac{2}{3}\sin^2\theta_w)u_L + \overline{u}_R\gamma^\mu(-\tfrac{2}{3}\sin^2\theta_w)u_R + \tag{2.64}$$

$$\left. +\overline{d}_L\gamma^\mu(-\tfrac{1}{2}+\tfrac{1}{3}\sin^2\theta_w)d_L + \overline{d}_R\gamma^\mu(\tfrac{1}{3}\sin^2\theta_w)d_R\right],$$

and the electromagnetic current, J_{EM}^μ, is given by

$$J_{EM}^\mu = \overline{e}\gamma^\mu(-1)e + \overline{u}\gamma^\mu(+\tfrac{2}{3})u + \overline{d}\gamma^\mu(-\tfrac{1}{3})d. \tag{2.65}$$

The interaction terms between matter fields and electroweak boson fields, given by Eqs. 2.62-2.65, are one of the two primary results of this chapter. The second, discussed next, deals with fermion mass in the Standard Model. Fermion mass, specifically neutrino mass, gives rise to flavor changing phenomena that provide a possible solution to the solar neutrino problem.

Fermion Mass Terms The Lagrangian, $\mathcal{L}_0$, for a free Dirac particle with mass m can be expressed as

$$\mathcal{L}_I = \overline{\psi}(i\gamma^\mu\partial_\mu - m)\psi = \overline{\psi}_L i\gamma^\mu\partial_\mu\psi_L + \overline{\psi}_R i\gamma^\mu\partial_\mu\psi_R - m(\overline{\psi}_L\psi_R + \overline{\psi}_R\psi_L), \tag{2.66}$$

where states of definite chirality are mixed by the mass term. In the Standard Model, the left- and right-handed chirality eigenstates possess different SU(2) transformation properties. As such, the fermion mass terms shown in Eq. 2.66 cannot be present in the Standard Model Lagrangian. Instead, mass terms are generated by the interaction of matter fields with the Higgs field.

The simplest gauge invariant term that couples the electron field to the Higgs field is

$$\mathcal{L}_{mass} = -\lambda_e\left(\begin{array}{cc}\overline{\nu}_{eL} & \overline{e}_L\end{array}\right)\cdot\left(\begin{array}{c}\phi_1 \\ \phi_2\end{array}\right)e_R + h.c. \tag{2.67}$$

which simplifies to

$$-\frac{1}{\sqrt{2}}\lambda_e v\overline{e}_L e_R + h.c. \tag{2.68}$$

when the vacuum expectation value of the Higgs field is applied. The coupling constant λ, which gives the interaction strength between the electron fields and the Higgs field, produces an electron

mass term in the Lagrangian given by

$$m_e = \frac{1}{\sqrt{2}} \lambda_e v. \tag{2.69}$$

The quark mass terms are slightly trickier, since unlike neutrinos, the u-type quarks occupying the first component of the SU(2) spinors possess mass (in this simple formulation of the Standard Model we have approximated the neutrino as massless). The gauge invariant term generating the quark masses is given by

$$\mathcal{L}_{mass} = -\lambda_d \left(\begin{array}{cc} \overline{u}_L & \overline{d}_L \end{array} \right) \cdot \left(\begin{array}{c} \phi_1 \\ \phi_2 \end{array} \right) d_R - \lambda_u \left(\begin{array}{cc} \overline{d}_L & \overline{u}_L \end{array} \right) \cdot \left(\begin{array}{c} \phi_1 \\ \phi_2 \end{array} \right) u_R + h.c. \tag{2.70}$$

which simplifies to give quark masses

$$m_d = -\frac{1}{\sqrt{2}} \lambda_d v, \ m_u = -\frac{1}{\sqrt{2}} \lambda_u v. \tag{2.71}$$

It should be explicitly noted that the new mass terms generated by interactions between the fermions and the Higgs field are gauge invariant. This is because the SU(2) and U(1) charges of the fields composing the Lagrangian terms in Eqs. 2.67 and 2.70 sum to zero. One can easily verify this by examining Table 2.1, and recalling that the Higgs field, ϕ, has U(1) charge $+\frac{1}{2}$ and transforms as an SU(2) spinor. It was previously stated that a trivial extension of the Standard Model allows for neutrino mass. This could be performed by postulating the existence of right-handed neutrino fields, ν_R, and adding a term to Eq. 2.67 similar to the second term of Eq. 2.70, generating the mass of the u-type quarks. Gauge invariance of the Lagrangian would then require that the ν_R fields have no U(1) or SU(2) charge and thus do not interact via the electroweak force.

Before fermion masses were introduced into the theory, the only input parameters of the Standard Model were the gauge coupling constants, g and g', and the vacuum expectation value of the Higgs field, v. These initial three parameters are usually expressed in terms of somewhat more physical constants e, $sin\ \theta_w$, and m_W. An often stated deficiency of the Standard Model is the inclusion of nine new parameters, λ_i, one for each of the three known generations of leptons, and two for each of the three known generations of quarks.

In fact, the new fermion mass terms require four more parameters to be introduced. This is because the fermion fields are eigenstates of mass but are not necessarily eigenstates of the interactions; that is, the fermion fields of Eqs. 2.67 and 2.70 need not be the same as the fermion fields that interact with the gauge bosons in Eqs. 2.62-2.65. This complication allows the phenomena of CP violation and Cabbibo suppression to be explained and, with a slight extension, allows a parametrization of neutrino oscillations. The next section briefly introduces these concepts.

The CKM Matrix Eigenstates of the gauge interactions, known as flavor eigenstates, must be related to the mass eigenstates of the previous section via the most general 3×3 unitary matrix. Assuming the lack of ν_R fields, and hence neutrino mass, the ν_L fields may be defined (without loss of generality) such that no rotation is needed for the leptons. For the quarks, there is sufficient freedom to define the u-type quark mass eigenstates as flavor eigenstates, and to consider a unitary transformation between the flavor and mass eigenstates of the d-type quarks.

The three u-type quark fields, which are eigenstates of both mass and flavor, are called the up (u), charm (s), and top (t) quark fields. The d-type mass eigenstates, called down (d), strange (s), and bottom (b), are then related to the flavor eigenstates, d', s', and b', by

$$
\begin{pmatrix} d' \\ s' \\ b' \end{pmatrix} = \begin{pmatrix} V_{ud} & V_{us} & V_{ub} \\ V_{cd} & V_{cs} & V_{cb} \\ V_{td} & V_{ts} & V_{tb} \end{pmatrix} \begin{pmatrix} d \\ s \\ b \end{pmatrix}. \tag{2.72}
$$

The 3×3 unitary matrix is called the Cabbibo-Kobayashi-Maskawa matrix, V_{CKM}, and is filled with elements $V_{\alpha\beta}$. There are four degrees of freedom for the most general 3×3 unitary matrix. To illustrate this it is often written explicitly as

$$
V_{CKM} = \begin{pmatrix} c_{12}c_{13} & s_{12}c_{13} & s_{13}exp(-i\delta) \\ -s_{12}c_{23} - c_{12}s_{23}s_{13}exp(i\delta) & c_{12}c_{23} - s_{12}s_{23}s_{13}exp(i\delta) & s_{23}c_{13} \\ s_{12}s_{23} - c_{12}c_{23}s_{13}exp(i\delta) & -c_{12}s_{23} - s_{12}c_{23}s_{13}exp(i\delta) & c_{23}c_{13} \end{pmatrix}. \tag{2.73}
$$

Here $c_{ij} = cos\theta_{ij}$ and $s_{ij} = sin\theta_{ij}$. The four parameters of the unitary transformation, $\theta_{12}, \theta_{13}, \theta_{23}$, and δ are further input parameters to the Standard Model determined by experiment.

The representation of Eq. 2.73 is the *standard representation* advocated by the Particle Data

Group. As will be discussed in the next section, for the case of neutrino mass, a similar matrix may be used to parameterize neutrino flavor oscillations.

The CKM matrix has some basic physical manifestations. For instance, the V_{us} value, about 1/4, is responsible for the decreased strength of weak processes coupling the *u* and *s* quarks, compared to couplings between the *u* and *d* quarks. This phenomenon, historically known as Cabibbo suppression, led to the first phenomenological flavor mixing matrix . Another important manifestation stems from the δ phase parameter accounts for CP violating processes, a puzzle first noticed in the decay of neutral kaons.

Conclusions This completes the rudimentary discussion of the Standard Model. In summary, the SU(2)×U(1) gauge symmetry is broken by some Higgs field. This leads to an interaction between fermion fields and gauge bosons that describes the observed electroweak interactions. These interactions depend on only three parameters: e, $sin\theta_w$, and m_W. As mentioned previously, three degrees of freedom of the Higgs field become longitudinal components of the three massive bosons, providing mass and charge. The last component, not yet discussed, should exist as a scalar particle known as the Higgs boson. No conclusive experimental evidence for the Higgs boson has been found.

The addition of fermion mass terms requires coupling between the Higgs field and the fermions. This requires nine further parameters, one for each massive particle. Furthermore, the CKM matrix requires four more parameters, which allow for flavor changing processes to occur.

The next section discusses the physics of neutrino flavor oscillations. These oscillations of neutrinos from one flavor to another depend on both a non-zero neutrino mass and a mixing matrix for leptons analogous to the CKM matrix.

2.2 Neutrino Oscillations

The term **neutrino oscillations** refers to the quantum phenomenon of a neutrino created in a certain flavor eigenstate changing, or oscillating, to a different flavor eigenstate as it propagates. The experimental evidence [23] for neutrino oscillations was briefly discussed in the context of the solar neutrino problem in Section 1.2.3. This section provides a brief description of the physics behind neutrino oscillations and, specifically, implications for ^{8}B neutrinos created in the Solar core. The high density of electrons in the Sun which drops off adiabatically (in the context of neutrino oscillations) with solar radius, coupled with the phenomenon of **matter − enhanced** neutrino oscillations, will be shown to have a significant effect on the ^{8}B neutrino energy spectrum.

As with the Standard Model material of the previous section, the physics of neutrino oscillations has been discussed extensively in review papers and books. As a result, the associated terminology and notation have become rather standardized. The material in this section roughly follows the notations and approach of the book *Neutrino Astrophysics* by John Bahcall [5].

2.2.1 Vacuum Oscillations

In Section 2.1, it was noted that the quark mass eigenstates were not the same as the the flavor eigenstates which participate in the weak interaction. Without loss of generality, the u-type quarks were taken to be eigenstates of both mass and flavor, while the d-type quarks required the CKM matrix to describe the change of basis between mass and flavor eigenstates as shown in Eq. 2.72. If we allow neutrinos to have a non-zero mass, an analogous situation exists for leptons. We take the charged leptons to be eigenstates of both mass and flavor, while the neutrino flavor eigenstates ν_α (α=e,μ,τ) are described in terms of the mass eigenstates ν_j (j=1,2,3) by a mixing matrix $U_{\alpha j}$,

$$|\nu_\alpha(t)\rangle = \sum_j U_{\alpha j} exp(-\frac{i}{\hbar}E_j t)|\nu_j\rangle. \tag{2.74}$$

The mixing matrix $U_{\alpha j}$ is called the Maki-Nakagawa-Sakata matrix, or MNS matrix. The probability, then, that a neutrino created in flavor eigenstate ν_α will behave as a ν_α at some later time t is given by

$$|\langle \nu_\beta(t)|\nu_\alpha(0)\rangle|^2 = \sum_{j,k} U_{\alpha j} U_{\beta j}^* U_{\alpha k}^* U_{\beta k} exp[-\frac{i}{\hbar}(E_j - E_k)t]. \qquad (2.75)$$

For solar neutrino experiments unable to provide a definite energy resolution, such as the Homestake ^{37}Cl neutrino capture experiment that first detected an apparent deficit in the solar neutrino flux [13], it is convenient to average Eq. 2.75 over neutrino energies. Following Bahcall, who showed [31] that an average over a range of energies leads to cancellations between terms in Eq. 2.75 where $j \neq k$, we obtain

$$|\langle \nu_e(t)|\nu_e(0)\rangle|^2 = \sum_{j} |U_{ej}|^4, \qquad (2.76)$$

which is the probability that an electron-type neutrino created at time $t = 0$ is observed as an electron-type neutrino at some later time t. The condition that the MNS matrix be unitary places a restraint on the smallness of $|\langle \nu_e(t)|\nu_e(0)\rangle|^2$, given by

$$|\langle \nu_e(t)|\nu_e(0)\rangle|^2 \geq \frac{1}{N}, \qquad (2.77)$$

where $N = 3$ is the number of lepton flavors. This provides the important result that the solar ν_e flux may be reduced by at most a factor of 3 by neutrino oscillations in a vacuum. In fact, for vacuum oscillations to reduce the observed solar ν_e by a factor even close to 3, which is near what the original Homestake experiment observed [13], both the MNS mixing angles and the Earth-Sun distance would have to be **fine tuned**; that is to say, the MNS mixing angles would have to be much larger than those of the CKM matrix, *and* the Earth-Sun distance would have to be in a narrow range defined by the large MNS mixing angles. Vacuum oscillations thus do not offer a desirable solution to the solar neutrino problem, and it is now known conclusively [23] that matter-enhanced oscillations are required to offer a solution. Matter-enhanced oscillations are discussed in the next section. It is convenient, however, to carry on the discussion of vacuum oscillations so as to introduce terminology and equations which have useful analogs in the discussion of matter-enhanced oscillations.

For simplicity we consider only two flavor and mass eigenstates, and the mixing matrix then only requires one parameter θ_V, the vacuum mixing angle. The change of basis is then given by

$$\begin{pmatrix} \nu_e \\ \nu_\mu \end{pmatrix} = \begin{pmatrix} cos\theta_V & sin\theta_v \\ -sin\theta_V & cos\theta_v \end{pmatrix} \begin{pmatrix} \nu_1 \\ \nu_2 \end{pmatrix}. \tag{2.78}$$

The probability that a ν_e interacts as a ν_e at some later time is then

$$|\langle \nu_e(t)|\nu_e(0)\rangle|^2 = 1 - sin^2 2\theta_V sin^2 [\frac{E_2 - E_1}{2\hbar} t]. \tag{2.79}$$

This equation simplifies to the well-known expression

$$|\langle \nu_e(t)|\nu_e(0)\rangle|^2 = 1 - sin^2 2\theta_V sin^2 [\frac{\pi l}{L_V}], \tag{2.80}$$

where l is the distance traveled by the neutrinos, the L_V is the vacuum oscillation length,

$$L_V = \frac{4\pi E \hbar}{\Delta m^2 c^3}, \tag{2.81}$$

and Δm^2 is the difference of the squares of the neutrino masses,

$$\Delta m^2 = |m_1^2 - m_2^2|. \tag{2.82}$$

Note then the important point that neutrino oscillation experiments are sensitive only to this Δm^2 value, and not the masses of the neutrinos themselves.

The inclusion of matter effects on neutrino oscillations is described most easily by explicitly defining a Hamiltonian. In this context the Hamiltonian is referred to as the **massmatrix**, denoted for vacuum oscillations as M_0. Any neutrino state can naturally be described in the flavor basis as

$$|\nu(t)\rangle = c_e(t)|\nu_e\rangle + c_\mu(t)|\nu_\mu\rangle. \tag{2.83}$$

Note that one may include all three neutrino flavors with the same technique, although this is apparently quite a burden in practice. Two flavors are adequate for this discussion which seeks only to highlight the general ideas of mixing. After symmetrizing the mass matrix, the coefficients $c_{e,\mu}(t)$ may be shown to evolve with time as

$$i\hbar \begin{pmatrix} c_e(t) \\ c_\mu(t) \end{pmatrix} = \pm \frac{\Delta_V}{2} \begin{pmatrix} -cos2\theta_V & sin2\theta_V \\ sin2\theta_V & cos2\theta_V \end{pmatrix} \begin{pmatrix} c_e(t) \\ c_\mu(t) \end{pmatrix}, \tag{2.84}$$

46

where the term Δ_V is defined in terms of the vacuum oscillation length,

$$\Delta_V = \frac{2\pi\hbar c}{L_V} = |\frac{\Delta m^2 c^4}{2E}|,$$ (2.85)

and the mass matrix M_0 is taken to be the 2×2 matrix operating on the right-hand side of Eq. 2.84.

2.2.2 Matter-Enhanced Oscillations

The seminal works of Wolfenstein [32, 33] in 1978 and 1979, and Mikheyev and Smirnov [34, 35, 36] laid the groundwork for matter-enhanced neutrino oscillations. The need for fine-tuning in vacuum oscillation solutions to the solar neutrino problem was undesirable, and matter-enhanced oscillations provide a way around this problem. The presence of electrons in the Sun, the density of which is large in the solar core and drops to zero as the neutrinos propagate out of the Sun, allows for matter-enhanced mixing to occur. Electron-type neutrinos emitted in the solar core are free to interact via $W^{\pm}$ exchange with solar electrons. It is the forward scattering amplitude of this process which produces matter-enhanced mixing, and is termed the MSW effect after the original researchers.

The equations describing vacuum oscillations are easily generalized to describe MSW oscillations. The mass matrix serving as a Hamiltonian for the two-state neutrino system is expanded to

$$M = M_0 + M_{matter},$$ (2.86)

where the new (matter-enhanced) term is given by

$$M_{matter} = \sqrt{2}G_F n_e |\nu_e\rangle\langle\nu_e|,$$ (2.87)

where G_F is the Fermi constant, n_e is the electron number density, and the ν_e projection operator indicates that only electron-type neutrinos take part in the process.

The behavior in time of the flavor eigenstates is given by a generalization of Eq. 2.84,

$$i\hbar \begin{pmatrix} c_e(t) \\ c_\mu(t) \end{pmatrix} = \pm\frac{\Delta_M}{2} \begin{pmatrix} -cos2\theta_M & sin2\theta_M \\ sin2\theta_M & cos2\theta_M \end{pmatrix} \begin{pmatrix} c_e(t) \\ c_\mu(t) \end{pmatrix},$$ (2.88)
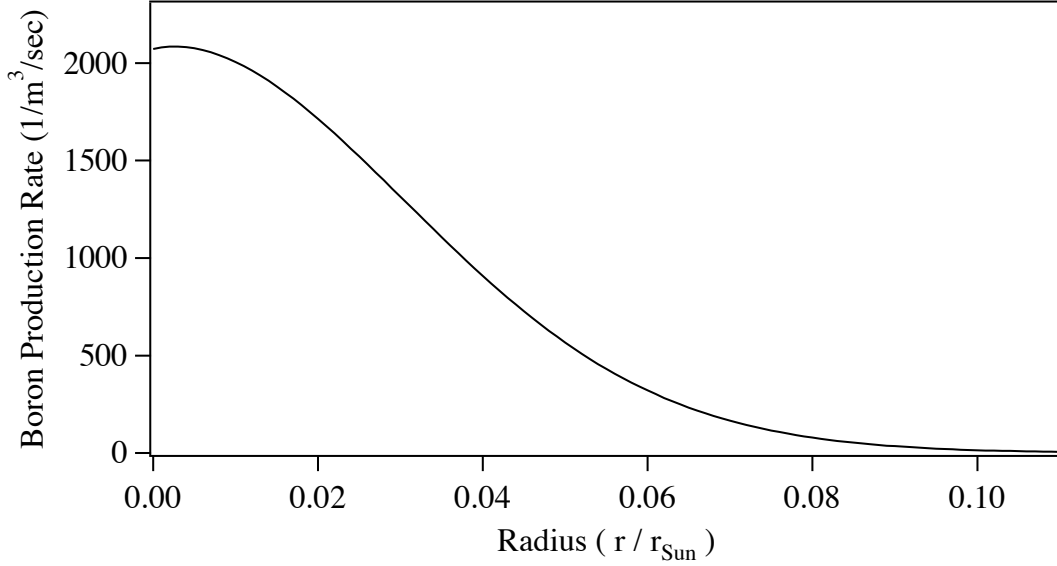
Figure 2.1. The production of ^{8}B due to nuclear fusion in the solar core, as a function of distance from the solar center. This graph is a result of a recent publication of the Standard Solar Model by Bahcall et al. [6].

where Δ_V is replaced by Δ_M,

$$\Delta_M = [(\Delta_V cos2\theta_V - \sqrt{2}G_F n_e)^2 + (\Delta_V sin2\theta_V)^2]^{1/2}, \tag{2.89}$$

and the new mixing angle in matter θ_M is given by

$$tan2\theta_M = \frac{tan2\theta_V}{1 - \frac{L_V}{L_e}sec2\theta_V}, \tag{2.90}$$

and the neutrino-electron interaction distance L_e is introduced,

$$L_e = \frac{\sqrt{2}\pi\hbar c}{G_F n_e}. \tag{2.91}$$

The crucial result of the MSW effect is that there exists a critical electron number density, the resonance density n_e, given by

$$n_e = \frac{|\Delta m^2|c^4 cos2\theta_V}{2\sqrt{2}G_F E}, \tag{2.92}$$

whereby mixing between ν_e and ν_μ is maximized due to a large matter mixing angle, $\theta_M = \pi/4$. Note that, even for small vacuum mixing angles, θ_V, the resonance condition can occur. Specifically, the resonance density does occur in the Sun.

2.3.3 ^{8}B Neutrinos from the Solar Core

The presence of the MSW effect, and of the resonance electron density in the Sun, allows for ν_e neutrinos to oscillate to ν_μ and ν_{tau} neutrinos as they propagate from the Solar core to detectors on Earth. This section will briefly consider the effect of neutrino oscillations on neutrinos from ^{8}B.

I have written code which numerically propagates neutrinos from various coordinates in the Sun, where they are emitted from ^{8}B β-decay. An understanding of the ν_e component of ^{8}B neutrinos after they have traversed the Sun to detectors on Earth depends on where in the Sun the neutrinos were emitted. Fig. 2.1 shows the production rate of ^{8}B by nuclear fusion as a function of distance from the solar center. This information was obtained from a recent publication of the Standard Solar Model [6].

Integrating over the ^{8}B production rate as a function of location, and propagating the neutrinos isotropically, I arrive at the probability that a ν_e emitted in the Sun behaves as a ν_e as it reaches the Earth. This result has been obtained countless time before, with greater accuracy. My approach is incomplete in that it ignores for example, the day-night effect resulting from the MSW effect as the neutrinos propagate through the Earth. The survival probability of ν_e from ^{8}B β decay is shown in Fig. 2.2.

2.3 Weak Interactions in Nuclei

The early development of the theory of weak interactions was instigated and perpetuated almost entirely by investigations of nuclear β-decay and other low energy processes. Lee and Yang proposed in 1956 that weak processes may not conserve parity [37], providing a solution to the $\theta - \tau$ puzzle. Soon after, in 1957 Wu et al. discovered that parity was in fact almost maximally violated in the β-decay of ^{60}Co [38]. Early measurements of the β-ν angular correlation in β-decay [39, 40, 41], carried out between 1959 and 1963, indicated a $\mathbf{V} - \mathbf{A}$ Lorentz structure of
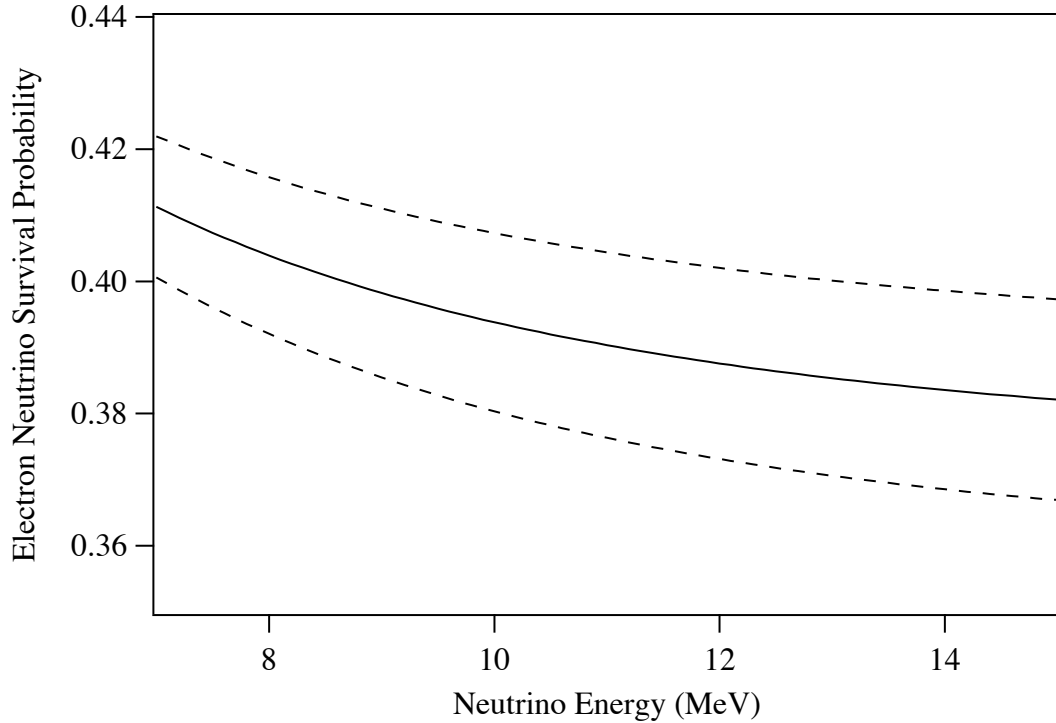
Figure 2.2. The survival probability of ν_e neutrinos emitted from ^{8}B β-decay in the Sun as a function of neutrino energy. The solid line indicates the survival probability using the best values [25] of θ_V and Δ_m^2 available from both solar neutrino and terrestrial reactor experiments. The dotted lines indicate the 1σ uncertainties due to uncertainties in θ_V and Δ_m^2. Note that the energy range is consistent with the threshold of typical water-Cerenkov detectors.

weak currents. The 1964 discovery by Cronin and Fitch of CP violation in neutral kaons [42] was another important discovery.

This section presents a development of nuclear β-decay sufficient to motivate the calculation of the ^{8}B neutrino spectrum, the main result of this thesis. As much as possible, the discussion will derive from the results of Section 2.1.

2.3.1   General Considerations

In the discussion of the Standard Model in Section 2.1, the part of the Lagrangian concerning the interactions of matter fields with the four gauge fields, Eqs. 2.62-2.65, was derived. Nuclear β-decay changes the charge of the nucleus and hence is described through interactions with the

charged W^+ and W^- gauge fields, described in Eqs. 2.62 and 2.63. The neutral weak current, induced by interactions with the Z^0 gauge field as in Eq. 2.64, represents an important aspect of the Standard Model but plays no role in β-decay.

In the quantized theory the matrix element $\mathcal{M}$ for the process $u \to d + e^+ + \nu_e$, describing β-decay at the quark level, is given by the usual application of the Feynman rules:

$$\mathcal{M} = -g^2 V_{ud} \ \bar{u}_d \gamma_\lambda (1 - \gamma_5) v_u \left(\frac{-g^{\lambda\rho} + \frac{q^\lambda q^\rho}{m_W^2}}{q^2 - m_W^2} \right) \bar{u}_{\nu_e} \gamma_\rho (1 - \gamma_5) v_e. \tag{2.93}$$

Here u and v are the positive and negative frequency Dirac fields describing the matter particles, and q is the momentum transfer. The term in parentheses is the W-boson propagator.

In β-decay the momentum transfer, of order $1 - 10$ MeV, is far less than $m_W = 80.4$ GeV, allowing a simplification of the propagator. The quark fields may be replaced by fields representing a nucleus, with $|\alpha\rangle$ representing the initial state and $|\beta\rangle$ the final state. Eq. 2.93 then becomes

$$M = \frac{G_F}{\sqrt{2}} V_{ud} J_{hadron\,\lambda} J_{lepton}^\lambda \tag{2.94}$$

where the hadronic and leptonic charged weak currents, J_{hadron}^λ and J_{lepton}^λ are given by

$$J_{hadron}^\lambda = \langle \beta | \gamma_\lambda (1 - \gamma_5) v_p | \alpha \rangle \tag{2.95}$$

and

$$J_{lepton}^\lambda = \bar{u}_{\nu_e} \gamma^\lambda (1 - \gamma_5) v_e, \tag{2.96}$$

and the newly introduced Fermi coupling constant G_F is given by

$$\frac{G_F}{\sqrt{2}} = \frac{g^2}{m_W^2}. \tag{2.97}$$

Note that the propagator present in Eq. 2.93 is absorbed into the Fermi coupling constant in the low energy approximation of Eq. 2.94, which takes the form of a current-current interaction. The low energy approximation is expressed graphically in Fig. 2.3.

The electromagnetic interaction induces vertex corrections altering the β-decay process, similar to corrections on a QED vertex. It is a textbook problem to calculate the corrections to a
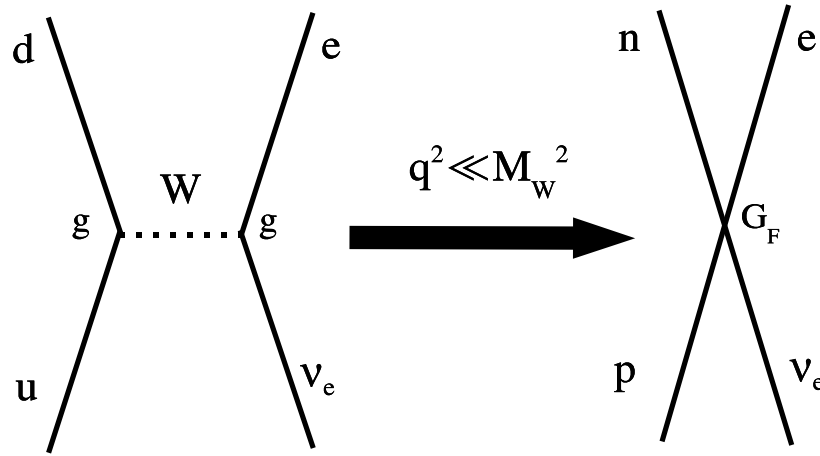
51

Figure 2.3. The Feynman diagrams generating nuclear β-decay. On the left is the diagram associated with the full interaction Lagrangian of the Standard Model, containing two interaction vertices and a W-boson propagator. On the right is the simplified diagram associated with the one vertex Fermi interaction.

leptonic vertex produced by brehmstrahlung and QED vertex corrections; to first order in the fine structure constant, α, the calculation is quite accessible. Such processes give rise to, for example, the electron magnetic moment which is the result of an induced tensor term. Radiative corrections to a nuclear vertex in β-decay are more complicated but, as will be discussed in Chapter 7, the first non-vanishing term in an expansion in α is calculable and independent of nuclear structure.

Corrections induced by the strong interaction, however, are not so tractable. These corrections are not calculable due to the non-perturbative nature of the strong interaction at low energies. Instead they are treated in a phenomenological fashion by expressing the nuclear weak current in the most general form allowed by Lorentz invariance. Note that in the simple $\mathbf{V} - \mathbf{A}$ form of the nuclear weak current, Eq. 2.95, the effects of the strong interaction were implicit in the nuclear wave functions, $|\alpha\rangle$ and $|\beta\rangle$. From this point on, the nuclei are treated as structureless elementary particles and the effects of the strong interaction are described by form factors.

The most general form for transitions between nuclei of arbitrary spin has been outlined by Holstein [43], who has made simplifying approximations and related the results to observable quantities. These results will be discussed in Chapter 6 in the context of the ^{8}B neutrino spectrum.

Presently, the discussion will be simplified by considering only the most general form of the weak current for transitions between two *nucleons*, given by

$$J^\lambda_{hadron} = V_{ud}\overline{u}_\beta \left[f_1\gamma^\lambda + if_2\sigma^{\lambda\rho}g_\rho + f_3q^\lambda - g_1\gamma^\lambda\gamma_5 - ig_2\sigma^{\lambda\rho}q_\rho\gamma_5 - g_3\gamma_5q^\lambda \right] u_\alpha. \tag{2.98}$$

The vector form factors f_i and and axial form factors g_i are functions of q^2, but in the case of β-decay the dependence may be ignored and the form factors evaluated at $q^2 = 0$. In the next sections, symmetry arguments will be applied to characterize these form factors.

2.3.2   Symmetries

As discussed in Section 2.1, a global symmetry implies the existence of a conserved current. In the case of an SU(2) symmetry, the conserved current is the isotopic current of Eq. 2.30. The Standard Model contains an SU(2)$_L$[1] symmetry which, while broken for gauge transformations, remains unbroken globally. The resulting conserved isotopic current plays an important role in β-decay.

The electromagnetic current, J^μ_{EM}, of Eq. 2.65 may be expressed generally for a field ψ with charge Q as

$$J^\mu_{EM} = \overline{\psi}\gamma^\mu Q\psi = \overline{\psi}\gamma^\mu(T_3 + Y)\psi, \tag{2.99}$$

where Eq. 2.59 has been used to relate electric charge to the SU(2)$_L$ and U(1) gauge couplings T_3 and Y. The SU(2)$_L$ component of J^μ_{EM}, denoted by J^μ_3, acts only left-handed fields. Considering ψ now as an SU(2)$_L$ spinor, J^μ_3 takes the form

$$J^\mu_3 = \overline{\psi}\gamma^\mu(1 - \gamma_5)\sigma_3\psi, \tag{2.100}$$

where the $(1 - \gamma_5)$ is explicitly included to indicate the left-handed nature of the current. Expressing the charged weak interaction current, Eqs. 2.62 and 2.63, in similar form gives

$$J^\mu_W \equiv J^\mu_\pm = \overline{\psi}\gamma^\mu(1 - \gamma_5)\sigma_\pm\psi. \tag{2.101}$$

---

[1]From this point on, the SU(2) gauge symmetry of the Standard Model will be referred to as SU(2)$_L$, so labeled because it acts on left-handed fields. This distinction will be made because of the frequent appearance in nuclear physics of isospinors representing nucleons and nuclei. For example, the neutron and proton may be described by an SU(2) isospinor, and ^{8}Li, ^{8}Be, and ^{8}B by an SU(3) isospinor.

It is clear from Eqs. 2.100 and 2.101 that J_3 and $J_\pm$ form two isotriplet currents: a *vector* isotriplet current, $J_i^V = \overline{\psi}\gamma^\mu\sigma_i\psi$, and an *axial* isotriplet current, $J_i^A = \overline{\psi}\gamma^\mu\gamma_5\sigma_i\psi$. The vector current will be considered first.

The Conserved Vector Current

The vector isotriplet current, $J_i^V = \overline{\psi}\gamma^\mu\sigma_i\psi$, is termed the Conserved Vector Current (CVC). When applied to left-handed fields behaving as spinors under $SU(2)_L$, such as the up-down quark spinor, the current is *exactly* conserved in the Standard Model; this follows immediately from global $SU(2)_L$ symmetry.

The $SU(2)_L$ quark spinors are inconvenient in practice since free quarks do not exist in nature. In nuclear physics, it is convenient to arrange nucleons and nuclei into isospin multiplets reflecting approximate symmetries. For example, the neutron and proton have quark contents *udd* and *uud*, respectively. Both represent the ground state of these quark configurations. Assuming the strong interaction treats *u* and *d* quarks identically, the neutron and proton must have nearly equivalent quark wave functions. This idea is supported by the near equality of their masses, $m_n = 939.6$ MeV and $m_p = 938.3$ MeV, with the difference arising predominantly from electromagnetic effects. In analogy to the fundamental $SU(2)_L$ $u - d$ isodoublet, the neutron and proton are likewise arranged into a SU(2) isodoublet. The vector current $J_i^V = \overline{\psi}\gamma^\mu\sigma_i\psi$ is then assumed to operate on the $n - p$ isodoublet. In this formulation, the vector current is not exactly conserved; it is violated due to imperfect isospin symmetry. Nonetheless, it remains an effective tool of nuclear physics.

The original formulation [44] of the CVC hypothesis in 1957, well before the conception of the Standard Model, was proposed to account for the near equality of the weak coupling constants responsible for vector decays such as muon decay and superallowed Fermi decays ($J^\pi = 0^+ \to 0^+$) decays between members of a nuclear isomultiplet. The motivation for CVC was an analogy to electric charge; electric charge is conserved due to a conserved electromagnetic current, so a *weak* charge associated with a conserved weak vector current was postulated. The existence of a conserved weak charge is sometimes referred to as the weak CVC hypothesis. Due to the
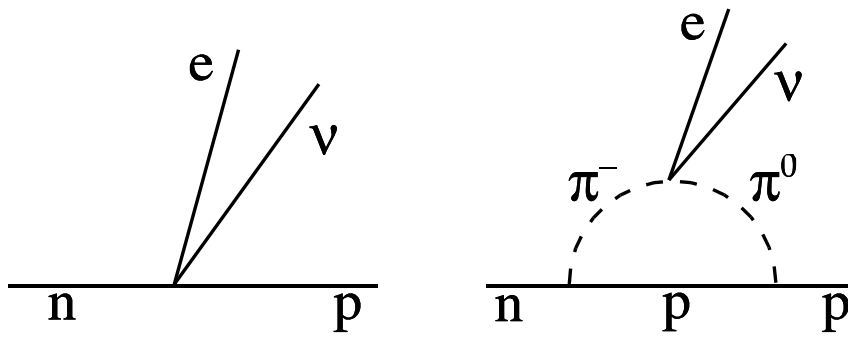
Figure 2.4. At left is the diagram corresponding to the β-decay of a bare nucleon. In addition, the pion contribution to vector (Fermi) β-decay must be considered. The lowest order diagram containing a pion contribution is shown at right.

similar appearance of the vector parts of the charged weak currents and the isovector portion of the electromagnetic current, these three currents were postulated to form an isotriplet, sometimes known as the strong CVC hypothesis.

The weak CVC hypothesis explains the equality of ft-values for all superallowed β-decays, after isospin breaking effects have been considered. It is historically fortunate that V_{ud} is so close to unity, as this causes the coupling constant for superallowed β-decays to be very close to that of muon decay. At the time CVC was proposed, the difference in these coupling constants induced by V_{ud} were smaller than experimental uncertainties.

The weak CVC hypothesis may be understood conceptually at the nuclear level through a simple example. In superallowed β-decay, only the vector portion of the weak current contributes. In the impulse approximation of β-decay, a single nucleon in the nucleus is responsible for the decay. Corrections to this arise from the mesonic contributions, such as pion exchange which mediates the strong interaction between nucleons. Fig. 2.4 shows the Feynman diagram for the β-decay of a bare nucleon, as well as the first order correction given by the β-decay of a nuclear pion. Weak CVC then not only predicts the existence of pion β-decay, but can be used to estimate its frequency [44].

The strong CVC hypothesis indicates that the vector form factors, f_i, of Eq. 2.98, of the hadronic weak current are identical to the vector form factors of the isovector part of the hadronic

electromagnetic current. Considering the neutron-proton isospin doublet as an example, the electromagnetic matrix element, $\mathcal{M}$, linking nucleon states with momenta p and p' and spins s and s' are written

$$\mathcal{M} = \langle p's'|J_{EM}^{\mu}|ps\rangle = \bar{u}_{p's'}\left[C_n\gamma^{\mu} + iM_n\sigma^{\mu\nu}q_{\nu} + S_nq^{\mu}\right]u_{ps} \tag{2.102}$$

for the neutron, and similarly for the proton with $C_n, M_n, S_n \to C_p, M_p, S_p$.

The scalar form factors can be shown to vanish by the requirement that J_{EM}^{μ} is conserved. The tensor form factors, labeled M because they produce the anomalous magnetic nucleon moments, are given by $M_p = 1.79/2m$ and $M_n = -1.91/2m$ where m is the nucleon mass. The vector form factors are labeled C because they produce the interaction field of a normal Dirac particle with a given charge, are $C_p = 1$ and $C_n = 0$.

Consider a SU(2) isospinor, u, containing neutron and proton wave functions, where the proton part is given by $u_p = [(1+\sigma_3)/2]u$ and the neutron part by $[u_n = (1-\sigma_3)/2]u$. Defining the isovector, C^1, M^1, and isoscalar, C^0, M^0, form factors by

$$C^0 = C_p + C_n = 1 \qquad M^0 = M_p + M_n = -\frac{0.12}{2m}, \tag{2.103}$$

$$C^1 = C_p - C_n = 1 \qquad M^1 = M_p - M_n = \frac{3.70}{2m}, \tag{2.104}$$

the electromagnetic matrix element becomes

$$\mathcal{M} = \bar{u}\left[\frac{1}{2}\left(C^0\gamma^{\mu} + iM^0\sigma^{\mu\nu}q_{\nu}\right) + \left(C^1\gamma^{\mu} + iM^1\sigma^{\mu\nu}q_{\nu}\right)\sigma_3\right]u. \tag{2.105}$$

Strong CVC then requires the form factors f_i of the hadronic weak current operating on the proton-neutron isodoublet to be given by $f_1 = C^1 = 1$, $f_2 = M^1 = 3.70/2m$, and $f_3 = 0$.

The CVC hypothesis, incorporated in the Standard Model by its global SU(2)$_L$ symmetry and extended to practical nuclear applications by exploiting isospin symmetries, is a powerful tool in nuclear physics. The existence of a weak vector charge not renormalized by the strong interaction allows important tests of the Standard Model. Measurements of superallowed β-decay rates provide an important experimental test, and the equality of superallowed rates in varying nuclei confirm the weak CVC hypothesis and are used to determine V_{ud}. The strong CVC hypothesis is
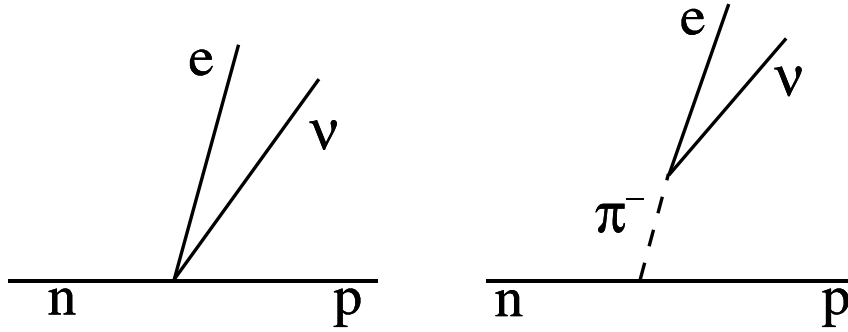
Figure 2.5. At left is the diagram corresponding to the β-decay of a bare nucleon. At right is the lowest order diagram containing a pion contribution to axial (Gamow-Teller) β-decay.

more difficult to test, since weak form factors in β-decay are not easily accessible experimentally. However, strong CVC allows the relatively easy measurements of electromagnetic form factors to be used to infer the analogous weak form factors; this approach is used later in the determination of the ^{8}B neutrino spectrum.

Partially Conserved Axial Current

The axial isotriplet current, $J_i^A = \bar{\psi}\gamma^\mu\gamma_5\sigma_i\psi$, does not play as large a role in nuclear physics as does its vector counterpart, in large part because it is not conserved. This follows immediately from the Dirac equation; for massless Dirac particles a conserved axial current does exist in the classical theory, but the Standard Model contains massive fermions.

There is a more interesting reason why the axial current is not conserved. It is a property of gauge theories that axial currents, which may be conserved in the classical field theory, acquire a divergence when the theory is quantized and radiative corrections are considered. A general discussion is found in Ref. [29]. Here, only a simple approximation of nuclear physics is considered, where the divergence of the axial current is related to properties of the pionic nuclear current which mediates the strong interaction. In this context, the axial current is not conserved because it connects the pion states to the vacuum, as shown schematically in Fig. 2.5. The divergence of the axial current may thus be approximated in terms of the pion decay constant. This approximation is given, in the context of ^{8}B β-decay, in Chapter 6.

Chapter 3

The ^{8}Be Final State: An R-matrix Description

The mass 8 nuclear system offers ample opportunity for experimental tests of nuclear and electroweak physics. A diagram showing mass 8 nuclear energy levels is shown in Fig. 3.1. The instability of mass 8 nuclei is an important characteristic of the system. The ^{8}Be nucleus decays rapidly into α particles, and the short lifetime provides a broad region of excitation energies in ^{8}Be through which nuclear processes, such as β-decays, radiative decays, or α-α scattering may proceed. The likelihood that a given excitation energy in ^{8}Be is populated by a nuclear process is sometimes described phenomenologically by the R-matrix formulation, where a region of excitation energies in ^{8}Be is described in terms of interfering nuclear states. The R-matrix formulation is used in this thesis as a tool to parametrize and describe various experimental data, including the alpha spectrum.

The mass 8 system includes a T=1 isotriplet, containing ^{8}B, so that recoil order effects (described by the Conserved Vector Current and possibly Second Class Currents – as discussed in Chapter 6) may be studied by measuring reaction rates and angular correlations associated with the β-decays and radiative decays of the isotriplet, and the subsequent ^{8}Be breakup into α particles. The instability of the ^{8}Be daughter state increases the potency of experimental tests by
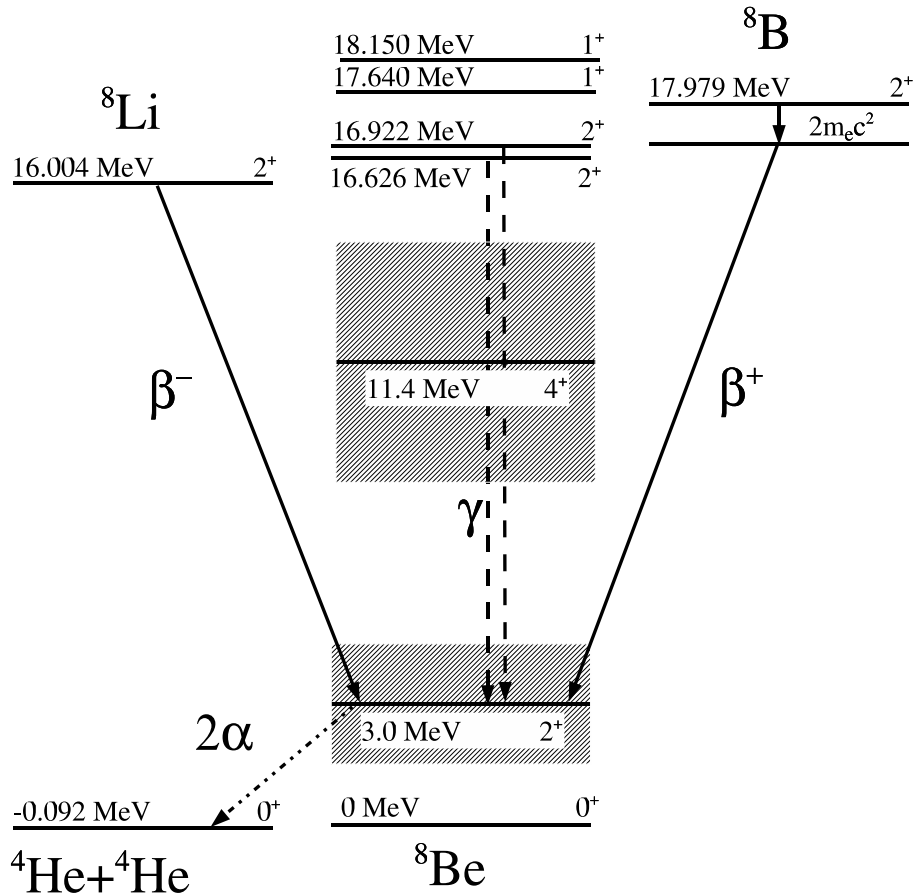
Figure 3.1. Nuclear levels in mass 8 relevant to the β-decays of the ^{8}B and ^{8}Li ground states. Spins, parities, and excitation energies relative to the ^{8}Be ground state are indicated.

allowing, for example, recoil order matrix elements to be characterized as a function of energy release.

This chapter summarizes nuclear transitions in mass 8, concentrating on processes relevant to ^{8}B β-decay. Most importantly, the probability that a given excitation energy in ^{8}Be is populated by ^{8}B β-decay (determined experimentally by measurements of the α spectrum following the ^{8}Be disintegration) is characterized using the R-matrix formulation. Secondarily, the recoil order matrix elements which contribute to the β-decay, and affect the neutrino spectrum, are character-ized. A discussion of past experimental data, analyzed using results from this chapter, is given in Chapter 4. Details and results of the experimental work of this thesis are given in Chapter 5.

3.1 Energy Levels and Transitions in Mass 8

Measurements of s-wave α-α scattering using a helium gas-jet target [45] indicate the ground state of ^{8}Be ($J^\pi=0^+$) has mass 92.04$\pm$0.05 keV above the mass of two α particles, and width $\Gamma=5.57\pm0.25$ eV. All excitation energies (E_x) in mass 8 are given relative to the ^{8}Be ground state. The ^{8}B ground state has $J^\pi=2^+$, so that the β-transition from ^{8}B to the ^{8}Be ground state (and isospin analog transitions) is second forbidden and should be highly suppressed. The presence of the ^{8}Be ground state is thus ignored in this work.

The broad ^{8}Be state ($J^\pi=2^+$) near $E_x=3.0$ MeV excitation energy with approximate width $\Gamma=1.5$ MeV is discernible from d-wave α-α scattering [46], and is responsible for the peak of the ^{8}B and ^{8}Li β-delayed alpha spectra [47, 48, 49, 50].

A ^{8}Be state ($J^\pi=4^+$) near $E_x=11.4$ MeV excitation energy with approximate width $\Gamma=4.0$ MeV [51] has been identified and is included in Fig. 3.1 for completeness. Its existence is ignored in this work, again because transitions from ^{8}B to this state are second forbidden.

Two $J^\pi=1^+$ states with excitation energies $E_x=17640\pm1$ keV and $E_x=18150\pm4$ keV and widths $\Gamma=10.7\pm0.5$ keV and $\Gamma=138\pm6$ keV [51], respectively, are shown in Fig. 3.1. These states are included because the ^{8}B and ^{8}Li allowed β-decays could conceivably proceed partially through these levels; this possibility has been considered [46] using the R-matrix approach, where it was found inclusion of these 1^+ states was not necessary to describe experimental data.

The ^{8}B ($J^\pi=2^+$,$T_z=+1$) and ^{8}Li ($J^\pi=2^+$,$T_z=-1$) ground states constitute two states of a T=1 isotriplet, lying at energies 17.9798 MeV and 16.0052 MeV, respectively [51]. The analogous ^{8}Be isospin state ($T_z=0$) is mixed between a doublet of energy eigenstates with excitation energies 16.626$\pm$3 keV and 16922$\pm$3 keV and widths $\Gamma=108.1\pm0.5$ keV and $\Gamma=74.0\pm0.4$ keV, respectively [51]. This doublet provides a method to study interference effects between two isospin mixed levels, using for example the ^{12}C(γ,α)^{8}Be(2α) [52] and ^{10}Be(d,α)^{8}Be(2α) [53] reactions. The amount of isospin mixing between the levels may be approximated simply by a comparison

of the widths of the states, since α decay is by far the dominant channel and $\Delta T=1$ α decays are forbidden.

The most crucial observable in the determination of the ^{8}B neutrino spectrum, the subject of this thesis, is the α energy spectrum of the ^{8}B(β^+)^{8}Be(2α) decay chain. The α energy spectrum can be used to determine the probability that a given excitation energy in ^{8}Be is populated by the ^{8}B β-decay. Then, assuming the ^{8}B β-decay is completely allowed, the ^{8}B neutrino spectrum is inferred by simply convoluting an allowed (statistical) spectrum over the allowed energy releases. Complications to this arise from recoil order contributions to the β-decay, causing the neutrino energy spectrum to deviate from the allowed approximation.

Recoil order matrix elements relevant to ^{8}B β-decay may be deduced by measurements [54, 55, 56, 48] of radiative transitions from the T=1 analog state in ^{8}Be, split between the energy doublet near 16 MeV, to the broad state at 3 MeV. The CVC hypothesis is used to equate radiative decay matrix elements, parametrized using the R-matrix formulation, to the weak magnetism (and possibly weak electricity) matrix elements contributing to ^{8}B β-decay. Measurements [57, 58, 59] of the β-α angular correlation as a function of β-particle energy provide an independent method of determining these matrix elements. An R-matrix parametrization of the weak magnetism matrix element is given in this chapter. A full discussion of past recoil order experiments, and their implications for the ^{8}B neutrino spectrum, is given in Chapter 6.

3.2   R-matrix Description of Mass 8 Nuclear Transitions

The many-level R-matrix formalism has previously been used to parametrize data involving the broad ^{8}Be state, including the alpha decay spectrum following ^{8}B β^+ decay [60, 46, 61, 49, 62]. The application of the R-matrix to β decay is an approximation, and the physical significance of R-matrix fit parameters is not clear. In principle, it is possible to deduce the ^{8}B β^+ decay strength function directly from the measured α spectrum without resorting to R-matrix formalism. The R-matrix approach, however, gives a good fit to the observed α spectrum

and provides a convenient method for propagating systematic uncertainties in the α spectrum to the neutrino spectrum. Furthermore, systematic uncertainties in the α spectrum dominate the statistical uncertainties, justifying the representation of the data by a smooth function.

The R-matrix formalism is adopted then as a convenient way to characterize experimental data. Before an R-matrix description of ^{8}B β-decay can be given, the Coulomb functions must be developed.

3.2.1   Coulomb Functions

The R-matrix formulation of ^{8}B β-decay makes use of factors arising from the electromagnetic interaction of two α particles. The interaction is quantified by the Coulomb equation

$$u''(\rho) - [l(l+1)\rho^{-2} + 2\eta\rho^{-1} - 1]u(\rho) = 0, \tag{3.1}$$

where the primes indicate differentiation with respect to the scaled distance variable ρ. The notation here follows Ref. [63], where ρ is defined as

$$\rho = kr, \tag{3.2}$$

where k is the classical wave number,

$$k = (\frac{2M_{2\alpha}E}{\hbar^2})^{1/2}, \tag{3.3}$$

r is the radial separation of the particles, E is the energy of relative motion of the α particles, and $M_{2\alpha}$ is the reduced mass of two α particles. The variable η is given by

$$\eta = \frac{Z_1 Z_2 e^2 M_{2\alpha}}{\hbar^2 k}, \tag{3.4}$$

where Z_1 and Z_2, generally, are the charges of the interacting particles.

The functions F(ρ) and G(ρ) are defined as the solutions of Eq. 3.1 for $l = 2$ α particles which are regular and irregular at $r = 0$, respectively. The solutions were calculated by numerical integration of Eq. 3.1, and applying the asymptotic forms

$$F(\rho) \equiv sin(\rho - \eta log2\rho - \frac{1}{2}l\pi + \sigma_l), \tag{3.5}$$
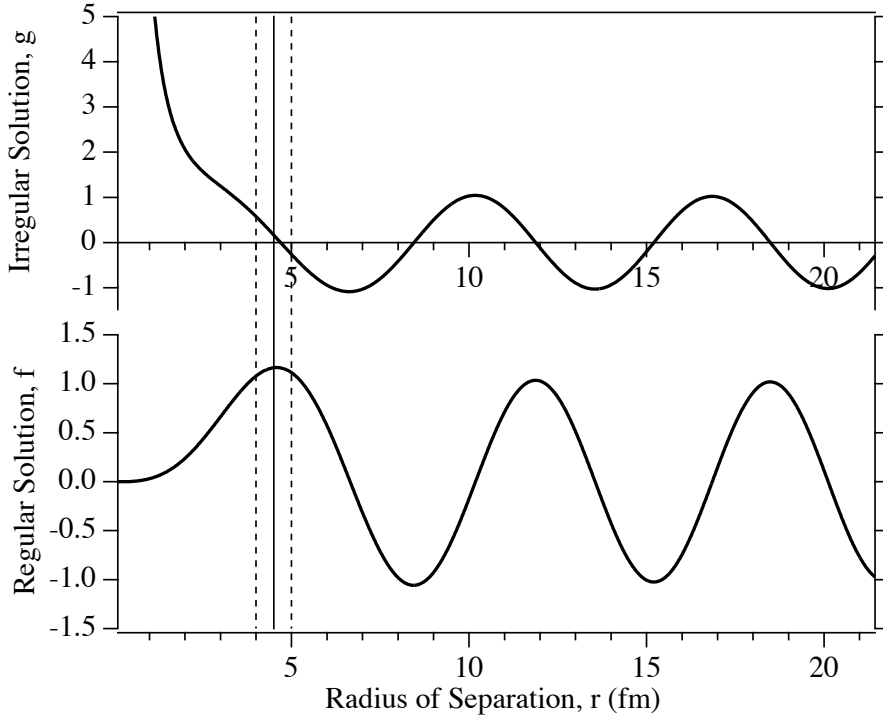
Figure 3.2. The regular and irregular solutions of the Coulomb equation, F and G, for l=2 α particles with a relative energy of motion of 3.0 MeV. The horizontal axis is given in terms of radial distance of separation, r. The functions are evaluated at the chosen matching radii of r_c=4.5±0.5 fm, indicated by horizontal lines.

$$G(\rho) \equiv cos(\rho - \eta log2\rho - \frac{1}{2}l\pi + \sigma_l), \tag{3.6}$$

where σ_l is the phase of the gamma function,

$$\sigma_l = arg\Gamma(1+l+i\eta), \tag{3.7}$$

which also must be solved numerically.

The solutions were calculated using Mathematica. Sample solutions are shown in Fig. 3.2.

As in previous works [46, 49, 62], the Coulomb functions are evaluated at matching radius r_c=4.5 fm, with an uncertainty of 0.5 fm. The penetrability and shift factors, $P(E_x)$ and $S(E_x)$, are defined as [63]

$$P(E_x) = \sqrt{\frac{2M_{2\alpha}E_x}{\hbar^2}} \frac{r_c}{F(r_c)^2 + G(r_c)^2} \tag{3.8}$$
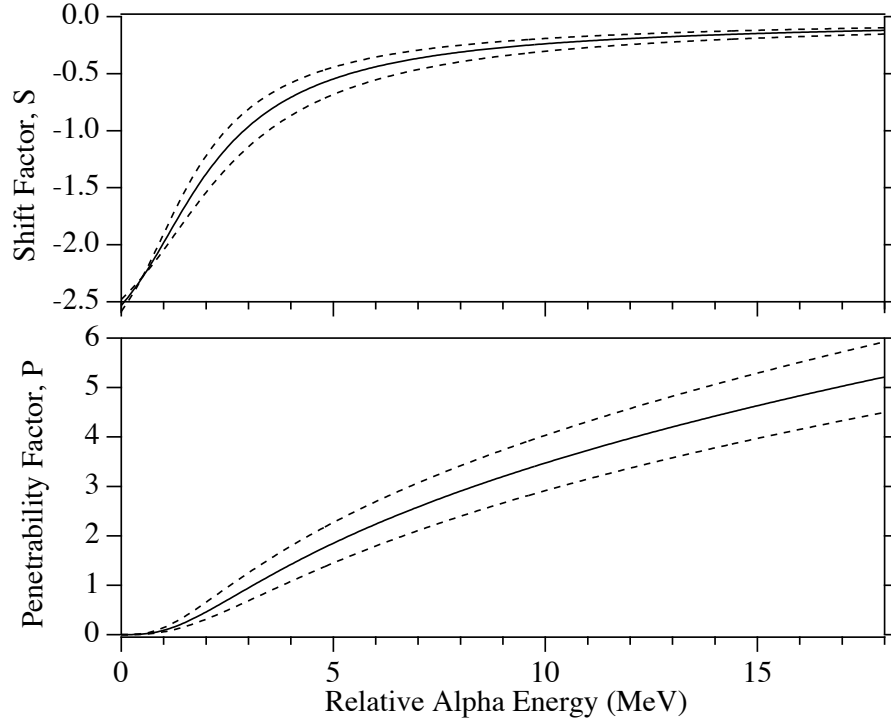
Figure 3.3. The shift and penetrability functions, *S* and *P*, as functions of the energy of relative motion of the α particles. The solid lines indicate the values when the solutions of the Coulomb function, *F* and *G*, are evaluated at a matching radius r_c=4.5 fm. The dashed lines correspond to variations induced by the uncertainty in r_c, Δr_c=0.5 fm.

and

$$S(E_X) = \sqrt{\frac{2M_{2\alpha}E_x}{\hbar^2}} \frac{r_c[F(r_c)F'(r_c) + G(r_c)G'(r_c)]}{F(r_c)^2 + G(r_c)^2}. \tag{3.9}$$

The shift and penetrability factors appear directly in R-matrix description of decay processes involving ^{8}Be, and are shown as a function of the α particles energy in Fig. 3.3.

3.2.2   R-Matrix Description of Beta Decay

In ^{8}B β-decay, the ^{8}B ground state undergoes an allowed β$^+$ transition to a broad range of excitation energies in the α unstable ^{8}Be daughter. I define the ^{8}B β$^+$ decay **strengthfunction** as the probability that a given differential range of excitation energies in ^{8}Be will be populated. As stated previously, the strength function is determined by measurements of the α particle energy

spectrum following the breakup of the daughter ^{8}Be nucleus, and is necessary to construct the neutrino spectrum.

In the R-matrix approximation, the β^+ decay of ^{8}B proceeds with varying strength through a region of interfering nuclear states in ^{8}Be which immediately decay into α particles. Each state is characterized by an excitation energy, $\mathcal{E}_j$, a *reduced width*, γ_j, and a β^+ decay strength quantified by Fermi and Gamow-Teller matrix elements, $\mathcal{M}_{Fj}$ and $\mathcal{M}_{GTj}$.

As discussed previously, only 2^+ states in ^{8}Be are considered. A numerically accurate R-matrix fit to the observed α spectrum requires the three 2^+ states in ^{8}Be shown in Fig. 3.1, as well as one phenomenological *background state* approximating the combined effect of all higher-lying 2^+ states. It has been shown [46, 62] that R-matrix fits using only these four states were sufficient to describe previous experimental data.

The broad state with excitation energy near 3 MeV and width of about 1.5 MeV, responsible for the peak of the observed α spectrum, is labeled (j=1). The excitation energy, $\mathcal{E}_1$, and reduced width, γ_1, are considered free fit parameters. Shell-model considerations [64] indicate no significant Fermi decay strength to this level, as discussed in Ref. [59] which reports measurements of the β-ν-α correlations in ^{8}B and ^{8}Li consistent with a pure Gamow-Teller decay. We take the Fermi decay strength to vanish, $\mathcal{M}_{F1}$=0, while the Gamow-Teller matrix element, $\mathcal{M}_{GT1}$, is a free parameter.

The nearly degenerate doublet with excitation energies 16.626 and 16.922 MeV [51], which are almost maximally mixed in isospin, are labeled (j=2,3). We describe the isospin mixing of the doublet using the standard formulation [60] and consider the energy eigenstates ψ_2 and ψ_3 in terms of the isospin eigenstates ϕ_A (T=0) and ϕ_B (T=1),

$$\psi_2 = \alpha\phi_A + \beta\phi_B, \quad \psi_3 = \beta\phi_A - \alpha\phi_B, \tag{3.10}$$

where α and β are mixing parameters with $\alpha^2 + \beta^2 = 1$. Since α decays from a T=1 state are forbidden, the parameters α and β may be approximated from the level widths,

$$\alpha^2 = \Gamma_2/(\Gamma_2 + \Gamma_3), \quad \beta^2 = \Gamma_3/(\Gamma_2 + \Gamma_3). \tag{3.11}$$

65

An accurate R-matrix description of the alpha spectrum requires $\alpha,\beta > 0$. The energies, $\mathcal{E}_2$ and $\mathcal{E}_3$, and reduced widths, γ_2 and γ_3, of the doublet are well constrained by α-α scattering experiments [65] and are held constant.

The decomposition of the doublet into its component isospin eigenstates allows a simplified description of the Fermi and Gamow-Teller strengths. The T=0 state, ϕ_A, has a Gamow-Teller strength treated as a free parameter, $\mathcal{M}_{GTA}$. The T=1 state, ϕ_B, is the isospin analog of the ^{8}B and ^{8}Li ground states and is populated by Fermi decay with a strength given by the superallowed Fermi matrix element, $\mathcal{M}_{FB}=\sqrt{2}$. The Gamow-Teller decay to the T=1 component, or Fermi decay to the T=0 component, may be nonzero due to isospin breaking but has been estimated to be negligible [66] in this context, as discussed in Ref. [46]. Hence we take $\mathcal{M}_{GTB}=0$ and $\mathcal{M}_{FA}=0$. The matrix elements of the isospin eigenstates are then related to the matrix elements of the energy eigenstates by Eq. 3.10,

$$\mathcal{M}_{F2} = \beta\mathcal{M}_{FB}, \quad \mathcal{M}_{F3} = -\alpha\mathcal{M}_{FB}, \tag{3.12}$$

and

$$\mathcal{M}_{GT2} = \alpha\mathcal{M}_{GTA}, \quad \mathcal{M}_{GT3} = \beta\mathcal{M}_{GTA}. \tag{3.13}$$

The background state labeled (j=4) has an excitation energy held fixed to a value near that used in recent works [49, 62, 46], $\mathcal{E}_4$=37.0. The parameter $\mathcal{E}_4$ could be allowed to float, but the quality of the fit is very weakly dependent on its value. The reduced width, γ_4, and the Gamow-Teller matrix element, $\mathcal{M}_{GT4}$, are free parameters. The Fermi strength is taken to be negligible, $\mathcal{M}_{F4}$=0.

The $P(E_x)$ and $S(E_x)$ are the penetrability and shift factor arising from the regular and irregular solutions of the Coulomb equation of L=2 α particles, defined in Ref. [63]. As in previous works [46, 49, 62], we evaluate the Coulomb functions at matching radius r_c=4.5 fm, and choose the boundary condition, B, to be $S(\mathcal{E}_1)$.

The R-matrix approach gives a parametrization of the ^{8}B β^+ decay strength function, indi-

cating the probability that ^{8}Be is populated at a given excitation energy, E_x. The function takes the form [60]

$$\frac{dN}{dE_x} = \left(\frac{Nt_{1/2}}{6166}\right) f_\beta(E_x)\left(a^2(E_x) + c^2(E_x)\right). \tag{3.14}$$

Here N is the total number of observed decays,

$$N = \int \frac{dN}{dE_x} dE_x. \tag{3.15}$$

The lifetime of ^{8}B, $t_{1/2}$, is 770 ± 3 msec [51]. The unitless integrated phase space available to the β decay leptons, $f_\beta(E_x)$, including the Fermi function and outer radiative corrections, has been evaluated according to the parametrization given by Wilkinson and Macefield [67]. The Fermi and Gamow-Teller matrix elements, a(E_x) and c(E_x), are parametrized by

$$a^2(E_x) = \frac{P(E_x)}{\pi} \left(\frac{\left|\sum_{j=1}^4 \frac{\mathcal{M}_{Fj}\gamma_j}{\mathcal{E}_j - E_x}\right|^2}{\left|1 - \left(S(E_x) - B + iP(E_x)\right)\sum_{j=1}^4 \frac{\gamma_j^2}{\mathcal{E}_j - E_x}\right|^2}\right) \tag{3.16}$$

and

$$c^2(E_x) = \frac{P(E_x)}{\pi} \left(\frac{\left|\sum_{j=1}^4 \frac{\mathcal{M}_{GTj}\gamma_j}{\mathcal{E}_j - E_x}\right|^2}{\left|1 - \left(S(E_x) - B + iP(E_x)\right)\sum_{j=1}^4 \frac{\gamma_j^2}{\mathcal{E}_j - E_x}\right|^2}\right). \tag{3.17}$$

3.2.3 R-Matrix Description of Weak Magnetism

The radiative decay of the ^{8}B isospin analog doublet in ^{8}Be provides useful information on the magnitude of recoil order matrix elements, which may be quantified using the R-matrix formalism. In previous experiments [54, 55, 56, 48], a ^{4}He beam was directed at a ^{4}He gas cell to excite the doublet in ^{8}Be. The ^{4}He(^{4}He,γ)^{8}Be cross section was measured as a function of beam energy and angle of emission of the γ ray. These measurements determine the widths of the isovector M1 and E2 transitions, $\Gamma_{M1}^{T=1}$ and $\delta_1 = \Gamma_{E2}^{T=1}/\Gamma_{M1}^{T=1}$, as well as the widths of the isoscalar

transitions, $\varepsilon = \Gamma_{M1}^{T=0}/\Gamma_{M1}^{T=1}$ and $\delta_0 = \Gamma_{E2}^{T=0}/\Gamma_{M1}^{T=1}$. The radiative widths are considered as functions of E_x.

The matrix elements responsible for the β-decay of ^{8}B, $c(E_x)$, and the radiative decay analog in ^{8}Be, defined as $b(E_x)$, have drastically different functional dependences on E_x. This was first observed [54, 56] through a comparison of the shapes of the final state distributions in ^{8}Be following the α and γ decays. The form of $b(E_x)$ was later described [48] using the R-matrix approach, which parametrized $b(E_x)$ as an interfering sum of three different matrix elements, $\mathcal{M}_i$, to the three 2^+ levels in ^{8}B shown in Fig. 3.1,

$$b^2(E_x) = \frac{P(E_x)}{\pi} \left(\frac{\left| \sum_{j=1}^{3} \frac{\mathcal{M}_j \gamma_j}{E_j - E_x} \right|^2}{\left| 1 - \left(S(E_x) - B + iP(E_x) \right) \sum_{j=1}^{3} \frac{\gamma_j^2}{E_j - E_x} \right|^2} \right) \tag{3.18}$$

This parametrization of the weak magnetism term, b, is similar in form to that of the β-decay Gamow-Teller element, c. Both of these parameterizations will be applied to discussions of experimental data in the mass 8 decay chain.

Chapter 4

Previous Measurements of the ^{8}B β-delayed Alpha Spectrum

The ^{8}B β decay strength function, defined as the probability that a given excitation energy in the broad ^{8}Be resonance is populated by ^{8}B β-decay, is most easily determined by measuring the alpha particle energy spectrum following ^{8}B β decay. The purpose of this work is to evaluate the strength function from my new measurement of the alpha spectrum, and then to deduce the ^{8}B neutrino spectrum. This chapter deals with previous measurements of the alpha spectrum.

The ^{8}B β-delayed alpha spectrum first attracted interest in the 1930's and 40's because the observed ^{8}Be resonance was not described [68] by a Breit-Wigner shape. An R-matrix approach involving several overlapping levels of ^{8}Be, discussed in Chapter 3, was developed [60] in the 1960's and adequately described the shape of the ^{8}Be resonance. Experimental interest in the alpha spectrum remained high, however, due to the importance of recoil order matrix elements in transitions between states in A=8 nuclei. Recoil order effects were mentioned in Chapter 3 and are discussed in detail in Chapter 6. Prior to 1995, at least five measurements detecting the energy spectrum of single alpha particles emitted following the decay of ^{8}B have been performed [47, 69, 70, 71].

More recently, the importance of the ^{8}B neutrino spectrum as an input in analysis of solar neutrino data has renewed interest [72] in measurements of the single alpha energy spectrum. In the year 2000 a measurement [49] was reported which detected both alpha particles and claimed a significantly improved precision over previous measurements. The experiment on which this thesis is based again measured both alpha particles, and was initially reported in 2003 [50]. A subsequent measurement was reported in 2006 [73].

This chapter gives a discussion of all previous alpha spectrum measurements, the corrections applied to them, and the level of agreement or disagreement between the measurements. The possible existence of systematic effects not identified by the original experimenters is addressed.

4.1 Kinetic Considerations

As mentioned previously, the strength function gives the probability that a given excitation energy in ^{8}Be is populated by ^{8}B β decay. The strength function is described phenomenologically by the R-matrix method given in Chapter 3, and is determined experimentally by measurements of the alpha energy spectrum following the ^{8}Be breakup. This section deals with the relationship between the strength function and the measured alpha spectrum.

When both alpha particles are detected, the alpha spectrum differs from the strength function in two well-defined ways: (1) The strength function is a function of ^{8}Be excitation energy, while the alpha energy spectrum is a function of observed alpha energy. The zero of excitation energy is defined by the ^{8}Be ground state, which is unbound by 92 keV as shown in Fig 3.1. Hence, the alpha spectrum trivially lies 92 keV higher in energy than the strength function. (2) With respect to the strength function, the alpha spectrum is slightly broadened and shifted higher in energy due to the nuclear recoil from the ^{8}B β decay. The leptons emitted in the β decay impart momentum and energy to the ^{8}Be daughter, which is carried away by the breakup alpha particles. This effect is calculable and will be described later in this section.

When only single alpha particles are detected, the alpha energy spectrum differs even further

from the strength function due to two additional effects: (3) Only one alpha particle is detected. Trivially then, the observed single alpha energies will be roughly half of the total alpha energy release. (4) The single alpha spectrum is broadened significantly by a kinematic effect stemming from lepton recoil. The ^{8}Be daughter nucleus, as mentioned in the previous paragraph, is generally in motion with respect to the detectors. The ^{8}Be motion broadens the single alpha spectrum. Previous work has been performed to calculate the magnitude of this effect [46, 62], and it will be discussed in this section.

4.1.1 Nuclear Recoil from the ^{8}B β decay

In nuclear β decay the nucleus is many thousands of times more massive than the emitted β particle, and at least millions times more massive than the neutrino. The mass discrepancy between the nucleus and leptons allows an important simplifying approximation in the treatment of nuclear β decay. In the limit of an infinitely massive nucleus, the nucleus is able to have arbitrarily large amounts of momentum without having any kinetic energy since

$$E = \frac{p^2}{2m} \tag{4.1}$$

at low velocities. Thus, the emitted β particle and neutrino are free to travel in any direction without being constrained by conservation of momentum. The recoil nucleus is able to absorb all the momentum from the leptons *without possessing any kinetic energy itself*. In this heavy nucleus approximation, the β particle and neutrino receive all the energy released in the decay. The complicated kinematics of a three body decay is then reduced to a much simpler two body case.

The approximation of an infinitely heavy nucleus of course is not exact. Considering that energy releases in β decays are of order 1-10 MeV and nuclear masses are of order 10 GeV, Eq. 4.1 indicates the recoil nucleus should possess kinetic energies of a few keV. Detailed studies of the recoil energy spectrum of daughter nuclei, including radiative and relativistic effects, were first carried out [74, 75] in the case of neutron decay. These calculations aided measurements [76] of the recoil proton spectrum designed to extract the β-neutrino angular correlation.
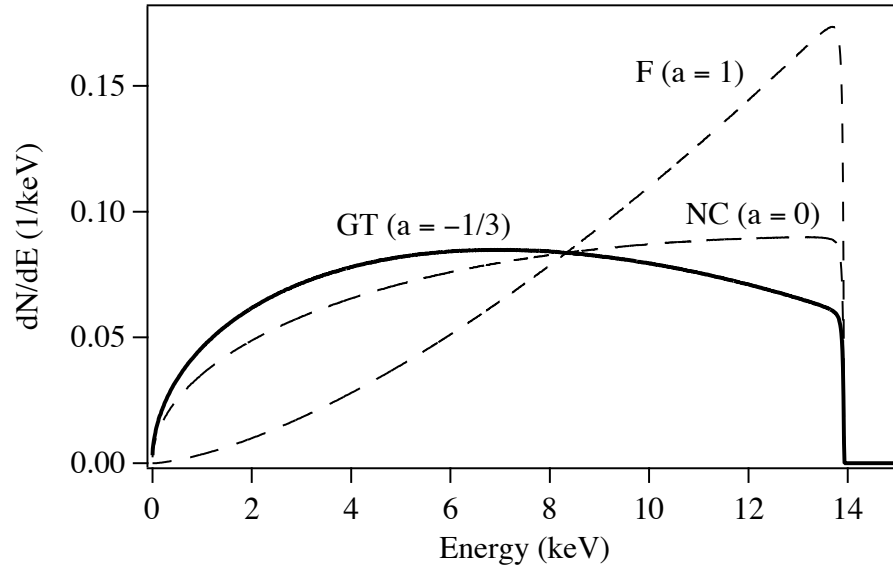
Figure 4.1. Nuclear recoil energy spectrum of ^{8}Be for β decays proceeding to excitation energy 3.0 MeV. The recoil energy spectrum for the ^{8}B Gamow-Teller β decay is shown in bold and labeled **GT**. For comparison, recoil energy spectra are also shown for Fermi decays (**F**) and decays with no angular correlation (**NC**).

The nuclear recoil spectrum of the ^{8}Be daughter, following ^{8}B β decay, depends on the energy released in the β decay. The primary effect of the nuclear recoil is to shift the alpha energy spectrum higher in energy, with respect to the strength function. Nuclear recoil in principle also broadens the observed α particle energy spectrum, but this effect is small due to the large natural width of the alpha spectrum. Decays populating high excitation energies in ^{8}Be have low energy release and hence low nuclear recoil; decays populating low excitation energies will have larger nuclear recoils. The effect of nuclear recoil on the observed α particle energy spectrum is thus more significant at lower alpha energies.

Naturally, β-neutrino angular correlations have a significant effect on the shape of the recoil nucleus energy spectrum. The correlation constant, a, is defined such that the probability P that the β particle and neutrino will be emitted from the nucleus at a relative angle θ is given by

$$P(v, \theta) \propto 1 + a \frac{v}{c} cos\theta, \tag{4.2}$$

where v is the β particle velocity.

A plot of the nuclear recoil energy spectrum is shown in Fig. 4.1 for a ^{8}B β decay proceeding to an excitation energy of 3.0 MeV in ^{8}Be, close to the most likely value. For comparison, spectra are shown for angular correlations $a = -1/3$ (Gamow-Teller decay, largely corresponding to the case of ^{8}B), $a = 1$ (Fermi decay), and $a = 0$ (no angular correlation).

Considerations of nuclear recoil in this work will always make the assumption that $a = -1/3$ for ^{8}B β decay. While, as indicated in Chapter 3, decays proceeding to the highest excitation energies in ^{8}Be may be Fermi decays, the nuclear recoil effect there is of order 0.1 keV, so small as to be negligible in the context of the experimental uncertainties discussed in Chapter 5.

4.1.2 Recoil Broadening of the Single Alpha Spectrum

The nuclear recoil has a further effect on the energy spectrum of single α particles. In the ^{8}Be center of mass frame, conservation of momentum requires the emitted α particles to have identical energies. The recoil ^{8}Be daughter nucleus is generally in motion in the lab frame, however, and the two emitted α particles will generally have different energies. If only one α particle is detected, the energy spectrum will then be broadened. In this section, the effect of recoil broadening on the single α particle spectrum will be shown to be significant.

Recoil broadening is pronounced in the β decay of ^{8}B due to the relatively small nuclear mass (leading to larger nuclear recoil), and a strong correlation between the α, β, and neutrino particles. The correlation is quantified by introducing the β-ν-α *triple correlation A*. The triple correlation is defined so that the probability P that the β particle and α particle are emitted with a relative angle $\theta_{\beta-\alpha}$, the neutrino and α particle with relative angle $\theta_{\nu-\alpha}$, for a β particle with velocity v is given by

$$P(v, \theta_{\beta-\alpha}, \theta_{\nu-\alpha}) \propto 1 + A\frac{v}{c}cos\theta_{\beta-\alpha}cos\theta_{\nu-\alpha}. \tag{4.3}$$

For the ^{8}B Gamow-Teller β decay the expected triple correlation is $A = -1$, as can be seen from angular momentum considerations [62]. An early experiment [77] measuring this quantity found $A = -1.05(12)$ for ^{8}B and $A = -1.01(7)$ for ^{8}Li, consistent with Gamow-Teller transitions.

The strong triple correlation indicates that the β particle and neutrino tend to be emitted in the direction of α particle motion, leading to an increased recoil broadening effect.

The effect of recoil broadening has been quantified for the case of ^{8}B [62], applying a kinematic technique used in the analysis of prompt protons emitted following the β decays of ^{32}Ar and ^{33}Ar [78]. The quantity δE is introduced, so that for two α particles with total energy $2E$, the individual α particles have energy $E + \delta E$ and $E - \delta E$. The recoil broadening effect is the characterized by the probability density

$$\frac{dN}{dE}(x) = \frac{15}{16T_{max}}(1 - 2x^2 + x^4), \tag{4.4}$$

where

$$x = \frac{\delta E}{T_{max}}. \tag{4.5}$$

Here T_{max} is the maximum value of δE allowed by kinematics, given by

$$T_{max}(E_x) = \sqrt{W_0^2 - 1}\frac{m_e}{M}\sqrt{2Qmc^2\frac{M - m - Q}{M - Q}}, \tag{4.6}$$

where E_x is the ^{8}Be excitation energy, m_e is the electron mass, m the alpha mass, M the ^{8}Be mass, $W_0(E_x)$ the β decay endpoint in units of m_ec^2, and $Q = E_x + 92\ keV$.

For this distribution, the full width at half maximum (FWHM) is given by

$$FWHM = 2T_{max}(1 - \frac{1}{\sqrt{2}})^{1/2}. \tag{4.7}$$

Note that these equations are all results of previous work on recoil broadening [62] and are reproduced here for completeness.

The recoil broadening distribution, dN/dE, of Eq. 4.4 is shown in Fig. 4.2. It should be noted that an incorrect expression for dN/dE exists in the literature, and was first produced in an experiment measuring the single α particle energy spectrum following ^{8}Li β decay [79]. This expression was reproduced in a comprehensive R-matrix analysis of mass 8 data [46]. As pointed out in Ref. [62], the expression of Ref. [79] incorrectly assumes the triple correlation to be $A = -1/3$. The incorrect expression for dN/dE is also shown in Fig. 4.2, for comparison.
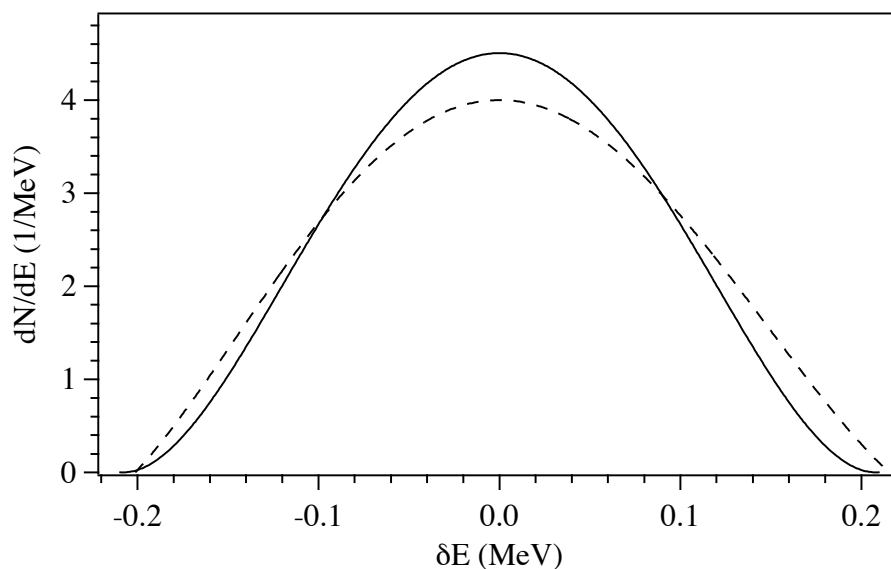
Figure 4.2. The effect of recoil broadening on the single α particle spectrum for β decays proceeding to excitation energy E_x=3.0 MeV in ^{8}Be. The solid line is the result of the most recent work [62], the dashed line is the previous (incorrect) result [79].

The FWHM of the distribution is shown in Fig. 4.3 as a function of excitation energy in ^{8}Be. This figure indicates the magnitude of the broadening effect over the α particle spectrum. Again, the incorrect expression [79] is included for comparison. It should be pointed out that a similar plot of FWHM in Ref. [46] is incorrect; while the shape of the function appears correct in Ref. [46], it is off by a multiplicative factor. This was first pointed out in Ref. [62], which includes figures similar to Figs. 4.2 and 4.3, and was verified by the author of this work.

4.2 Single Alpha Particle Measurements

The previous section dealt with the kinematic considerations necessary to relate the abstract strength function, characterized by the R-matrix formulation, to the observed single α particle energy spectrum. This section will describe previous measurements of the single α particle spectrum, discuss possible experimental uncertainties associated with these measurements, and consider the implications of the measurements and their uncertainties.
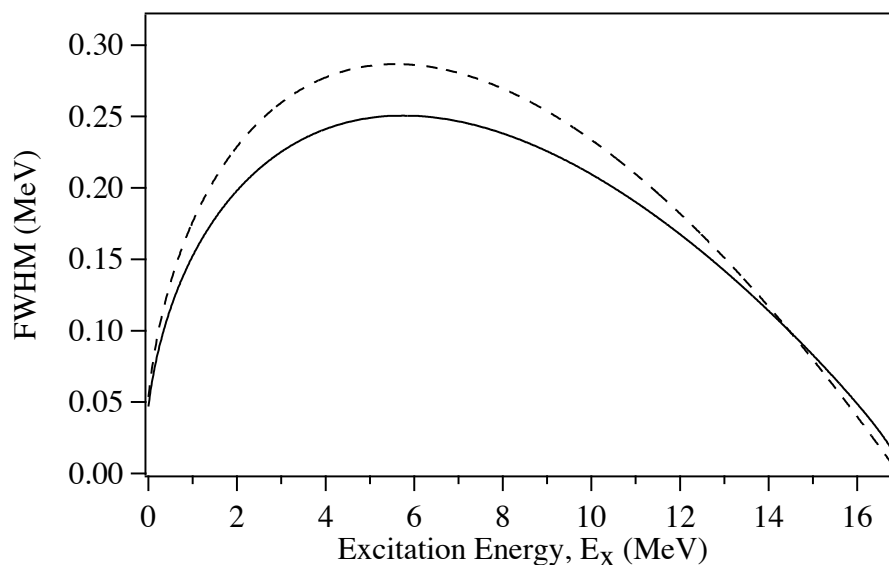
Figure 4.3. The full width at half maximum (FWHM) of the recoil broadening distribution as a function of ^{8}Be excitation energy. The solid line is the result of the most recent work [62], the dashed line is the previous (incorrect) result [79].

4.2.1 The Experiments

At least five measurements of the single α particle energy spectrum have been performed. Here the motivation and experimental technique of each experiment is briefly described.

F. C. Gilbert (1953) This early experiment [80] bombarded 375 MeV α particles on Be to produce both ^{8}B and ^{8}Li which was stopped in a nuclear track emulsion. The energy of the decay α particles by measuring their ranges in a nuclear track emulsion. Clearly this method of production is not optimal; the data used for this α spectrum measurement was a byproduct of an experiment [81] with different scientific goals.

At the time of this experiment, the α spectrum of ^{8}Li had been measured several times [82, 83, 84]. The ^{8}B α spectrum was extracted from the data "for the purposes of (a) checking the similarity of the two mirror nuclei, (^{8}Li and ^{8}B), and (b) searching for a possible new level in the excited (^{8}Be) nucleus" which potentially would appear only in the ^{8}B data due to its higher energy release.

The ^{8}B and ^{8}Li tracks in the emulsion were identified by their characteristic "hammer" or "T" shape resulting from the tracks of two alpha particles emitted at the end of the ^{8}B or ^{8}Li nuclear tracks. The ^{8}B and ^{8}Li were distinguished by the grain density as a function of curvature in the magnetic field. The number of observed events totaled 100 for ^{8}B and 257 for ^{8}Li, and the α particle ranges were translated into energies. There was no observed difference in the ^{8}B and ^{8}Li α spectra due to the limited statistics, and the data is not of sufficient quality to be of more than historical interest at this point in time. The data is sufficient, however, to indicate that the early theoretical model [68] of mass 8 β decay does not properly account for the roughly 15% highest energy α particles in the spectrum.

This experiment is considered here as a single α particle experiment since, although both α particles were detected, the analysis ignored recoil broadening and implicitly assumed both α particles to have the same energy. The difference in track lengths of the α particles in the emulsion was then used as an estimator of systematic uncertainty.

B. J. Farmer and C. M. Class (1959) The second experiment [47] to measure the ^{8}B α spectrum used the ^{6}Li(^{3}He,n)^{8}B reaction. The authors point out that the ^{8}Li had been measured several times previous to their experiment, but the ^{8}B spectrum had been measured only once [80], "no doubt owing to the inability to make B^8 conveniently. This situation was remedied when He^3 (beams) became readily available." The experimental data were obtained using a CsI crystal scintillation detector mounted on a photomultiplier tube, read out through a 256-channel pulse height analyzer. The CsI detector was thin (5 mil) to decrease background from β and γ particles emitted during the mass 8 decay chain. The primary ^{3}He beam bombarded the ^{6}Li target on a beam-on/beam-off cycle created using a pair of beam deflection plates at 6 kV. Data was taken only during the beam-off cycle to avoid background from unrelated events. Calibration of the CsI crystal, the response of which was shown to be highly nonlinear, was performed using external sources at 7 α particle energies between 1 and 9 MeV.

The motivation for this experiment [47] was to test the early theoretical descriptions [68] of the ^{8}B β decay chain. Farmer and class found poor agreement [47] with these early models, but

better agreement with a newer theoretical model [85] which was published back-to-back with the experimental paper [47]. The new model [85] relied on d-wave α-α scattering data as an empirical input to describe the intermediate J^π=2$^+$ ^{8}Be state, and hence is not as complete as the R-matrix descriptions of Chapter 3. However, the model was successful in showing that the 4$^+$ state in ^{8}Be at excitation energy 11.4 MeV (see Fig. 3.1), used in the first theoretical treatment [68], was not necessary to describe the β decay. This is satisfactory, as Farmer and Class indicated [47], because the β decay to the 4$^+$ state is second forbidden.

The Farmer and Class data [47] was published only graphically. The data was graphically extracted for use in a later work [72]. I have obtained this data courtesy of Eligio Lisi, an author of Ref. [72].

G. J. Clark and P. B. Treacy and S. N. Tucker (1969) This experiment [69] used ^{8}B again produced by the ^{6}Li(^{3}He,n)^{8}B reaction, using a 3.5 MeV ^{3}He beam from a Van de Graff accelerator at the Australian National University. The target was enriched (99.6% ^{6}Li) lithium oxide of thickness 20 μg cm^{-2} on a nickel foil backing of thickness 50 μin. All of the ^{8}B products stopped within the Ni backing and a silicon surface barrier detector, mounted behind the Ni backing, was used to observe the α particles. Again, a beam-on/beam-off cycle of period 0.34 sec was created using a rotating shutter which blocked the primary ^{3}He about 3 m upstream from the target. Data was taken using a multichannel pulse height analyzer during the beam-off cycles.

This experiment [69], the first to use a silicon detector, is of some historical interest since it made the first attempts to correct the observed ^{8}B α spectrum for systematic energy loss of α particles in the target backing (dependent on the distribution of the ^{8}B in the Ni) and in the gold surface layer of the silicon detector. This was accomplished using existing straggling data [86] along with measurements of the thicknesses of the nickel backing and gold surface layer using α particles from a ^{228}Th source. The ^{228}Th source was also used to calibrate the detector.

The motivation for this experiment [69] was to collect data of sufficient quality to test the early R-matrix model [60] of Barker introduced the previous year. The experimenters found [69] good agreement with the R-matrix model and extracted a number of level parameters, although

no χ^2 value for the numerical fit is given. The data are presented only in graphical format deemed unusable in a later ^{8}B analysis by Bahcall et al. [72], who found the "data cannot be extracted from (the Clark et al.) Fig. 2 with sufficient precision to be useful for our purposes." I also adopt this viewpoint and lists this experiment only for its historical interest.

D. H. Wilkinson and D. E. Alburger (1971) This experiment [70] used the ^{6}Li(^{3}He,n)^{8}B reaction to produce ^{8}B. The products were implanted into two distinct "catcher foils" (100 and 200 μg cm^{-2} gold evaporated onto 20 μg carbon foils), producing two distinct data sets. After bombardment of an unspecified time the catcher foils were swung in front of a thin Si detector "of thickness just sufficient to stop the most energetic α particles." The detector gain was continuously monitored by a pulser producing pulses which correspond to energy 9 MeV. The gain was shifted by small amounts during the run according to shifts in the pulser peak position. Frequent calibrations using ^{241}Am were also performed.

The motivation for this experiment [70] was to test for second-class currents, explained in this thesis in Chapter 6, by examining the ft-values of the mirror ^{8}B and ^{8}Li β decays. The ^{8}Li α spectrum was hence also measured, using the ^{7}Li(d,p)^{8}Li reaction and bombarding the same catcher foils. It is of interest that this experiment did not require a precise *absolute* energy calibration; instead the *relative* energy of α particles from the ^{8}B and ^{8}Li decays was the crucial quantity. The data sets were corrected for energy loss in the catcher foils (based on approximations of the implantation depth distributions of ^{8}B and ^{8}Li) and in the detector dead layer. Note that this experiment produced two data sets for the ^{8}B α spectrum, one for each catcher foil. The numerical data arising from the thick foil has been reported in Ref [46], that from the thin foil in Ref [61].

L. De Braeckeleer and D. Wright (1995) This experiment, unreported in direct form in the literature, is briefly discussed in Ref [72]. It followed a procedure similar to the Clark et al. and Wilkinson and Alburger experiments, depositing ^{8}B in a thin foil and observing single α particles in a thin Si detector. The motivation for this α spectrum measurement was to provide input for a detailed experimental analysis [48] of radiative decays in the mass 8 iso-multiplet. Data

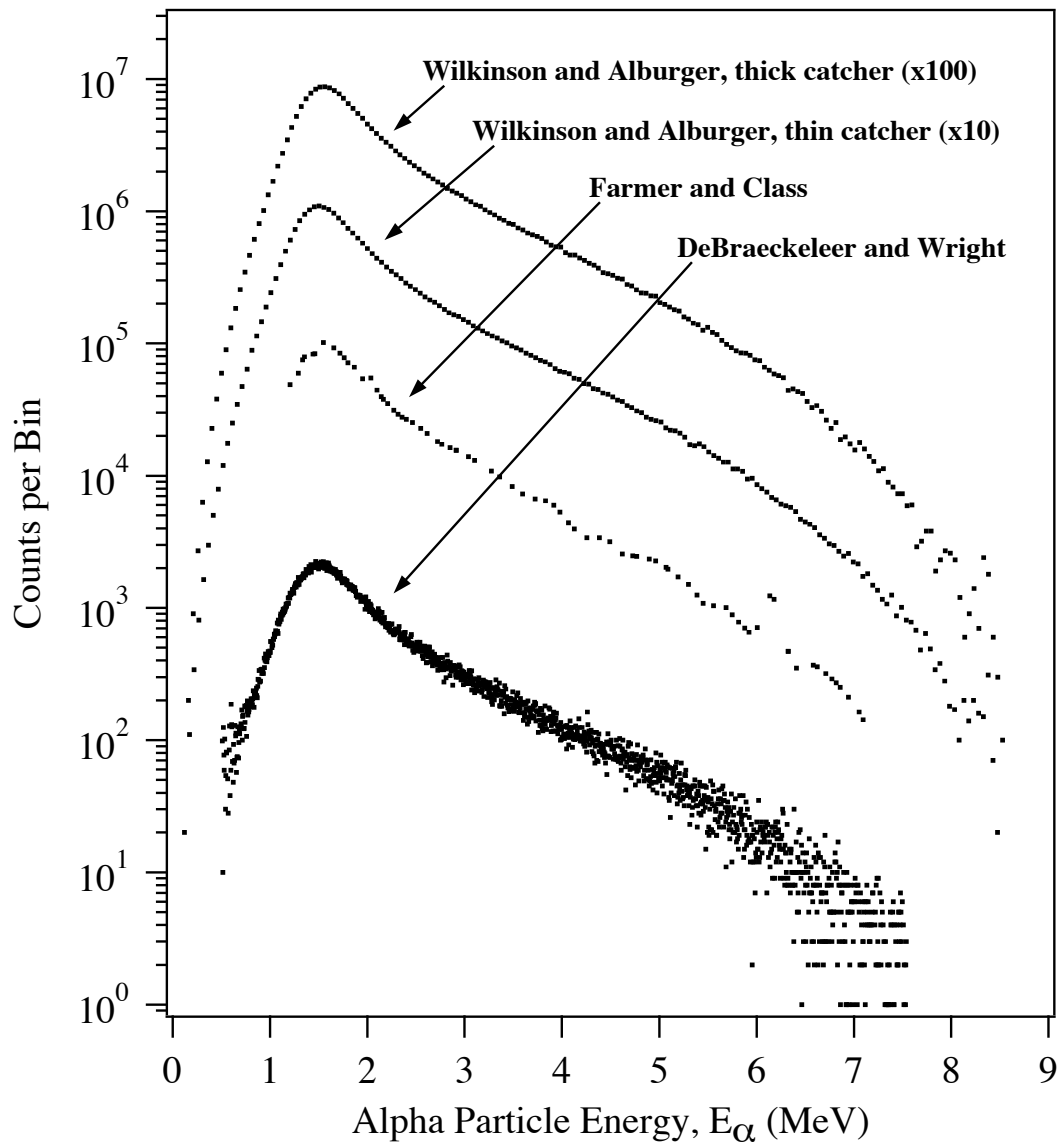Figure 4.4. Four of the single α particle spectrum data sets from the experiments described in the previous section. The two Wilkinson and Alburger data sets have been offset vertically for purposes of presentation. This figure was motivated by and is very similar to Fig. 2 of Ref. [72].

on radiative decays provides information on weak magnetism and second class currents, topics which are discussed in Chapter 6.
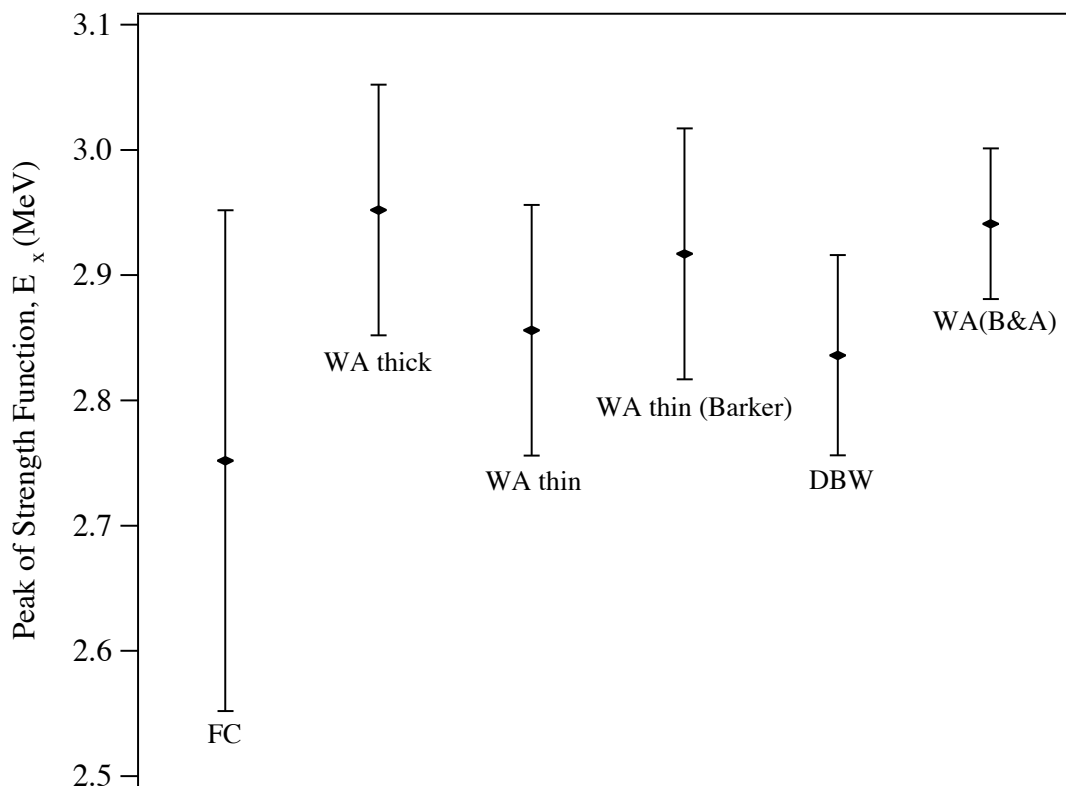
Figure 4.5. The peak of the ^{8}B strength function, as determined by various R-matrix analyses of the four single alpha spectrum data sets. A description of how these values and their uncertainties were obtained is given in the text.

4.2.2   Results and Implications

The ^{8}B α spectrum data from some of the experiments listed above are shown in Fig. 4.4. The Wilkinson and Alburger data sets consist of roughly 2.1×10^6 recorded ^{8}B α particle events (thick catcher) and 2.5×10^6 events (thin catcher). The Farmer and Class data consists of roughly 0.5×10^6 events, and the DeBraeckeleer and Wright data set consists of roughly 1.6×10^6 events.

It is convenient to compare the four data sets shown in Fig. 4.4 by fitting the data using the R-matrix description given in Chapter 3. This technique allows the data to be represented by a smooth function characterized by a few (6-8) fit parameters. The description of the data by a fit function is a legitimate approach for these data sets because uncertainties in the energy scale calibration are far larger than statistical uncertainties. A proper R-matrix description of

the ^{8}B strength function depends on a proper treatment of the kinetic recoil effects discussed in Section 4.1, this was demonstrated conclusively in Ref. [62]. In some analyses of these data sets the kinetic recoil effects have been either treated incorrectly [46] or ignored altogether [61, 72]. Naturally, systematic effects such as α particle energy straggling in the thin films and detector dead layers, and detector lineshape also must be considered in the fitting process. An account of these effects were given by the original experimenters [47, 70] and further discussion and improvement on the treatment of these systematic effects have been made [61, 72, 62].

The two Wilkinson and Alburger data sets, (WA thick) and (WA thin), have been analyzed multiple times [70, 46, 61, 62, 73]. The first R-matrix fit was performed on the (WA thick) data set by Warburton [46] in 1985 using an incorrect treatment of recoil broadening. The value for the peak of the ^{8}B strength function is shown in Fig. 4.5 and labeled "WA thick". The (WA thin) data set was analyzed by Barker [61] in 1989, who attempted to improve on the original treatment of systematic effects [70], resulting in a different energy assignment to each channel of the data. Barker ignored kinetic recoil effects altogether, dismissing them as insignificant [61]. The peak value of the resulting fit is labeled in Fig. 4.5 as "WA thin (Barker)". The (WA thick) and (WA thin) data sets were analyzed simultaneously by Bhattacharya and Adelberger in 2002 using new measurements of α particle straggling and improved lineshapes [62]. They found good agreement between the two sets and their result is shown in Fig. 4.5 as "WA (B&A)".

The (FC) and (DBW) data sets, and the (WA thin) with the original [70] energy calibration have never been subject to an R-matrix analysis in the literature. However, Bahcall et al. [72] produced a comparison of all the existing single α spectrum data in 1996. They found that, in the context of producing a ^{8}B ν spectrum from the α spectrum data, the existing α spectra were indistinguishable when shifted by some offset in the energy scale [72]. They identified the values of these offsets [72] which allow these data sets, labeled as "FC", "DBW", and "WA thin", to be included in Fig. 4.5 by offsetting them from the "WA thick" fit result.

The uncertainties for the values given in Fig. 4.5 were obtained as follows. For "FC" the uncertainty is taken as 200 keV, primarily due to the difficulty in extracting data from the graphical
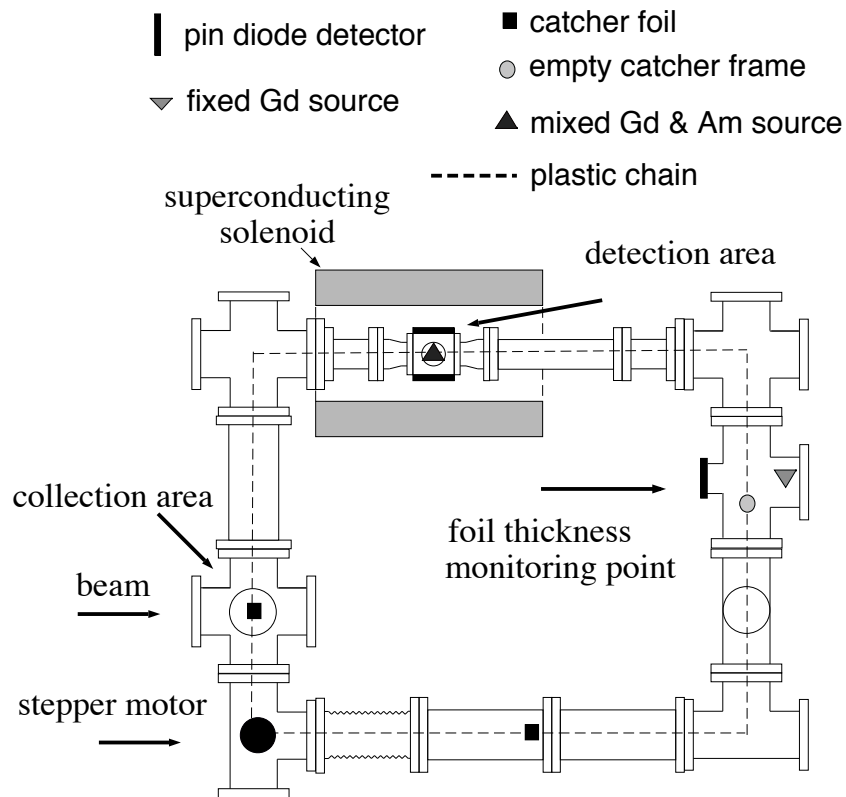
Figure 4.6. A schematic overview of the experimental setup used by Ortiz et al. [49]. This figure is taken directly from Ref. [49].

format of the original work [47], as discussed in Ref. [72]. For "WA thick", "WA thin", and "WA thin (Barker)" the uncertainties are 100 keV, based on the uncertainty in the original work [70] and on later analysis [61, 72]. For "DBW" the uncertainty is explicitly given as 80 keV [72]. Finally, for "WA (B&A)" the uncertainty is 60 keV [62] due to an improved treatment of systematic effects.

4.3   The Coincidence Alpha Particle Measurement

In 2000 Ortiz et al. [49] reported the first measurement of the *coincidence* ^{8}B α spectrum, where the coincidence α particles were detected in two separate detectors. The Ortiz et al. experiment was the first ^{8}B α spectrum measurement performed specifically to determine the ^{8}B neutrino spectrum and was performed with specific attention to calibration of the energy scale.

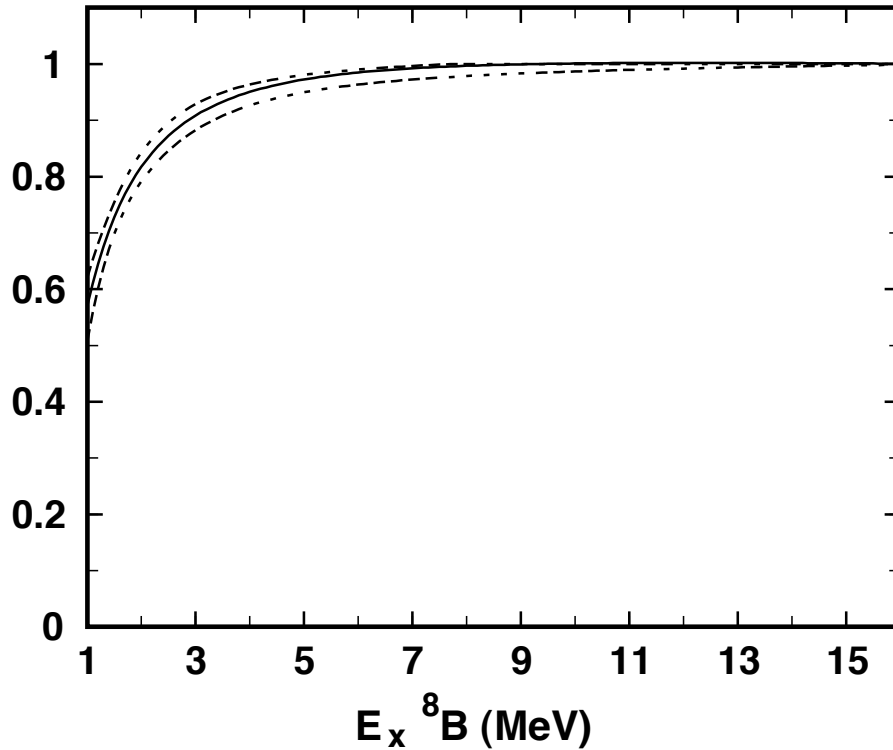Figure 4.7. The detection efficiency of α particles as a function of excitation energy in ^{8}Be, induced by the magnetic field. This figure is taken directly from Ref. [49].

The energy calibration was roughly 10 times more precise than the single α particle experiments described in the previous section.

Ortiz et al. [49] identified several systematic uncertainties that affected the previous ^{8}B α spectrum measurements. Specifically, Ortiz et al. mention "energy summing of the α's with the preceding $β^+$'s, resulting in a distortion of the spectrum," "low energy $β^+$ backgrounds and possible events originating from ^{8}B's implanted in the frame of the catcher foil, correcting for shifts in the α energy due to the recoiling nucleus and α-energy losses at different depths in the catcher foil," and "finally, all previous measurements had to be interrupted to perform detector energy calibrations." These uncertainties had been identified and treated by the original experimenters [47, 70, 48] and others [46, 61, 72], and had led to energy scale uncertainties on the order of 100 keV, as shown in Fig. 4.5 and discussed in the previous section. In addition to the large uncertainty induced by these systematic uncertainties, Ortiz et al. point out that a systematic shift
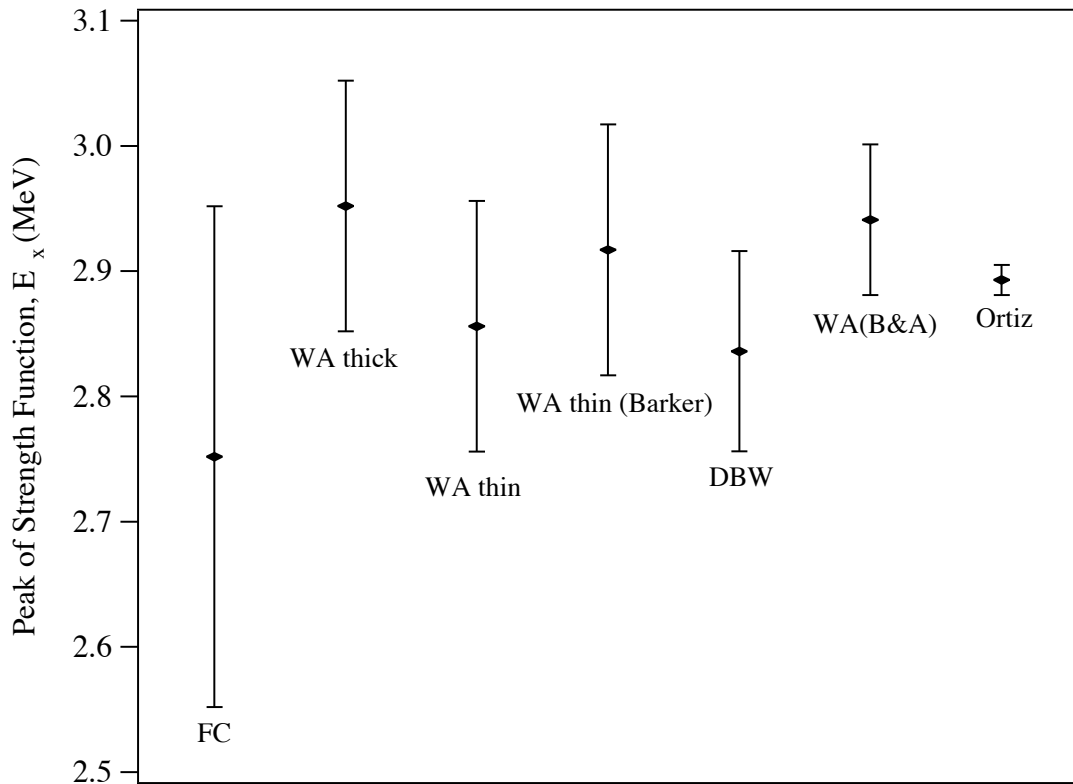
Figure 4.8. The peak of the [8]B strength function, as determined by various R-matrix analyses of the four single alpha spectrum data sets as well as the Ortiz et al. coincidence alpha spectrum data set.

in the spectrum could occur if the uncertainties are not properly dealt with. In order to produce higher quality [8]B α spectrum data and construct a neutrino spectrum more precise than the one obtained [72] based on a analysis of the older single α spectrum data, Ortiz et al. designed an experiment which, they claim, "overcame all the (systematic) difficulties discussed above."

The experimental setup of the Ortiz et al. [49] is shown schematically in Fig. 4.6. As with the previous α spectrum measurements, the experiment used catcher foils (20 μg cm^{-2} of ^{12}C mounted on Al frames) to trap [8]B. The foil was moved to a counting chamber where both α particles from the decay were detected in coincidence using two PIN Si detectors. The counting chamber was located inside a superconducting solenoid that produced a 3.5 Tesla magnetic field. The purpose of the magnetic field was to channel the positrons from the [8]B β decay away from

the detectors, thus eliminating a systematic uncertainty shared by the previous single α particle measurements. The presence of the magnetic field, however, also altered the trajectories of the heavier α particles. A simulation was employed to determine the detection efficiency as a function of α energy, the results of which are shown in Fig. 4.7. Note that the detection efficiency at the peak of the α spectrum (excitation energy in ^{8}Be, E_x, near 3 MeV) is only 90%, and the efficiency drops sharply for lower α particle energies. The inclusion of the magnetic field, then, does eliminate one systematic uncertainty (positron energy summing), but only at the cost of introducing a new uncertainty (detection efficiency).

After passing out of the counting chamber, the catcher foil thicknesses were inferred by measuring the energy loss of α particles from a ^{148}Ga source passing through the foils. At times when no catcher foils were present in the counting area, a mixed source of ^{148}Ga and ^{241}Am was used to calibrate the detectors. Finally, a catcher foil frame, with no carbon foil, was periodically placed in the ^{8}B bombardment area and then moved to the counting chamber to determine whether any α particles from ^{8}B implanted in the frame were being detected.

Ortiz et al. [49] performed an R-matrix analysis of the data, and constructed a neutrino spectrum. The results of the α spectrum measurement are compared with earlier measurements in Fig. 4.8.

Chapter 5

The Alpha Spectrum Measurement

A new measurement [50, 87] of the α-particle energy spectrum following the β-decay of ^{8}B has been performed for this thesis. The technique used in this new alpha spectrum measurement is fundamentally different from the techniques of the previous measurements, described in Chapter 4, and was designed to avoid some systematic effects present in those measurements. This chapter motivates the experimental technique and then describes in detail the experimental procedures, results, and uncertainties of the new alpha spectrum measurement.

5.1 Motivation and Experimental Overview

The experiment was performed at the Argonne Tandem-Linear Accelerator System (ATLAS) at Argonne National Laboratory. A primary ^{6}Li beam was incident on a ^{3}He gas cell in the ATLAS beam line. The reaction products included ^{8}B, produced by the ^{3}He(^{6}Li,^{8}B)n reaction, which exited the gas cell and proceeded down the beam line. The ^{8}B ions were sent through an Enge split-pole magnetic spectrograph, spatially separating ions of different energies. Some ions were incident on a 91±1 μm thick planar Si detector, located in the spectrograph focal plane. The spectrograph was tuned to select ^{8}B ions of the proper energy to be implanted near the midplane

^{8}B Alpha Spectrum Systematic Uncertainties

Experiment (Year)	Si Detector Dead Layer	Source Scattering	β^+ Energy Deposition	Recoil Broadening	Monte Carlo Corrections
Farmer/Class (1960)	☠	☠	☠	☠	
Wilkinson/Alburger (1971)	☠	☠	☠	☠	
DeBraeckeleer et al. (1995)	☠	☠	☠	☠	
Ortiz et al. (2000)	☠	☠			☠

This experiment:
^{8}B implanted into detector, both α particles detected without energy loss in insensitive regions. The β^+ energy deposition minimized by thin (91 mm) Si detector and coincidence requirement. ^{20}Na implanted into detector, provides calibration in the 2.5 - 5 MeV range.

Winter et al. (2002)			☠		

Figure 5.1. This figure identifies the systematic effects present in the various alpha spectrum measurements. The figure is similar to a slide, used during presentations, motivating the experimental technique of implanting ^{8}B and ^{20}Na (for calibration) in a Si detector.

of the detector. The primary ^{6}Li beam was set to a beam-on/beam-off cycle, and the alpha energy release following the ^{8}B beta-decay was measured.

This is the only alpha spectrum measurement to use a ^{8}B source implanted into a detector. The implanted source eliminates the possibility that the alpha particles lose energy outside the sensitive region of the detector, a systematic effect present in the previous measurements.

The implanted source also allows the full energy of both α particles to be detected in a single detector. Previous experiments [47, 69, 70, 71] using a single detector observed only single α particles and were subject to the kinetic broadening effects discussed in Section 4.1. The Ortiz experiment [49] used two detectors and observed both α particles, one in each detector. In this experiment, the observation of both α particles in the same detector increases the energy signal by about a factor of two, causing the peak of the energy spectrum to be nearer the energies of the calibration sources and eliminating the need to consider any kinematic broadening effects.

14.398(7) 2⁺

^{20}Na

β

{
10.840(4) 0.17% 2⁺
10.274(3) 2.88% 2⁺
9.483(3) 0.24% 2⁺

7.8334(15) 0.58% 2⁺
7.4219(12) 15.96% 2⁺
}

α

4.730 0⁺

^{16}O+^{4}He

1.63367(2) 79.44% 2⁺

0 MeV 0⁺
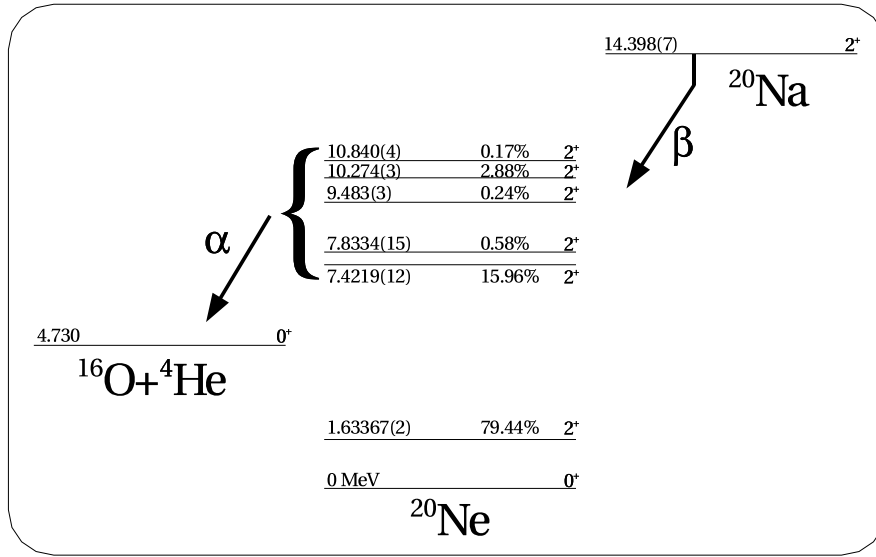
^{20}Ne

Figure 5.2. The relevant energy levels [88] in the ^{20}Na beta-delayed alpha decay. The nuclear energies (in MeV), relative to the ground state of ^{20}Ne, are given for each level along with the J$^{\pi}$ designation. The beta-decay branching ratios are given for the levels in ^{20}Ne.

The systematic effect of positrons depositing energy in the detector cannot be avoided with an implanted source. The effect was reduced by using a thin detector; the detector thickness was just sufficient to stop α particles emitted with the highest possible energy (about 8.5 MeV). The positrons, nearly minimum-ionizing for most of the β-spectrum, deposited a small amount of energy (roughly 20 keV) in the thin detector. The effect of positron energy deposit was further reduced with a coincidence plastic scintillator β-particle detector placed adjacent to the Si detector. The β-detector selected events where the positrons had trajectories close to normal to the Si detector surface, identifying a subset of events with smaller positron energy deposits. The systematic effects present in the various alpha spectrum measurements are summarized in Fig. 5.1.

The system was calibrated with ^{20}Na from the ^{3}He(^{19}F,2n)^{20}Na reaction, produced using a ^{19}F primary beam from ATLAS incident on the same ^{3}He gas cell. The ^{20}Na was also selected by energy using the Enge spectrometer and implanted near the detector midplane. The β-decay of ^{20}Na proceeds with 20% probability to α unstable levels in ^{20}Ne as shown in Fig. 5.2, providing

calibration lines of well-known energy [51]. An external ^{228}Th α source was used to provide additional calibration lines.

5.2 Experimental Technique

The preceeding section gave an overview of the experiment while motivating the use of a source implanted in a detector. This section gives a more detailed description of the experimental technique, from the primary beams produced by ATLAS to the data aqcuisition system. All considerations of systematic uncertainties inherent in the experimental technique are deferred to Section 5.3.

5.2.1 Primary Beams: The ATLAS Accelerator

The ATLAS accelerator at Argonne National Laboratory is the only nuclear accelerator using superconducting components for ion acceleration and focusing. ATLAS was chosen for this experiment because it produces beams of greater intensity and energy (up to roughly 17 MeV per nucleon) than traditional (non-superconducting) accelerators which are limited by heating effects. High beam energies are essential for this experiment because the ^{8}B and ^{20}Na products must have sufficient energy for implantation in the Si detector. A floorplan of the ATLAS accelerator is shown in Fig. 5.3.

The ^{6}Li beam, used to produce ^{8}B, was produced accelerating ^{6}Li ions from an electron cyclotron resonance (ECR) source with a 12 MV linac. This beam was then sent into the 20 MV booster linac, and then into the 20 MV ATLAS linac. The resulting ^{6}Li beam had an energy of 36.4 MeV and an average intensity of 120 pnA over six continuous days of running. The ^{19}F beam, used to produce ^{20}Na for calibration, was produced in a similar fashion and had an energy of 199 MeV and an average intensity of 0.5 pnA over a one day run taking place immediately prior to the ^{8}B run.
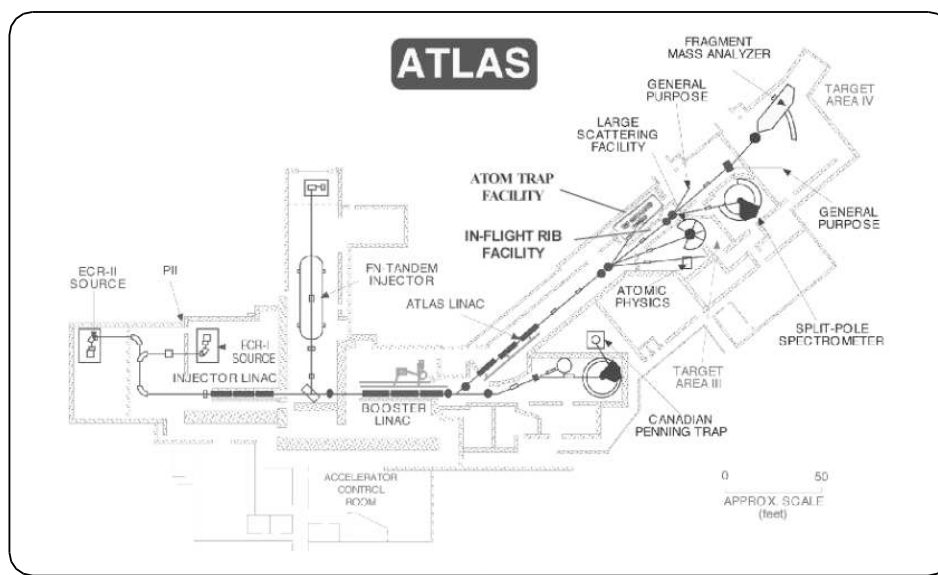
Figure 5.3. The floorplan of the ATLAS accelerator at ANL. This figure was taken from the ANL website [89].

5.2.2 Production Reactions: The ^{3}He Gas Cell

The primary beams were directed onto a ^{3}He gas cell located in the ATLAS beam line. The gas cell was 3.5 cm long and filled with 700 mbar ^{3}He, cooled to 82 K. The gas cell was separated from the beam-line vacuum by 1.3 mg/cm^2 titanium windows. The pressure and temperature in the cell were held constant to $\pm$1%. Several identical gas cells were mounted vertically in the beam vacuum so that, if one failed during bombardment, another could be moved into the beam. The experiment could then continue without breaking the vacuum of the ATLAS beam line. As it happened, the additional gas cells were not needed because the first cell did not fail.

The ^{8}B (t$_{1/2}$=770$\pm$3 ms) beam was produced using the ^{3}He(^{6}Li,^{8}B)n reaction. The use of the heavier nuclear reactant (^{6}Li) as the primary beam allowed the ^{8}B products to have sufficient energy to exit the gas cell and continue down the beam line as a secondary beam, a procedure referred to as the In-Flight Technique [93]. The maximum total cross section [91] for this reaction is roughly 22$\pm$2 mb for a ^{6}Li energy of roughly 12 MeV. This experiment operated at a much higher ^{6}Li bombarding energy (36.4 MeV) to produce a ^{8}B beam of sufficient energy for implantation. The total cross section at the ^{6}Li energy used in this experiment is roughly 4$\pm$1 mb
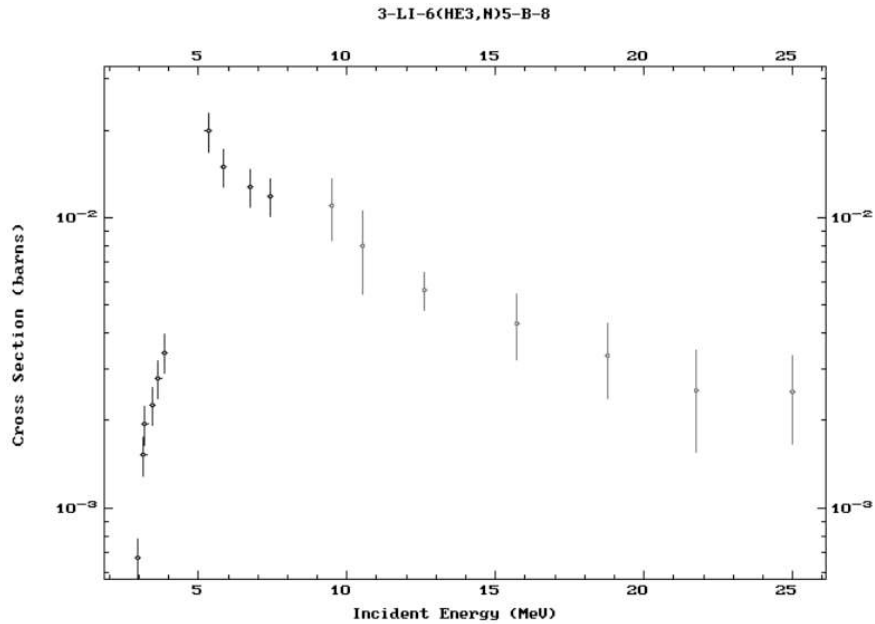
Figure 5.4. Production cross section for the ^{6}Li(^{3}He,n)^{8}B reaction. This plot is taken from the National Nuclear Data Center website [90], which compiled the data of Refs. [91] and [92]. Note that the incident energy listed here is that of a ^{3}He projectile on a stationary ^{6}Li target. The experiment described in this section used the inverse reaction.

[92]. A plot of the total cross section as a function of energy is given in Fig. 5.4. Detailed data on the angular differential cross sections are not available for the high bombarding energy, though experiments at lower energies [94] indicate a pronounced forward peak.

The ^{20}Na ($t_{1/2}$=448±3 ms) beam was produced by using the ^{19}F(^{3}He,2n)^{20}Na reaction. Cross section data for this reaction is not available; in fact, observation of this reaction does not appear to have ever been reported in the literature. However, other (^{3}He,2n) reactions have total cross sections on the order of 100 mb [51]. The ^{20}Na production rates observed in this experiment are consistent with this value.

5.2.3   Separation of ^{8}B and ^{20}Na

The ^{8}B products, fully stripped due to the high energies at which they traversed the gas cell, proceeded down the beam line and through a 22° bending magnet. The bending magnet separated

SPLIT - POLE MAGNETIC SPECTROGRAPH
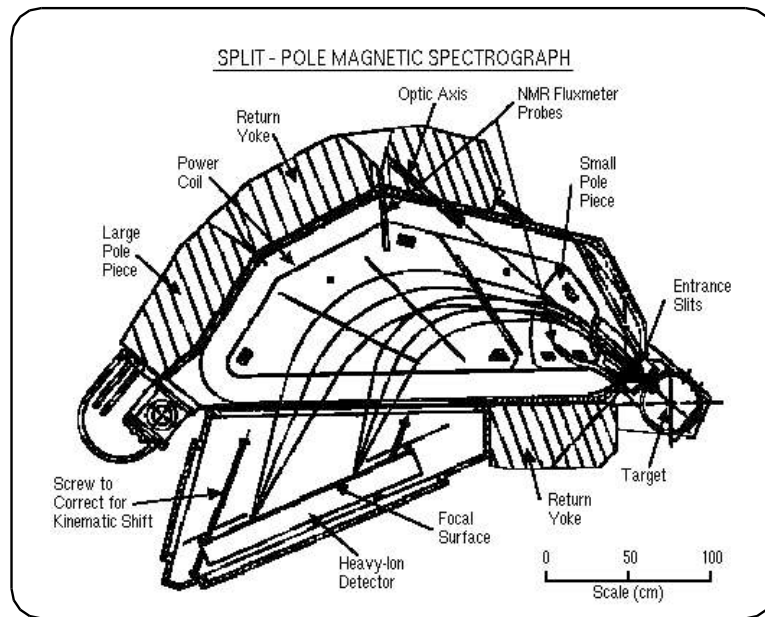
Figure 5.5. A schematic of the Enge split-pole magnetic spectrograph. This figure was taken from the Argonne National Lab website [89].

the ^{8}B beam from the (higher energy) ^{6}Li primary beam, and directed the ^{8}B beam to an Enge Split Pole spectrograph.

A gas-filled detector located in the focal plane of the spectrograph [95], sensitive to mass, nuclear charge, and energy, allowed identification of the ions traversing the spectrograph. Using the gas-filled focal plane detector, the ^{8}B component of the beam was measured to be about one part in 10^3. A portion of the low-energy tail of the primary ^{6}Li beam, as well as α particles, deuterons, and protons with the proper magnetic rigidity to traverse the spectrograph, accounted for most of ions incident on the detector. A ^{6}Li beam incident on ^{3}He cannot produce any β delayed particle emitters other than ^{8}B, which could create a background during the beam-off data acquisition cycles. No products resulting from possible interactions between ^{6}Li and the titanium windows of the gas-cell were observed with the proper rigidity to pass through the spectrograph.

5.2.4 Implantation into the Si Detector

The spectrograph was then adjusted so that ^{8}B ions with energies of 27.3$\pm$0.2 MeV were incident on the planar Si detector with a 150 mm^2 active area (13.8 mm diameter), located adjacent to the gas-filled focal plane detector. The quoted 0.2 MeV uncertainty in the ion energy is more precisely the width of the ion energy distribution. The width results primarily from the size of the Si detector, as different points on the Si detector surface correspond to different radii of curvature in the spectrograph field. An 11 mm diameter Ta collimator masked the edges of the Si detector to ensure that all implanted ^{8}B ions would be located in the active region of the detector.

Ion implantation depth was calculated using the SRIM (the Stopping and Range of Ions in Matter) software package [96]. The package includes several programs capable of modeling the transport and stopping of ions, with energies from 10 eV/amu to 2 GeV/amu, in matter. A description of the physics input and source code is available [97], and a comparison of SRIM stopping predictions to experimental results is actively maintained online [96].

The distribution of ^{8}B ions in the Si detector was modeled using the TRIM (Transport of Ions in Matter) program. The TRIM program is the most comprehensive program in the SRIM package, and gives the path and stopping point of ions on an event-by-event basis. The distribution, as predicted by TRIM, of implantation depths of 2×10^4 ^{8}B ions of energy 27.3 MeV is shown in Fig. 5.6. The distribution is sharply peaked at 42.3 μm, with a full-width at half-maximum of 0.3 μm. There is no significant tail corresponding to shallowly-implanted ions; less than 0.2% of the ions were implanted at a depth less than 40.0 μm.

The sharpness of the implantation depth distribution may easily be understood in a qualitative manner. The stopping of ions is due to two processes: interaction with target electrons and interaction with target nuclei (all arguments in this paragraph are taken from Ref. [97]). For ion energies much higher than 100 keV/amu the target electrons dominate the stopping. In this range, the ions slow due to a very large number of interactions with electrons where the ion loses only a small fraction of its total energy. Statistically, then, ranges of ions undergoing electron stopping will not show a large variance. As the ions slow to less than 100 keV/amu, interactions of ions
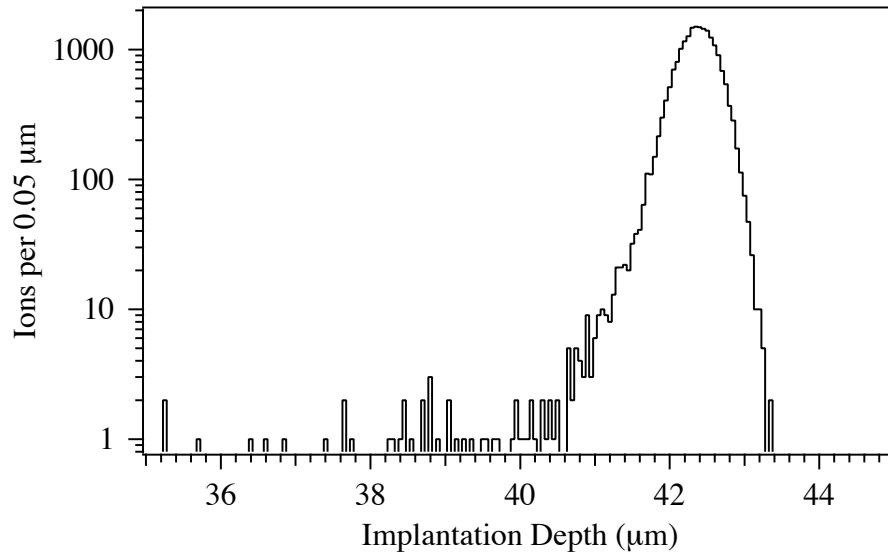
Figure 5.6. The results of a TRIM [96] simulation, showing the distribution of implantation depths of 20,000 ^{8}B ions of energy 27.3 MeV in silicon.

with target nuclei becomes significant. Nuclear collisions, which may involve the ion transferring a large fraction of its energy, may lead to a significant variance in ion range. In this experiment, the implantation energies are significantly high that electronic stopping dominates for most of the ion path, leading to the sharp distribution of Fig. 5.6.

The distribution of ^{8}B implantation depths is affected by the range of ion energies, 27.3±0.2 MeV. The 0.2 MeV uncertainty corresponds to a 0.3 μm uncertainty in implantation depth, according to further TRIM simulations. In this experiment, then, the distribution of ions is broader than that shown for the (monoenergetic) ions of Fig. 5.6. A further uncertainty, corresponding to the accuracy of TRIM, must be assigned. A global comparison of SRIM predictions to experimental stopping power data shows an average deviation of 4.6% [96]. A recent measurement of the slowing of ^{11}B ions, with energies from 3 MeV to 11 MeV, in 780 nm foils of crystal silicon [98] showed agreement with SRIM within 4.6%, hence this value is adopted as the uncertainty inherent in the simulations. It should be noted that the crystal composing the Si detector was cut off-axis from the parent crystal, such that particles normally incident on the detector would not
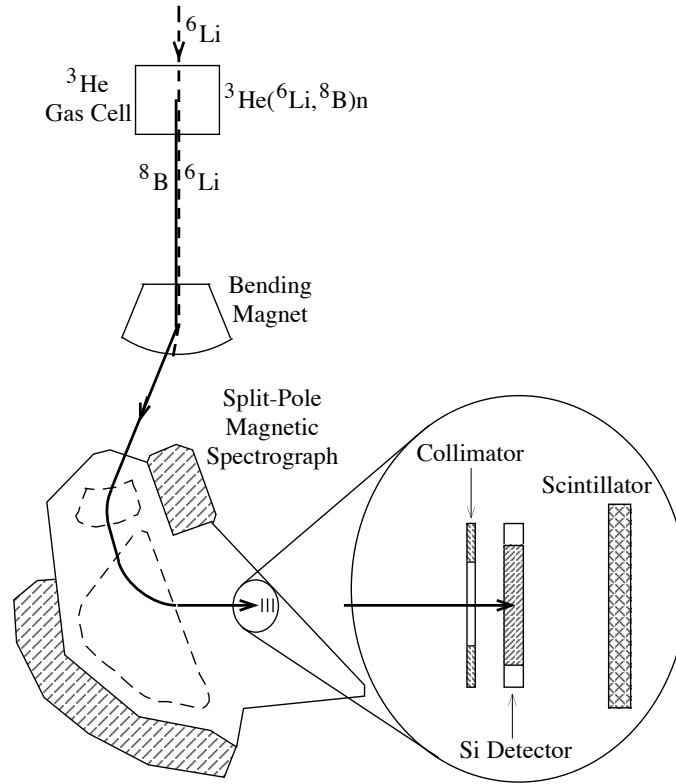
Figure 5.7. The experimental setup used to produce the ^{8}B (^{20}Na) beam, separate it from the primary ^{6}Li (^{19}F) beam, and select ions with energy 27.3 MeV (170 MeV) for implantation into the Si detector (not to scale).

be subject to channeling along symmetry axes [99]. Channeling may increase the implantation depth.

Given the above considerations, the distribution of ^{8}B implantation depths was taken to have a full-width at half-maximum of 0.7 μm, about an average value of 42.3$\pm$2.0 μm. Note that the uncertainty in the average value is due totally to the uncertainty in the SRIM stopping simulation.

The implantation depth distribution of the ^{20}Na ions used for calibration was determined in a similar fashion. The ^{20}Na ions first passed through a mylar degrading foil of thickness 85$\pm$4 μm, located roughly 5 cm up-beam of the detector. The spectrograph was tuned so that ions of energy 170.0$\pm$1.5 MeV were incident on the degrading foil/detector. The distributions of ^{20}Na implantation depths was found to have a full-width at half-maximum of 1.3 μm, about an average
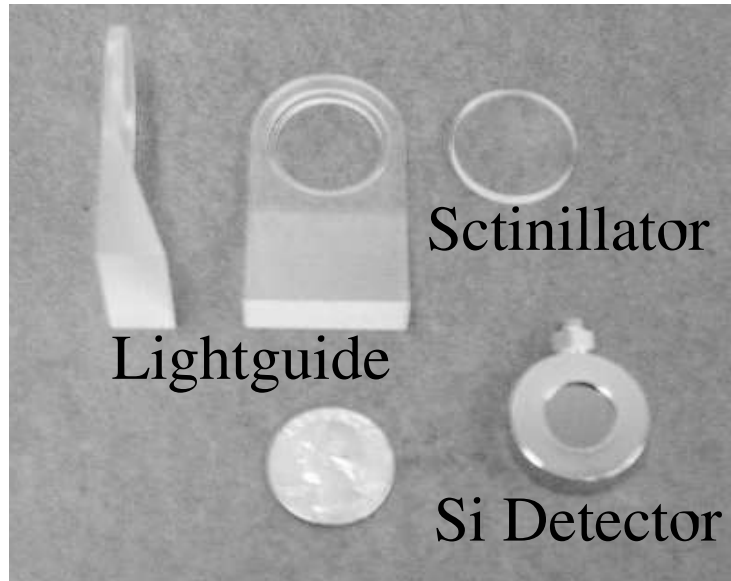
Figure 5.8. A photograph of light guides and scintillator similar to those used in this experiment. The light guide was beveled such that the scintillator would be physically constrained by light guide prior to being cemented. A Si detector, similar to the one used in this experiment, is also shown. The actual detectors used in the experiment were unavailable.

value of 48 ± 6 μm. The increased width and uncertainty associated with the ^{20}Na implantation is primarily due to the presence of the mylar degrading foil.

5.2.5 The Detectors

The Si detector, manufactured by Ortec, is classified as a D-series planar totally depleted silicon surface barrier detector, transmission mounted (model TD-025-150-100, serial number 36-093F). The thickness of the detector was given by the manufacturer as 91 μm, with a maximum thickness variation of 1 μm. The active area was given as 150 mm^2, corresponding to a circular region of diameter 13.8 mm. The detector was biased to 30.0 V.

The β particle detector, located 12 mm behind the Si detector, was a 25 mm diameter $\times$ 2 mm thick plastic scintillator coupled by a light guide to a Hamamatsu R647 photomultiplier tube (PMT). The detector identified a subset of events where the positron from the ^{8}B decay exited the Si detector with a trajectory within 30° to normal. Roughly 16% of the observed
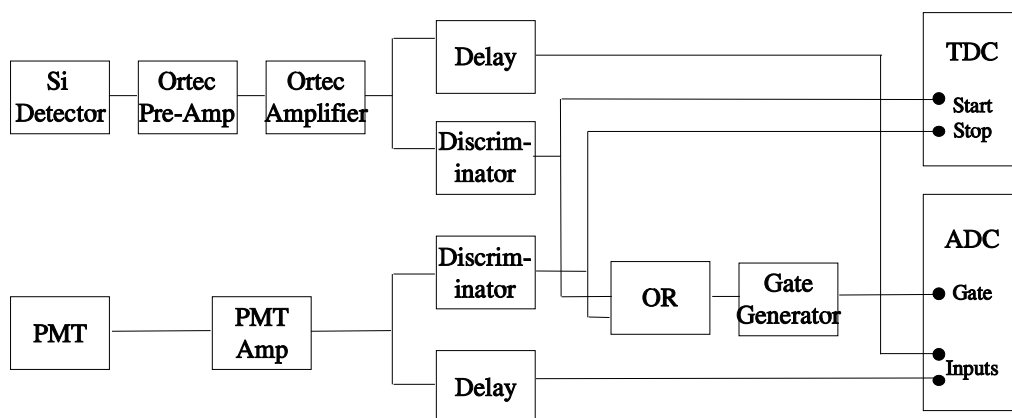
Figure 5.9. A schematic of the data acquisition equipment. Pulses from the detectors are shaped and amplified in the pre-amplifiers and amplifiers, and the pulse sizes recorded in analog-to-digital converters. Any pulse above threshold in either detector produces an electronic gate which causes a trigger for data to be recorded. The relative time between events in the two detectors is also recorded.

events occurred in coincidence with a count in the β detector, consistent with expectations from detector geometry. The Si/scintillator detector system was cooled to -5°C.

A schematic of relative locations of the gas cell, spectrograph, and detectors is shown in Fig. 5.7. A photograph of a Si detector and components of a β detector is shown in Fig. 5.8.

5.2.6   Data Acquisition

The signal from the Si detector was brought out of the spectrograph vacuum and fed into an Ortec 142 pre-amplifier. The signal was further amplified using an Ortec 672 amplifier with a 1.0 μsec shaping time. One output of the amplifier was sent into a Lecroy 623B discriminator used to create an event trigger. Another output of the amplifier was sent into an Ortec 811 analog-to-digital converter (ADC) Camac module which assigned the pulse height from the amplifier to one of 4096 bins.

The signal from the Hamamatsu R647 PMT was amplified using a Lecroy 612 PMT (10×) amplifier. One output of the amplifier was sent into a Lecroy 623B discriminator used to create an event trigger. Another output of the amplifier was fed into an Ortec 811 ADC. An event
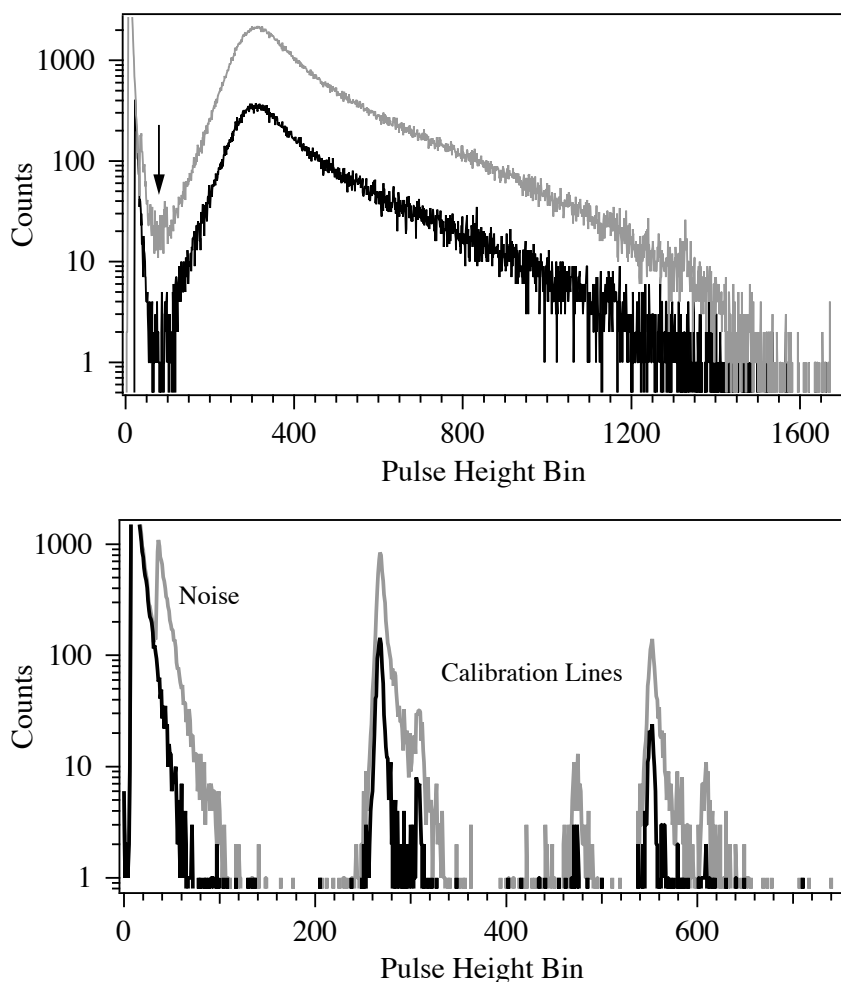
Figure 5.10. Raw data from the ^{8}B (top) and ^{20}Na alpha (bottom) measurements. The dark gray lines indicate alpha particle events which are coincident with an event in the beta detector; light gray lines indicate alpha particle events without regard to the beta detector. The arrow in the top panel points to a contamination peak from protons in the ^{8}B data set. This phenomenon is discussed in Section 5.3.

was defined as a pulse (above discriminator threshold) in either the Si detector or the PMT. A schematic of the data acquisition equipment is shown in Fig. 5.9.

During the ^{8}B run, the primary ^{6}Li beam was cycled (1.5 sec on/1.5 sec off) and data taken only during the beam-off cycles. The average implantation rate was 3 ^{8}B ions/sec, and 4.5×10^5 decays were observed over six days.

The calibration using implanted ^{20}Na was performed immediately before the ^{8}B run. As in

the ^{8}B run, the beam was cycled (1.0 sec on/1.0 sec off). An average implantation rate of 7 ^{20}Na ions/min was achieved, and over one day 1.0×10^4 decays were observed. The raw pulse height spectra from the ^{8}B and ^{20}Na runs are displayed in Fig. 5.10.

5.3 Experimental Uncertainties

The previous section described the experimental technique used to measure the alpha spectrum of ^{8}B. This section deals with the interpreting the experimental data, with an emphasis on the experimental uncertainties. This experiment was performed to measure the α particles *energy* spectrum, as such it is convenient to consider all systematic uncertainties as uncertainties in the energy scale. Naturally, then, an emphasis will be placed on the energy calibration using the ^{20}Na source and the external ^{228}Th source.

This section may be summarized by itemizing the three largest sources of experimental uncertainties in the α spectrum measurement: (1) The uncertainty in the energy scale calibration. (2) The uncertainty in correcting the energy deposited by positrons. The uncertainty in implantation depth of the ^{8}B and ^{20}Na ions may be included in this category. (3) A temporal gain variation observed over the seven days of data collection.

The number of ^{8}B events observed in this experiment (4.5×10^5) is relatively low compared to some past measurements ($\sim 1.6 \times 10^6$ for the deBraeckeleer et al. measurement [48], and $\sim 2.1 \times 10^6$ and $\sim 2.5 \times 10^6$ for the two Wilkinson and Alburger measurements [70]). However, the statistical uncertainties associated with this measurement are very small compared to the systematic ones, as will be discussed in Section 5.4. The present section will deal only with systematic uncertainties in the determination of the energy scale.

5.3.1 Data Cuts

The raw experimental data, shown in Fig. 5.10, was subject to data cuts to remove various backgrounds. The cuts were made using two pieces of information information which were stored
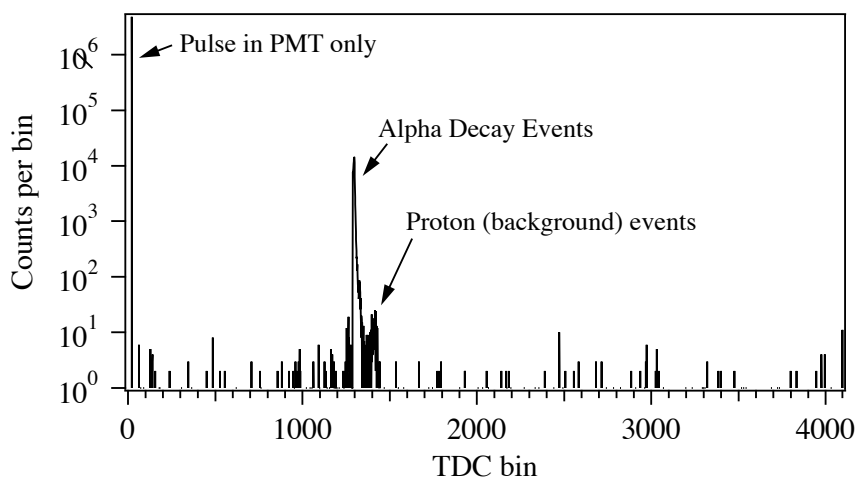
Figure 5.11. The relative time spectrum between events in the β-particle (start signal) and Si (stop signal) detectors, coming from the Time-to-Digital converter shown in Fig. 5.9. The peaks associated with ^{8}B events, proton background events, and events with no β-detector pulse above threshold are indicated. The unlabeled events scattered across the time spectrum are accidental coincidences.

on an event-by-event basis. The first was the relative time between pulses in the Si and β-particle detectors, registered by a TDC (the β-detector provided the start signal and the Si detector the stop signal). The time spectrum is shown in Fig. 5.11. The second was the size of the pulse in the PMT connected to the β-particle detector, registered by an ADC. The readout electronics, including the TDC and ADC, are shown in Fig. 5.9 and have been discussed in Section 5.2.

One type of background resulted because the electrostatic sweeper used to stop the beam was not perfectly efficient, allowing a weak beam during the counting cycles. Naturally, it is impossible to determine these background events from the Si detector pulse height information alone. Any ions in the beam, heavier than protons, with the proper rigidity to traverse the spectrograph and reach the Si detector were stopped [96] in the detector and rejected by the coincidence requirement with the β-particle detector. However, protons with energies near 8.7 MeV, produced in reactions from the primary beams, had the proper rigidity to traverse the spectrograph and hit the Si detector. These 8.7 MeV protons passed through the Si detector [96] and into the β detector, producing a peak near 800 keV in the coincidence data set. This peak is indicated in Fig. 5.10. These proton events were unambiguously rejected from the data set based on timing information,
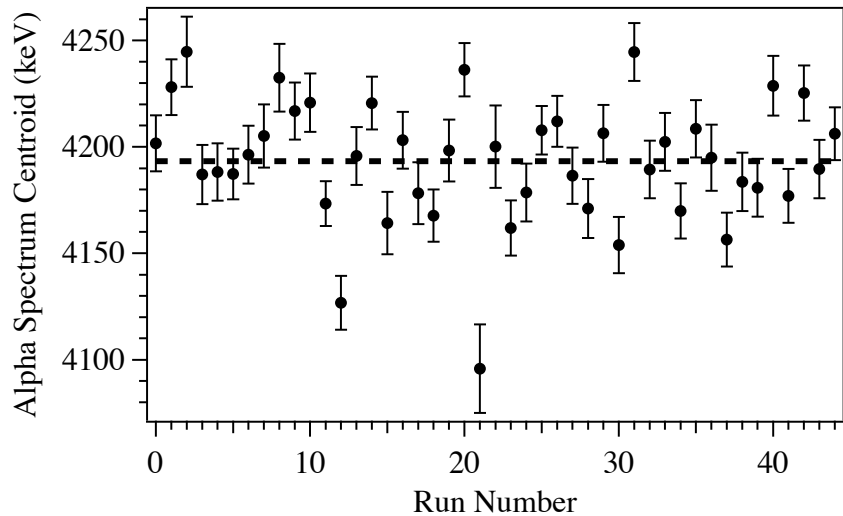
Figure 5.12. The centroid of the ^{8}B alpha spectrum as a function of run. The error bars are from statistics alone. The 45 runs are sequential in time and contain approximately equal amounts of data. The dotted line shows the average value of the centroids. The fluctuations about this value are about twice as large as expected from statistics alone, indicating a systematic variation of the energy scale over time.

as shown in Fig. 5.11, as well as on the large pulses observed in the β-particle detector (which were much larger than the pulses from the fast positrons.)

Random coincidences were removed with cuts on the time spectrum. Additional cuts on the time spectrum eliminated a small amount of background from external β decay activity.

5.3.2 Gain Variation

Possible damage to the Si detector, due to its constant bombardment by ions passing through the spectrograph, was a concern. The flux of ions incident on the detector was monitored by the spectrograph focal plane detector [95]. At the end of the ^{8}B run, the integrated incident flux on the Si detector was an order of magnitude below threshold for detector damage [99], and an increase in the Si detector leakage current characteristic of damage [99] was not observed. Hence, no gain variation resulting from damage was expected.

The gain was monitored with the centroid of the ^{8}B α spectrum and was found to fluctuate

within $\pm0.25\%$, corresponding to ±7 keV at the spectrum peak. The fluctuations are about two times larger than expected from counting statistics. External α particle sources were not reliable for monitoring gain shifts because of the accretion of residual gas onto the cooled Si detector, degrading the α particle energies by 10-20 keV over the course of the seven day run. (The accreted gas was not sufficient to appreciably degrade the ^{8}B and ^{20}Na beams incident on the detector, and had a negligible effect on implantation depth.) A plot of the ^{8}B α spectrum centroid as a function of ^{8}B run (the ^{8}B data was divided into 45 runs, sequential in time and with approximately equal numbers of events) is shown in Fig. 5.12.

A one parameter fit to the centroids gives χ^2=178.7 for 44 degrees of freedom. A two parameter linear fit function gives only a slightly better fit, χ^2=176.9, with the coefficient of the linear term being consistent with zero. Due to the large scatter of the data and the absence of any obvious trend in the gain over time, the gain variation is treated as a random systematic phenomenon. The magnitude of the systematic shift on the energy scale is approximated by increasing the error bars on the centroids by including a systematic uncertainty added in quadrature with the statistical uncertainty. The magnitude of the systematic uncertainty is approximated by requiring a χ^2=44 for 44 degrees of freedom. This procedure leads to the value quoted above, a nonstatistical gain variation of magnitude $\pm0.25\%$. No correction for this was applied to the data, instead a $\pm0.25\%$ uncertainty is included in the energy scale. This is the dominant source of uncertainty in the measurement.

A possible broadening of the alpha spectrum due to this shift will be small, given the relative values of the alpha spectrum width (on order of 1000 keV), and the value of the gain shift (7 keV at the spectrum peak). This effect is included in the analysis of Section 5.4.

5.3.3 Positron Energy Deposition

The positron energy loss in the Si detector was estimated using the EGSnrc simulation [100]. Simulations account for the geometry of the detectors and surrounding materials, positron energy spectra, and the ranges of ion implantation depths discussed previously. Probability distributions
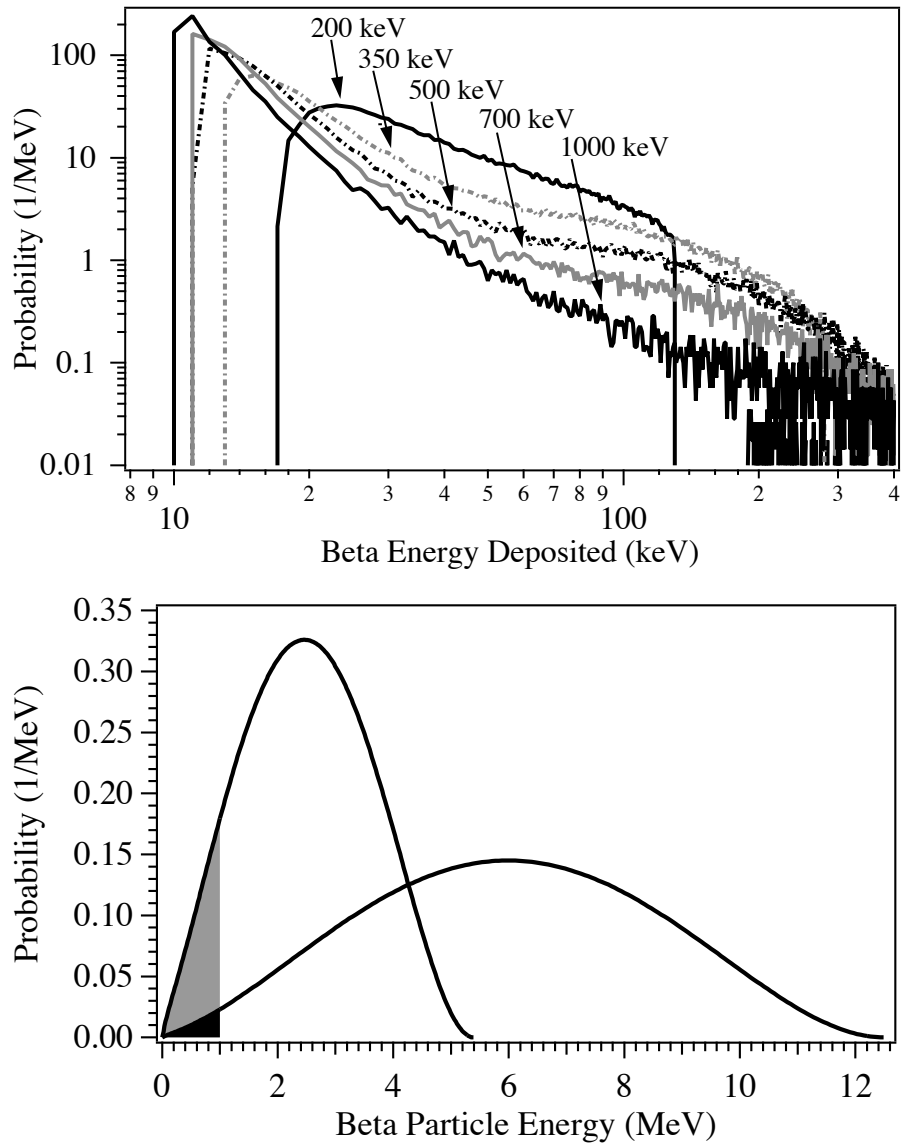
Figure 5.13. (Top panel) Results of EGSnrc [100] simulations giving the probability of a given energy being deposited in the Si detector by beta particles. The results for beta particles of various kinetic energies are indicated. These results are for events where the beta particle also triggers a count in the Si detector. Beta particles with kinetic energies above about 1 MeV have energy deposition curves which are nearly indistinguishable. (Bottom panel) The approximate beta particle energy spectra for ^{20}Na decays to the most probable alpha-emitting state in ^{20}Ne (beta particle endpoint roughly 5.9 MeV), and for the most likely ^{8}B beta decay (endpoint roughly 13 MeV). The spectra are are normalized to integrate to one. The shaded areas indicate the portion of the spectrum lying below 1 MeV kinetic energy, where beta particle energy deposition in the scintillator is increased.

Nucleus	Half life	Decay Description	Alpha Particle Energies in keV (Probability)
$^{228}_{90}$Th	1.91 yrs	α-decay to $^{224}_{88}$Ra	5423 (72.2%), 5340 (27.2%)
$^{224}_{88}$Ra	3.66 days	α-decay to $^{220}_{86}$Rn	5685(94.9%), 5449 (5.1%)
$^{220}_{86}$Th	55.6 sec	α-decay to $^{216}_{84}$Po	6288 (99.9%), 5747 (0.1%)
$^{216}_{84}$Po	0.14 sec	α-decay to $^{212}_{82}$Pb	6778 (100%)
$^{212}_{82}$Pb	10.6 hrs	β^--decay to $^{212}_{83}$Bi	none
$^{212}_{83}$Bi	60.6 min	64.1% β^--decay to $^{212}_{84}$Po	none
		35.9% α-decay to $^{208}_{82}$Pb	6090 (27.1%), 6051(69.9%)
$^{208}_{82}$Pb	stable		none

Table 5.1. The half-lives and decay modes of the nuclear isotopes involved in the decay chain from ^{228}Th to ^{208}Pb. The energies of the prominent emitted α-particles are given, along with the probability of emission. Uncertainties in the energies are on the order of 0.01 keV (much smaller than the precision in the values quoted here). All data in this table comes from a recent compilation of the Table of Radioactive Isotopes [101].

^{20}Ne Energy Level	Branch Ratio	α Energy (keV)	^{16}O Energy (keV)	Pulse Height Defect
1633.67 (2)	79.44%			
7421.9 (1.2)	15.96%	2153.1 (1.0)	538.8 (0.2)	40 keV
7833.4 (1.5)	0.58%	2482.4 (1.2)	621.2 (0.3)	42 keV
9483 (3)	0.24%	3803 (3)	953 (1)	46 keV
10274 (3)	2.88%	4434 (3)	1110 (1)	49 keV
10840 (4)	0.17%	4887 (4)	1223 (1)	51 keV

Table 5.2. Information on the beta-decay of ^{20}Na to the allowed states in ^{20}Ne, and the subsequent alpha disintegrations. All data in this table comes from a recent compilation of the Table of Radioactive Isotopes [101].

for energy loss by positrons were obtained for the subset of data associated with a coincidence count in the β detector, and for the total data set. The results of EGSnrc simulations for β particles producing a coincidence count are shown in Fig. 5.13. As seen in the figure, β particles with low energies deposit a dramatically greater amount of energy than particles which are near minimum ionizing (several MeV). Thus the effect of β particles on the alpha data is significantly greater for the ^{20}Na decays, which have a lower endpoint than the most probably ^{8}B decays, as seen in the Fig. 5.13.

The uncertainty associated with the EGSnrc simulations was estimated by comparing the total ^{8}B data set to the coincidence data set. The effect of the positron correction lowered the
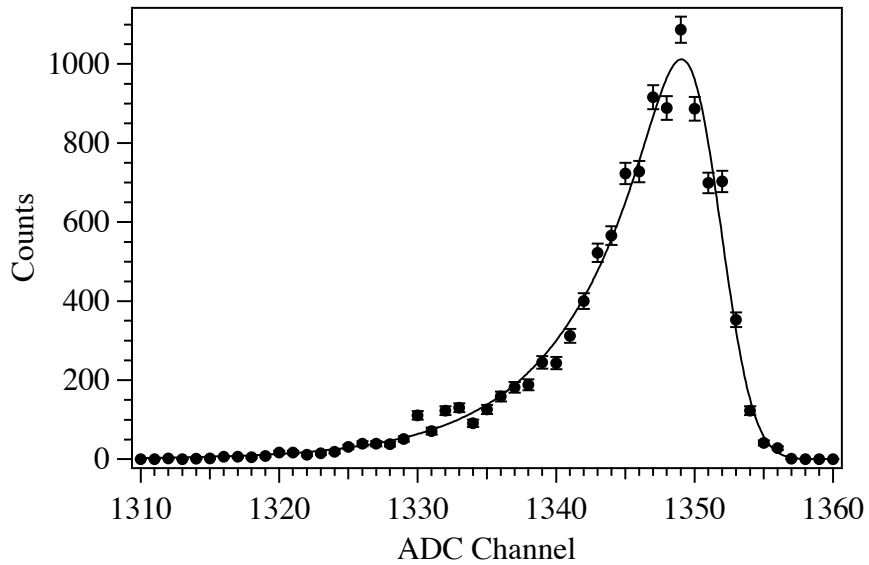
Figure 5.14. A fit to the 6778 keV ^{228}Th alpha line used in the external calibration. The error bars shown are purely statistical.

α-spectrum peak of the total data set by 55 keV, and the peak of the coincidence data set by 24 keV. After the correction, the peaks of the two data sets agreed to within 2 keV. The uncertainty associated with the simulation is thus assigned as ± 2 keV. The use of the total data set to estimate uncertainty in positron energy loss was not compromised by the beam leakage background, since beam particles with the proper rigidity to hit the detector had energies far from the ^{8}B spectrum peak.

Note that uncertainties in ion implantation depth affect the alpha measurement only inasmuch as they affect the energy deposited by positrons. This affect is easily approximated since, on average, minimum ionizing positrons deposit 0.6 keV/μm in Si, so that in the case of ^{8}B (^{20}Na) the uncertainty in implantation depth corresponds to an energy uncertainty of ± 1.2 keV (± 3.6 keV).
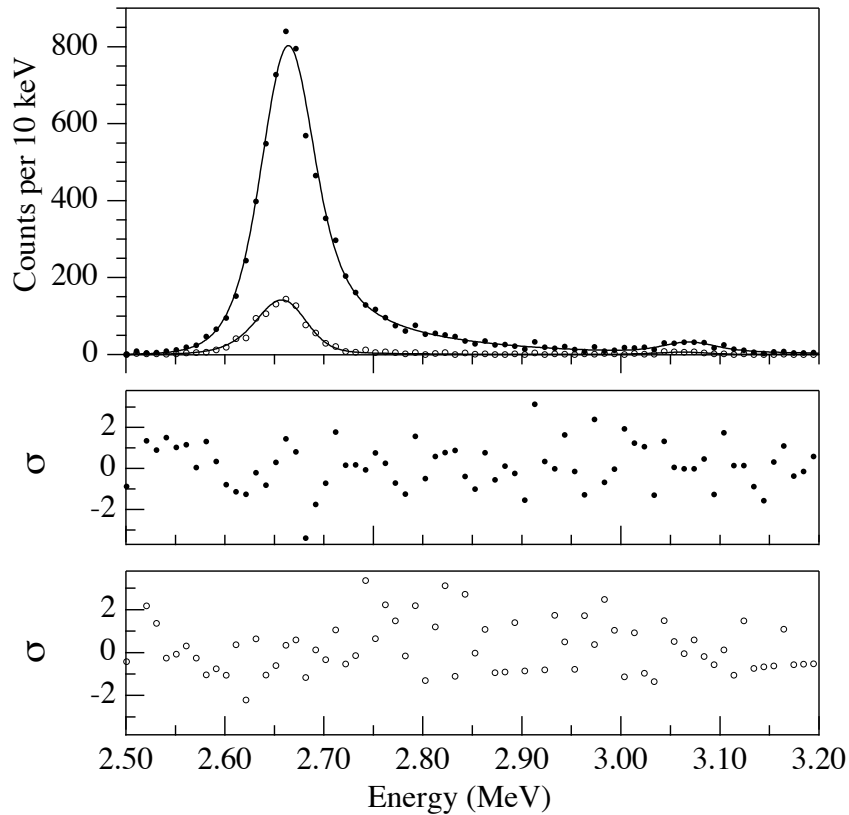
Figure 5.15. (Top panel) Fits to the ^{20}Na calibration lines. The open circles indicate the coincidence data set, while the solid circles indicate the total data set, i.e. no coincidence requirement. The curves show the best fit function, described in the text. (Middle panel) Residuals to the fit of the calibration lines for the total data set. (Bottom panel) Residuals to the fit of the calibration lines for the coincidence data set.

5.3.4   Energy Scale Calibration (using ^{228}Th and ^{20}Na)

Pulser tests were performed before and during the data collection period to investigate the behavior of the ADC. These tests indicated a negligible quadratic component in the relationship between pulse height and ADC bin, so that a linear fit to the calibration lines is sufficient to determine the energy scale. The pulser tests were also used to precisely determine the ADC bin associated with zero pulse size. The zero energy bin was used in the energy calibration.

The external ^{228}Th source emitted α particles at six distinct energies [51] and was used to perform an energy calibration. Details on the decay chain of ^{228}Th are shown in Table 5.1. Data
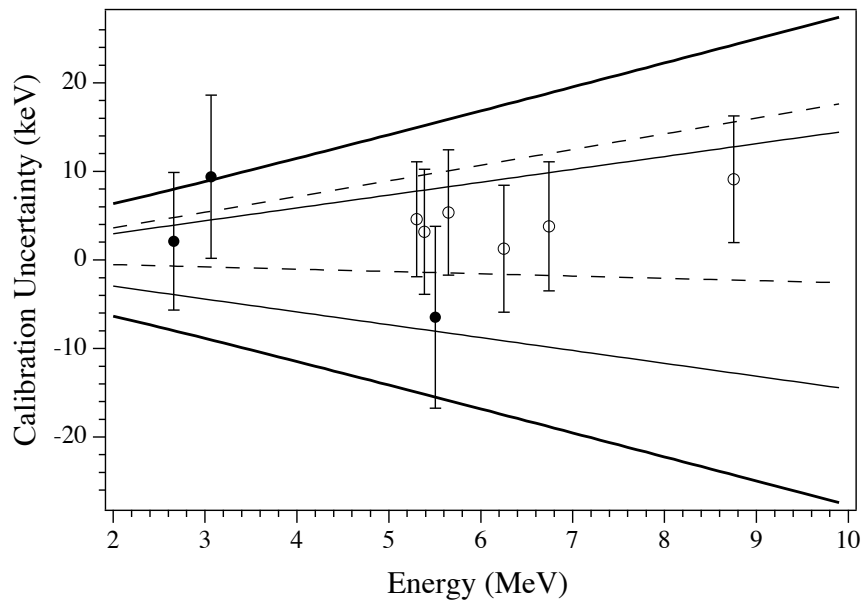
Figure 5.16. Residuals from the calibration process. The solid circles show the residuals for the three ^{20}Na calibration α lines to the best linear fit (energy vs. ADC channel). The open circles correspond to the six external ^{228}Th source α lines, which were not used in the calibration fit. The thin solid curves are the 1σ error bands associated with the ^{20}Na calibrations. The dashed curves are the 1σ error bands of a separate calibration from the ^{228}Th source. The thick solid curves show the total 1σ uncertainty in the energy scale, which is significantly larger than the calibration uncertainty alone due to temporal gain variation.

used for the ^{228}Th calibration was taken shortly after the detector was placed in vacuum and cooled, before an appreciable amount of residual gas condensed on the detector surface. The α particle energies were corrected for energy loss in the source and detector dead layer. The thickness of the dead layer was measured prior to the experiment by exposing the detector to alpha particles from ^{228}Th incident from various angles, giving a thickness of 27±4 μg/cm^2. The magnitude of the corrections for the various lines was 31-38 keV, with a characteristic uncertainty of 4-5 keV. A fit the 6778 keV line is shown in Fig. 5.14.

The energy spectrum from the ^{20}Na decay was used to perform a separate calibration of the energy scale. These data were subject to a correction based on the pulse height defect associated with the recoiling ^{16}O nuclei, which carry one fifth of the energy of the α disintegrations following ^{20}Na decay. The average pulse height defect of the recoil ^{16}O nuclei has been directly measured for ^{16}O nuclei in the energy range of interest [102]. The correction is 40-50 keV for the various

108
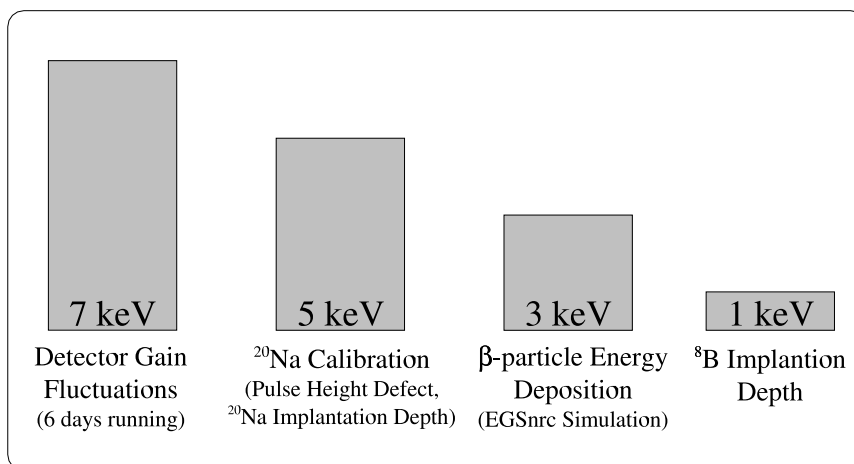
Figure 5.17. A summary of the systematic uncertainties present in the final determination of the alpha spectrum energy scale. The values given apply to the uncertainties at the most probable ^{8}B alpha energy, near 3 MeV.

^{20}Na alpha lines, with an uncertainty of ± 5 keV. The TRIM Monte Carlo simulation [96] was used to model the ionization energy loss of ^{16}O in silicon, and agreed within 2 keV with the average values of ionization loss observed in [102]. We have applied the TRIM results, scaled by 2 keV to agree with the experimental results, to approximate the pulse height spectrum of ^{16}O nuclei in a silicon detector. Further, TRIM was used to approximate the pulse height spectrum of the recoiling ^{16}O nuclei (in contrast to the data of Ref. [102], which provided only the average value of the pulse height).

The three most intense ^{20}Na calibration lines were fit to the pulse height spectrum predicted by TRIM, convoluted with the positron energy loss distributions and a Gaussian component to approximate detector noise. The position and amplitude of the lines were free parameters, as well as the Gaussian width. Results of the fit to two of the lines, resulting from ^{20}Na β^+ decays which led to α energy releases of 2691.9$\pm$1.2 and 3099.0$\pm$2.2 keV, are shown in Fig. 5.15 for both the total and coincidence data sets. The fit to the coincidence data set yielded χ^2/dof=79.3/71, and the total data set χ^2/dof=75.1/71. The log-likelihood minimization function [103] was used in the fits.
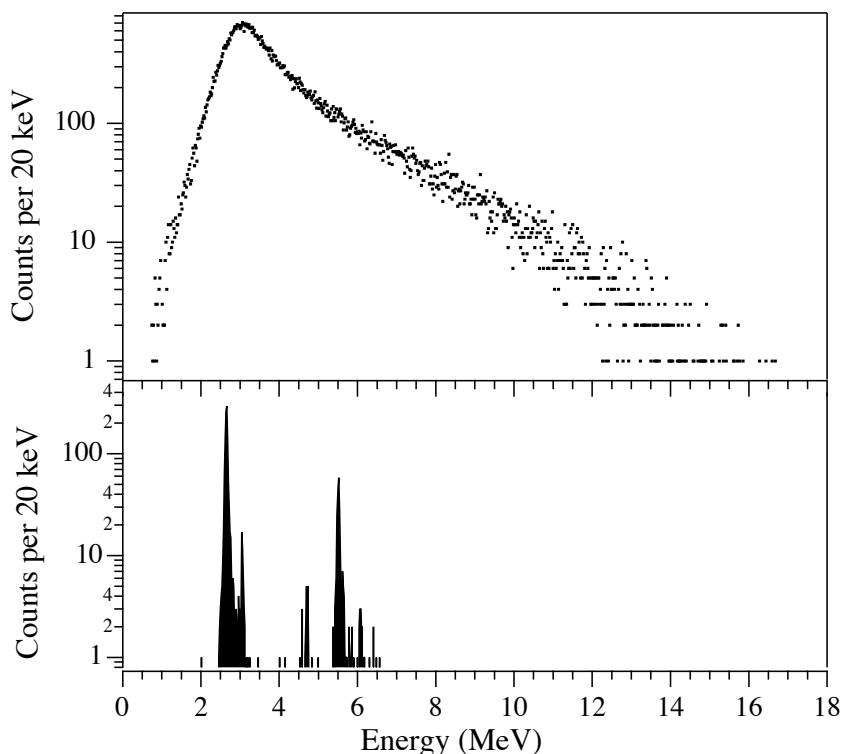
Figure 5.18. The measured ^{8}B β^+ delayed two α energy spectrum shown with the ^{20}Na β^+ delayed α lines used for calibration. The data shown here correspond to events coincident with the beta detector. The three most intense ^{20}Na α lines were used in the calibration. Some α lines of lower intensity are also visible.

A comparison of the ^{20}Na and ^{228}Th calibrations, including residuals to calibration fits, are shown in Fig. 5.16. The two calibrations are completely consistent, as can be seen. However, the ^{228}Th data was not used in the final energy scale determination to prevent uncertainties associated with external alpha sources, a potential source of error in previous alpha measurements discussed in Chapter 4, from affecting this measurement. Fig. 5.16 also shows the total uncertainty in the energy scale, dominated by the temporal gain variation.

5.3.5   Summary of Energy Scale Determination

A summary of the magnitudes of the various uncertainties in the energy scale determination is shown in Fig. 5.17. Plots of both the ^{8}B and ^{20}Na data sets are shown in Fig. 5.18. The data

shown are in coincidence with an event in the β particle detector, have been subject to the data cuts discussed, and are shown with the energy scale determined from the ^{20}Na calibration. Fig. 5.18 thus represents the ultimate result of the alpha spectrum measurement.

5.4 Application of the R-matrix Approach

The previous section led to a ^{8}B alpha spectrum data set with a well-defined energy scale and uncertainties. This section aims to use the R-matrix approach to fit the data with a smooth function and extract the ^{8}B β-decay strength function, as discussed in Chapter 3.

In principle, it is possible to deduce the ^{8}B $β^+$ decay strength function directly from the measured α spectrum without resorting to R-matrix formalism. The R-matrix approach, however, gives a good fit to the observed α spectrum and provides a convenient method for propagating systematic uncertainties in the α spectrum to the neutrino spectrum. Systematic uncertainties in the α spectrum dominate the statistical uncertainties, justifying the representation of the data by a smooth function.

In cases where the ^{8}B decays at rest, as in this experiment, the recoil of the daughter ^{8}Be nucleus will cause the total energy spectrum of the emitted α particles to deviate from the $β^+$ decay strength function given in Eq. 3.14. For a given excitation energy of ^{8}Be, the recoil energy distribution is exactly calculable and takes an average value of 7 keV at the most probable excitation energy near 3.0 MeV.

In addition to accounting for the ^{8}Be recoil, the strength function (Eq. 3.14) must be convoluted with the probability distribution of energies deposited by the positron, discussed in Section 5.3. The detector line shape, approximated as a Gaussian with width 25 keV, determined by fits to the ^{20}Na data sets, was also included but had a negligible impact on the fit due to the large width of the α spectrum.

The α spectrum data was fit using the log-likelihood minimization function [103]. The best fit gave χ^2/dof=3249.7/3376, indicating a satisfactory fit. The best fit parameters are given in
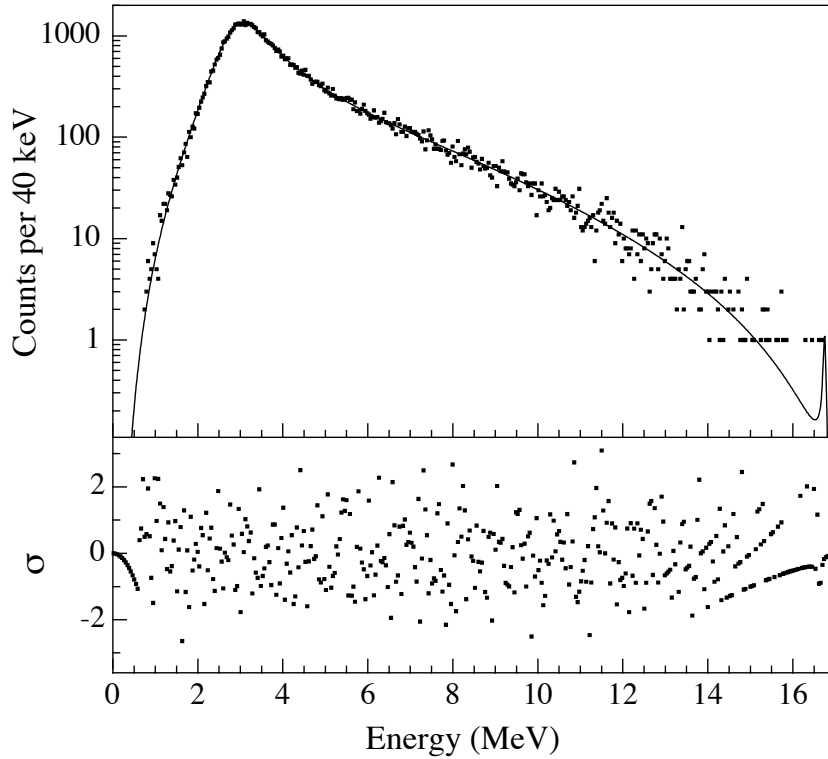
Figure 5.19. (Top panel) R-matrix fit to the observed decay spectrum. (Bottom panel) Residuals to the fit, scaled by the square root of the fit value.

Table 5.3, and the best fit is compared to the data in Fig. 5.19. The strength function is presented in numerical form in Appendix A.

The R-matrix approach was used to propagate the systematic uncertainties in the α spectrum measurement to the neutrino spectrum. As discussed in Sec. 5.3, the 1σ uncertainty in the energy scale is characterized by a multiplicative factor of 1±(0.275%), corresponding to about 8 keV at the spectrum peak, added in quadrature with a constant offset of 3 keV. R-matrix fits were performed to the α spectrum using the ±1σ energy scales, and the resulting ±1σ strength functions were used to produce ±1σ neutrino spectra.

An additional uncertainty was imposed to account for the rapid drop off of the α spectrum at low energies, where statistics are not sufficient to determine the spectrum shape. The penetrability factor, $P(E_x)$, is responsible for the drop off. The best R-matrix fit used $P(E_x)$ calculated for a

Parameter	Value	Parameter	Value
$\mathcal{E}_1$	3.043 MeV	γ_4^2	5.619 MeV
$\mathcal{E}_2$	16.626 MeV[1]	$\mathcal{M}_{GT1}$	-0.1462
$\mathcal{E}_3$	16.922 MeV[1]	$\mathcal{M}_{GTA}$	2.423
$\mathcal{E}_4$	37.0 MeV[1]	$\mathcal{M}_{GT4}$	-0.1320
γ_1^2	1.087 MeV	$\mathcal{M}_{FB}$	$\sqrt{2}$[1]
γ_2^2	10.96 keV[1]	$\mathcal{M}_{GTB}, \mathcal{M}_{F1}, \mathcal{M}_{FA}, \mathcal{M}_{F4}$	0[1]
γ_3^2	7.42 keV[1]		

Table 5.3. Values of R-matrix parameters determined by a fit to the coincidence α spectrum data, using a matching radius of r_c=4.5 fm.

matching radius of 4.5 fm. We approximate the uncertainty at low energies by calculating $P(E_x)$ at 4.0 and 5.0 fm, the $\pm 1\sigma$ matching radii recommended in Ref. [46], and perform fits under these conditions. There is a strong dependence [46] between the energy of the background state, $\mathcal{E}_4$ and matching radius, r_c, so the parameter $\mathcal{E}_4$ was allowed to float for these fits. We note that the variation of matching radius is a significant source of uncertainty only for neutrinos at very high ($E_\nu >$15 MeV) and low ($E_\nu <$0.5 MeV) energies.

5.5   Comparison to Previous Measurements

The strength function determined in this work disagrees with the result of the previous precision measurement of Ortiz *et al*. [49]. For both measurements, the uncertainty in the inferred neutrino spectrum is dominated by systematic effects. Smooth R-matrix fits to the alpha spectra thus provide a convenient way to compare the two results. Fig. 5.20 shows a comparison of the present results and a fit to the data of Ortiz *et al*. [49]. Uncertainties in the Ortiz *et al*. curve are taken directly from Ref. [49].

The strength function of this work has been used to derive a positron spectrum for the β-decay of ^{8}B using techniques described in Chapter 6. The positron spectrum is presented numerically, with uncertainties, in Table A.3. The deduced positron spectrum was compared to the experimental spectrum [104], and a one parameter fit to determine the amplitude gave an agreement of χ^2/dof=33.1/31, where only statistical uncertainties were included in the minimization func-
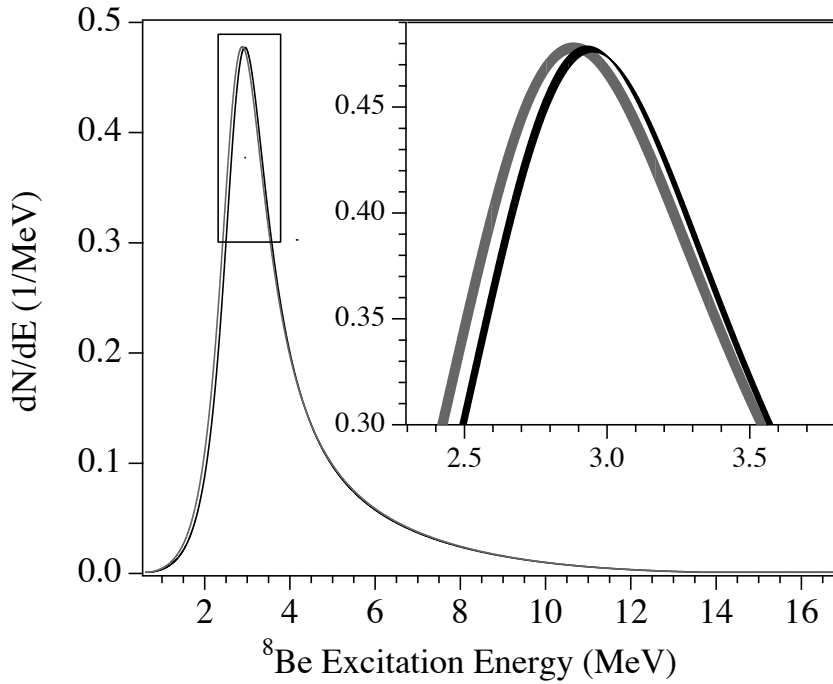
Figure 5.20. The ^{8}B β^+ decay strength function, determined by R-matrix fits to the ^{8}B α spectrum presented in this work (black) and in Ortiz *et al.* [49] (gray). The spectra are scaled to share the same peak height. The insert shows the locations of the spectrum peaks, on which the neutrino spectrum is highly dependent. The width of the lines in the insert indicate the magnitude of the $\pm 1\sigma$ experimental uncertainties. The thin feature in the black curve arises because the dominant uncertainty is a multiplicative factor in the energy scale.

tion. The agreement is shown in Fig. 5.21. The deduced positron spectrum was then allowed to float by an energy offset and marginal improvement (χ^2/dof=32.6/31) was found for an offset of -14±20 keV. In contrast, the positron spectrum deduced by Ortiz et al. [49] must be shifted by an energy offset of -70 ± 20 keV to give agreement (χ^2/dof=31.8/31) with the data [49]. The calibration uncertainty of the positron measurement is reported as 25 keV [72], and is not included in the fits.

After the work described here had been completed, a further measurement of the α spectrum was performed [73]. This new experiment used a technique similar to the Ortiz et al. measurement [49], observing the two α particles in separate detectors. The results [73] are in excellent agreement with the results of this work, as shown in Fig. 5.22.

114
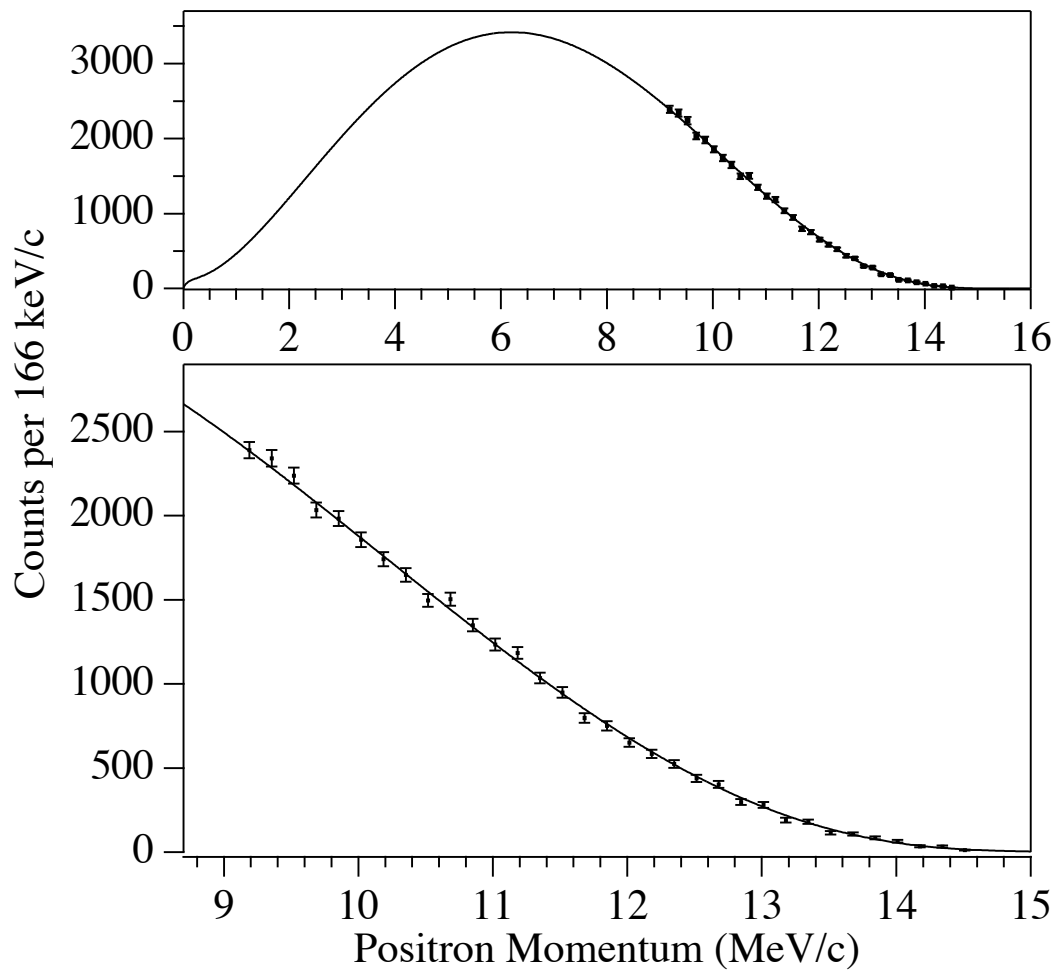
Figure 5.21. (Top panel) Comparison of the direct positron spectrum measurement [104] with the predicted spectrum based on the measured alpha spectrum. The amplitude of the predicted spectrum was floated. (Bottom panel) Same comparison, showing only the momentum range measured in the direct positron spectrum measurement [104].
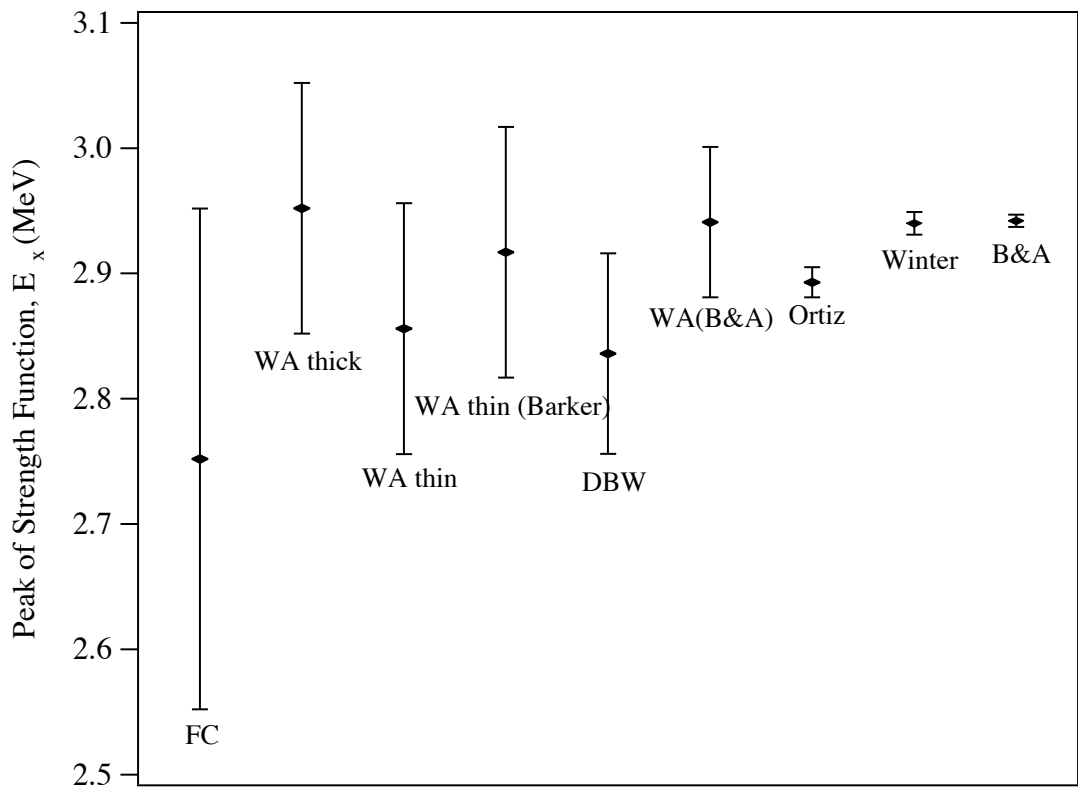
Figure 5.22. The peak of the ^{8}B strength function, as determined by various R-matrix analyses of the four single alpha spectrum data sets, the Ortiz et al. coincidence alpha spectrum data set, the results of this work [50, 87], and the even more recent data set of Bhattacharya et al. [73].

Chapter 6

Recoil Order Corrections to the Neutrino Spectrum

A proper description of ^{8}B β^+ decay includes recoil order effects which cause, for example, the energy spectra and angular correlations of decay particles to deviate from the allowed approximation. Deviations are of order E_0/m_n, where E_0 is the positron endpoint energy and m_n is the nucleon mass. The ^{8}B β^+ decay has a particularly large endpoint energy (most probable $E_0 \approx 13$ MeV) and a small Gamow-Teller strength (log ft = 5.6) for an allowed decay. Recoil order effects in ^{8}B are thus large compared to other nuclear systems.

Measurements of the radiative decay of the ^{8}B isospin analog state in ^{8}Be [54, 55, 56, 48], and of the angular correlation between β and α particles emitted in the decays of ^{8}B and ^{8}Li [57, 58, 59], determine the recoil order matrix elements. These results were first explicitly applied to the neutrino spectrum in [105, 104], where they were found to contribute at the 5% level. A more recent determination of the neutrino spectrum by Bahcall et al. [72] employed the same recoil order treatment as in Ref. [105]. Bahcall et al. provided a conservative estimate of the uncertainty associated with the recoil order correction on the neutrino spectrum by setting the 3σ uncertainty equal to size of the correction itself. A more recent determination of the neutrino spectrum by Ortiz et al. [49], applied recoil order corrections very similar to those in Ref. [105].

The two most recent α spectrum measurements, by Ortiz et al. [49] and the one reported here, involved determinations of the energy scale significantly more precise than the measurements used by Bahcall et al. [72]. Also, a recent precision measurement of radiative decay in ^{8}Be [48] provides additional information on recoil order effects, but has not yet been applied to the ^{8}B neutrino spectrum. In light of these recent experiments, recoil order effects are considered here with careful attention to the assignment of realistic uncertainties.

The Fermi matrix element plays a small role in the β^+ decay of ^{8}B, contributing only to decays proceeding through the highest excitation energies in ^{8}Be, as explicitly discussed in Ref. [46]. These low energy β^+ decays have suppressed recoil order corrections, and produce neutrinos which have no impact on solar neutrino experiments. Consideration of the Fermi matrix element is thus omitted.

A model independent treatment of recoil order effects is given by Holstein [43], whose notation we adopt here. Matrix elements contributing to the β decays of ^{8}B and ^{8}Li are denoted by c (Gamow-Teller), b (weak magnetism), d (induced tensor), f, g (vector second-forbidden), j_2, j_3 (axial second-forbidden), and h (induced pseudoscalar). Since the decays proceed to the broad continuum in ^{8}Be, the matrix elements should be considered as functions of the ^{8}Be excitation energy, E_x. Previous determinations of the ^{8}B neutrino spectrum [105, 104, 72, 49] neglected this energy dependence.

6.1   Beta and Neutrino Energy Spectra

The positron energy spectrum from an allowed decay proceeding between two energetically sharp nuclear states is given by

$$\frac{dN}{dE_\beta} \sim p_\beta E_\beta (E_0 - E_\beta)^2 F(-Z, E_\beta) R(E_\beta, E_0) C(E_\beta, E_0). \qquad (6.1)$$

Here p_β and E_β are the momentum and total energy of the positron, and E_0 is the positron endpoint energy. $F(-Z, E_\beta)$ is the Fermi function, which depends on the charge, Z, of the daughter nucleus and is negative for positron decays. The radiative corrections are contained in $R(E_\beta, E_0)$, which

was discussed in Chapter 2. The recoil order effects are contained in $C(E_\beta,E_0)$, which has the form

$$C(E_\beta,E_0) = 1 - \frac{2E_0}{3Am_n}\left(1 + \frac{d}{c} - \frac{b}{c}\right) + \frac{2E_\beta}{3Am_n}\left(5 - 2\frac{b}{c}\right) - $$

$$- \frac{m_e^2}{3Am_nE_\beta}\left(2 + \frac{d}{c} - 2\frac{b}{c} - \frac{h}{c}\frac{E_0 - E_\beta}{2Am_n}\right), \qquad (6.2)$$

where A=8 is the mass number. In the case of ^{8}B the recoil order matrix elements are dependent on the ^{8}Be excitation energy E_x ($E_x = \Delta - E_0$), where $\Delta = 17.468$ MeV is the total energy released in the ^{8}B β-α decay chain. (This discussion of positron and neutrino energy spectra ignores, for the sake of simplicity, the kinetic recoil of the daughter nucleus. This effect is included in the numerical calculations.) The positron spectrum is calculated by integrating Eq. 6.1 over all excitation energies in ^{8}Be, weighted by the strength function determined in Chapter 5. The neutrino spectrum is obtained by the simple substitution $E_\nu = E_0 - E_\beta$, and the application of different radiative corrections, discussed in Chapter 2.

6.2 Radiative Decay Measurements in ^{8}Be

The weak magnetism matrix element, b, exerts the greatest influence on the neutrino energy spectrum. Its value is best determined under the strong conserved vector current (CVC) hypothesis by measurements of the radiative decays of the ^{8}B isospin analog state in ^{8}Be which, as discussed in Chapter 3, is mixed between the two states of an energy doublet. The radiative decay is shown schematically in Fig. 3.1.

In previous experiments [54, 55, 56, 48], a ^{4}He beam was directed at a ^{4}He gas cell to excite the doublet in ^{8}Be. The ^{4}He(^{4}He,γ)^{8}Be cross section was measured as a function of beam energy and angle of emission of the γ ray. These measurements determine the widths of the isovector M1 and E2 transitions, $\Gamma_{M1}^{T=1}$ and $\delta_1 = \Gamma_{E2}^{T=1}/\Gamma_{M1}^{T=1}$, as well as the widths of the isoscalar transitions, $\varepsilon = \Gamma_{M1}^{T=0}/\Gamma_{M1}^{T=1}$ and $\delta_0 = \Gamma_{E2}^{T=0}/\Gamma_{M1}^{T=1}$. The radiative widths are considered as functions of E_x.

CVC relates the isovector radiative widths in ^{8}Be to the vector recoil matrix elements con-

Observable	Experiment	Value
δ_1	Ref. [54] (1975)	0.045±0.027
	Ref. [56] (1978)	0.14±0.03[1]
	Ref. [48] (1995)	0.01±0.03
δ_0	Ref. [56] (1978)	0.26±0.03[1]
	Ref. [48] (1995)	0.22±0.04
ε	Ref. [56] (1978)	0.00±0.03 [1]
	Ref. [48] (1995)	0.04±0.02
$\Gamma_{M1}^{T=1}$	Ref. [55] (1977)	4.1±0.6 eV[2]
	Ref. [56] (1978)	3.6±0.3 eV[2]
	Ref. [48] (1996)	2.80±0.18 eV

Table 6.1. Experimental determinations of the isovector and isoscalar M1 and E2 transition strengths. All quantities listed are integrated over final state excitation energies in ^{8}Be. [1]These values are based on a reanalysis of the original data, performed in Ref. [48]. The original analysis contained an error in the kinematic treatment of the decay photon. See Ref. [48] for details. [2]The values for M1 width are based on a reanalysis of the original data, performed in Ref. [48], using the values of δ_1 and δ_0 obtained experimentally in Ref. [48].

tributing to ^{8}B β decay, b, f, and g,

$$b(E_x) = Am_n\sqrt{6\Gamma_{M1}^{T=1}(E_x)/(\alpha E_\gamma^3)}, \tag{6.3}$$

$$f(E_x) = \frac{3}{10}\delta_1 b(E_x) \tag{6.4}$$

$$g(E_x) = -\sqrt{\frac{2}{3}}\left(\frac{2Am_n}{E_0}\right)f(E_x). \tag{6.5}$$

The isoscalar radiative widths are not related to β decay form factors by CVC.

A summary of the experimental results is given in Table 6.1. The experimental results for the isoscalar contributions to the decay, ε and δ_0, agree with each other and are of the same order as various shell model predictions compiled in Ref. [48]. The experimental values for δ_1 from two of the experiments [54, 48] are in agreement, but differ from the results in [56] by about 3σ. The present work will use the more recent value of δ_1 [48] which indicates a negligible second-forbidden contribution to the decay, in agreement with shell model predictions. The early experimental determinations of Γ_{M1} [55, 56] disagree with the recent and most precise result [48] by about 2σ. The recent result [48] is in best agreement with β-α angular correlation experiments, as will be discussed later, and is adopted in this work.
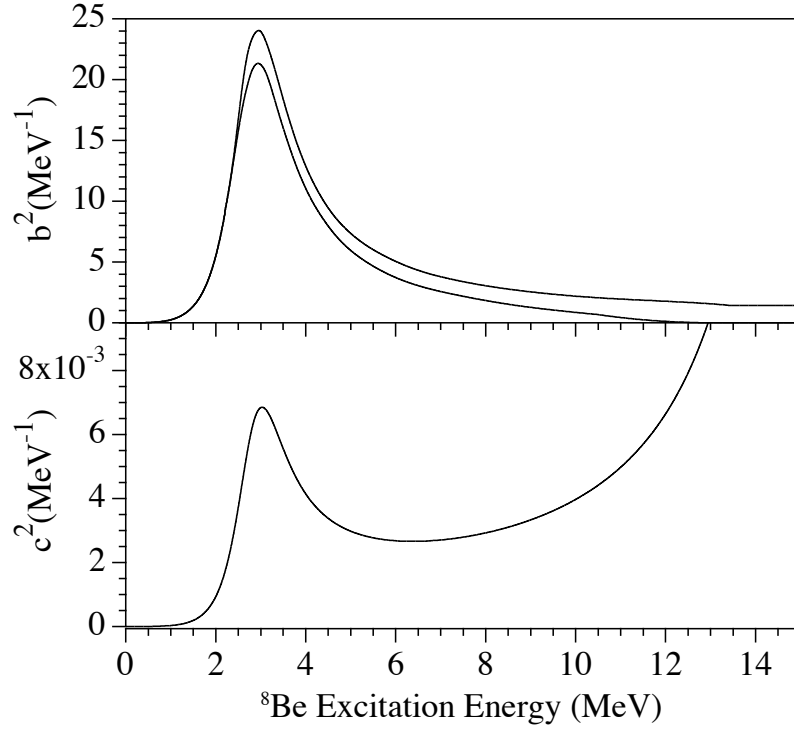
Figure 6.1. The top panel shows the functional dependence of the weak magnetism matrix element, $b(E_x)$, based on the measurement [48] of radiative decay in ^{8}Be. The bands indicate 1σ experimental uncertainties. The bottom panel shows the Gamow-Teller matrix element, $c(E_x)$, based on fits to the α spectrum discussed in Chapter 5. The uncertainties in $c(E_x)$ are comparable to the width of the line and are negligible in the context of recoil order corrections.

The matrix elements $b(E_x)$ and $c(E_x)$ have different functional dependences. This was first observed [54, 56] through a comparison of the shapes of the final state distributions in ^{8}Be following the α and γ decays. The form of $b(E_x)$ was later described [48] using the R-matrix approach, which parametrized $b(E_x)$ as an interfering sum of three different matrix elements, $\mathcal{M}_i$, to the three 2^+ levels in ^{8}B shown in Fig. 3.1,

$$b^2(E_x) = \frac{P(E_x)}{\pi} \left(\frac{\left| \sum_{j=1}^{3} \frac{\mathcal{M}_j \gamma_j}{\mathcal{E}_j - E_x} \right|^2}{\left| 1 - \left(S(E_x) - B + iP(E_x) \right) \sum_{j=1}^{3} \frac{\gamma_j^2}{\mathcal{E}_j - E_x} \right|^2} \right) \tag{6.6}$$

The notations used here are identical to those in Chapter 3. We use the parameters reported in Ref. [48] to determine $b(E_x)$. The form of $c(E_x)$ was given in Eq. 3.17, and determined by fits

121

to the α spectrum. We note that the R-matrix parameters appearing in both Eqs. 3.17 and 6.6 may take different values in the two expressions. The forms of $b(E_x)$ and $c(E_x)$ are shown in Fig. 6.1.

6.3   β-α Angular Correlations

The β-α angular correlations in the mirror decays of ^{8}Li and ^{8}B have been measured several times as a function of β particle energy [57, 58, 59]. Such measurements constrain the weak magnetism matrix element, b, as well as the induced tensor, d. The angular correlations take the form

$$N_\mp(\theta, E_\beta, E_x) = 1 + a_\mp(E_\beta, E_x)\cos\theta + p_\mp(E_\beta, E_x)\cos^2\theta, \tag{6.7}$$

where the -(+) subscript refers to the ^{8}Li(^{8}B) decay, θ is the angle between the β and α particles, and the factor v/c for the β particle has been set equal to 1. The $a_\mp$ coefficients are dominated by kinematic considerations, while the $p_\mp$ coefficients are strongly dependent on recoil order contributions,

$$p_\mp(E_\beta, E_x) = \frac{E_\beta}{2Am_nc} \times \tag{6.8}$$

$$\left([c - (d_I \mp d_{II}) \pm b] \pm \frac{3}{\sqrt{14}}f \pm \sqrt{\frac{3}{28}}g\frac{\Delta - E_x - E_\beta}{Am_n} - \frac{3}{\sqrt{14}}j_2\frac{\Delta - E_x - 2E_\beta}{2Am_n} - \frac{3}{\sqrt{35}}j_3\frac{E_\beta}{Am_n} \right),$$

where Δ is the total energy released in the ^{8}Li(^{8}B) β-α decay chain.

Assuming isospin symmetry, taking the sum and difference of p^- and p^+ produces cancellation between many of the mirror matrix elements of the ^{8}B and ^{8}Li decays. Corrections due to isospin breaking will be considered later. Defining $\delta_\pm = p_- \pm p_+$, dropping the vector matrix elements f and g, integrating over excitation energy E_x gives $\delta_\pm$ as a function of β particle energy,

$$\delta_-(E_\beta)\frac{Am_n}{E_\beta} = \frac{\int b(E_x)c(E_x)(\Delta - E_x - E_\beta)^2 dE_x}{\int c^2(E_x)(\Delta - E_x - E_\beta)^2 dE_x} \tag{6.9}$$

$$\delta_+(E_\beta)\frac{Am_n}{E_\beta} = \tag{6.10}$$

$$\frac{\int \left[c(E_x) - d(E_x) - \frac{3}{\sqrt{14}}j_2(E_x)\frac{\Delta - E_x - 2E_\beta}{2Am_n} - \frac{3}{\sqrt{35}}j_3(E_x)\frac{E_\beta}{Am_n} \right] c(E_x)(\Delta - E_x - E_\beta)^2 dE_x}{\int c^2(E_x)(\Delta - E_x - E_\beta)^2 dE_x}$$
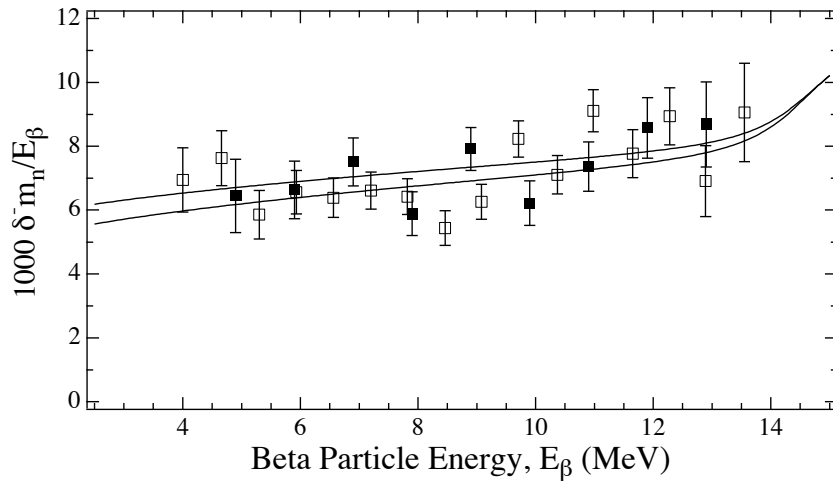
Figure 6.2. The solid squares are experimental data on δ^- from β-α angular correlation measurements from Ref. [58], the open squares are from Ref. [59]. The curves indicate the 1σ error bands from the prediction for δ^+ based on Eq. 6.9, using the weak magnetism, $b(E_x)$, and Gamow-Teller, $c(E_x)$, matrix elements.

where the second class contribution to the induced tensor has been omitted. This is consistent with existing data in the A=8 nuclear system [48], and with theoretical models which predict a second class current to contribute at a level below the current experimental sensitivity.

The matrix elements $b(E_x)$ and $c(E_x)$, determined previously, were applied to Eq. 6.9 to predict the δ^- observed in β-α angular correlation measurements [57, 58, 59]. The predictions are compared to the experimental δ^- data graphically in Fig. 6.2.

The level of agreement between the Eq. 6.9 prediction, based on the radiative decay and alpha spectrum data, and the β-α data sets was quantified by allowing the magnitude of b to float by a multiplicative constant, $b \rightarrow \kappa b$, in Eq. 6.9. The experimental data from the β-α correlation measurements was then used to determine the best fit value of κ. A value of κ different than unity would indicate a disagreement between the radiative width data and the β-α angular correlation data. This approach was previously applied [59, 56, 54, 48] with the motivation of testing CVC and searching for second-class currents. Here, the validity of CVC and the absence of second-class currents are assumed, and the test is performed to gage the level of agreement between the two types of recoil order measurements.

The best fit to the δ^- angular correlation data from Ref. [58] gave κ=1.06(4) with χ^2/dof=7.7/8. The best fit to the data from Ref. [59] gave κ=0.99(3) with χ^2/dof=24.8/15, where the large χ^2 value may be the result of the large point-to-point scatter of the data. The uncertainties in the data from Ref. [59] were expanded by $\sqrt{\chi^2/dof}$ to account for this effect, and both data sets were fit simultaneously, yielding κ=1.014(26) with χ^2/dof=24.6/24. The values of κ obtained, consistent with unity, indicate agreement between the radiative width measurement [48] and the β-α angular correlation measurements [58, 59], and provide confidence in the extracted weak magnetism matrix element.

The experimental $\delta^+(E_\beta)$ data is sensitive to the induced tensor matrix element, d. The effect of d on the neutrino spectrum is much milder than that of b. The energy dependences of $b(E_x)$ and $c(E_x)$ were inferred directly from γ and α spectrum measurements, respectively, but for $d(E_x)$ there is no such experimental signal. The determination of the induced tensor is further complicated by the presence of the axial second-forbidden terms, j_2 and j_3, which appear in the expression for δ^+, Eq. 6.10. Fortunately, the influence of d on the neutrino spectrum is sufficiently small that very conservative estimates of uncertainty may be imposed on d without significantly inflating the total uncertainty of recoil order corrections.

The β particle asymmetry from a polarized source of ^{8}Li or ^{8}B is also sensitive to j_2 and j_3, and would complement β-α correlation measurements to allow a more precise determination of the second-forbidden terms. One measurement of the asymmetry has been performed in ^{8}Li [106], but was systematically skewed by β particle scattering and required a sizable phenomenological correction. We do not include the asymmetry measurement in our analysis, but note that future measurements of this type would be helpful in constraining the values of j_2 and j_3.

Several models [64, 107, 66] have been employed to estimate the magnitude of the axial second-forbidden terms. The models predict contributions to δ^+ from j_2 and j_3 which are comparable to the contributions from the induced tensor, d_I. It has been pointed out [108] that mesonic exchange effects may be significant in A=8 β-decays, especially at the second-forbidden level, and that shell model calculations may break down.
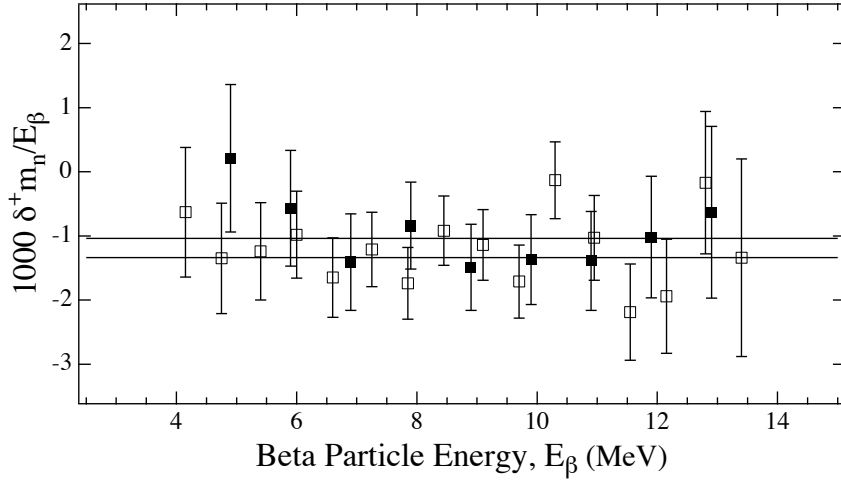
Figure 6.3. The solid squares are experimental data on δ^+ from β-α angular correlation measurements from Ref. [58], the open squares are from Ref. [59]. The curves indicate the 1σ error bands from the prediction for δ^+ based on Eq. 6.9, using the weak magnetism and Gamow-Teller matrix elements determined previously. Second forbidden contributions from j_2 and j_3 were ignored in this fit.

To determine of the best value of d from the δ^+ data, second-forbidden contributions are neglected and d will be assumed to take the same functional form as the Gamow-Teller matrix element, c. The possibility of large second-forbidden contributions to δ^+, with magnitude given by the shell model predictions, will then be considered and their effect on the extracted value of d will be assigned as an uncertainty. The uncertainty associated with the ambiguity in the functional form of d will be estimated by fitting the δ^+ data with the assumption that d takes the same form as the weak magnetism operator, b.

Utilizing the above assumptions, j_2 and j_3 are set equal to zero, d is considered to have the same form as c, $d = \eta c$, and Eq. 6.10 is used to fit the δ^+ data, with η as the only parameter. The best fit to the δ^+ data from Ref. [58] gives $\eta=10.3(2.3)$ with $\chi^2/\mathrm{dof}=2.7/8$. The best fit to the data from Ref. [59] gives $\eta=10.6(1.4)$ with $\chi^2/\mathrm{dof}=12.2/15$. Fitting both data sets simultaneously gives $\eta=10.5(1.2)$ with $\chi^2/\mathrm{dof}=15.0/24$. The results of the fits are compared to the δ^+ data in Fig. 6.3.

The uncertainty associated with the second forbidden terms is estimated by assuming the
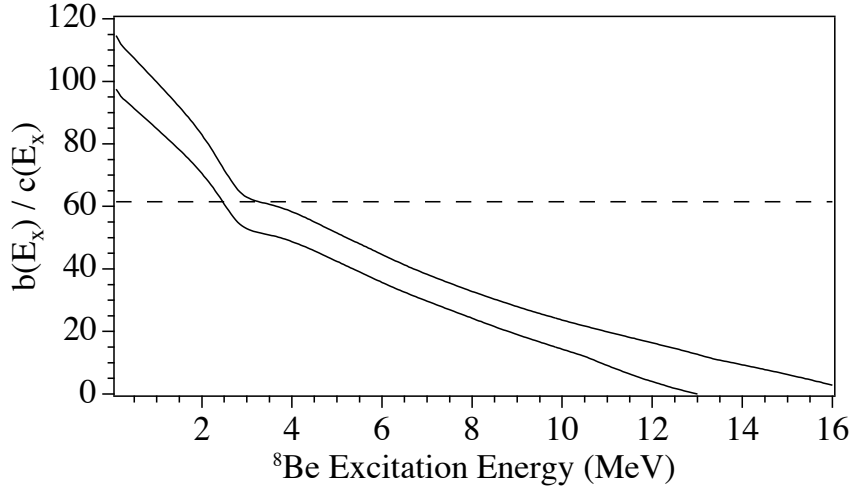
Figure 6.4. The solid curves indicate the 1σ error bands in the ratio between the weak magnetism matrix element, $b(E_x)$, and Gamow-Teller matrix element, $c(E_x)$, used in this work. The dashed line represents the ratio from Ref. [105], used in previous determinations of the neutrino spectrum [105, 104, 72, 49] which neglected the excitation energy dependence of $b(E_x)$ and $c(E_x)$.

values obtained using the model of Ref. [66], $j_2/A^2c \approx -400$ and $j_3/A^2c \approx -750$. We take $d = \eta c$ and the δ^+ data [58, 59] are fit, yielding η=13.8(1.2) with χ^2/dof=16.5/24.

The uncertainty associated with the unknown functional form of the induced tensor is estimated by taking $d = \xi b$. A simultaneous fit to the δ^+ data sets [58, 59], assuming no second forbidden contributions, gives ξ=0.185(20) with χ^2/dof=15.3/24.

6.4   Recoil Order Effects on the Neutrino Spectrum

The values and uncertainties of the weak magnetism, b, and induced tensor, d, matrix elements have been deduced from experimental data. A further uncertainty is applied to these values due to imperfect isospin symmetry and electromagnetic effects. The effect of isospin breaking is estimated by comparing the Gamow-Teller matrix elements of the ^{8}B and ^{8}Li mirror β decays. Previous comparisons of experimental α spectrum following ^{8}B and ^{8}Li decays indicate $c_{Li}/c_B \approx 1.07$ [46, 62]. As seen from Eqs.

6.9 and 6.10, this uncertainty propagates linearly to the extracted values of b and d. We thus
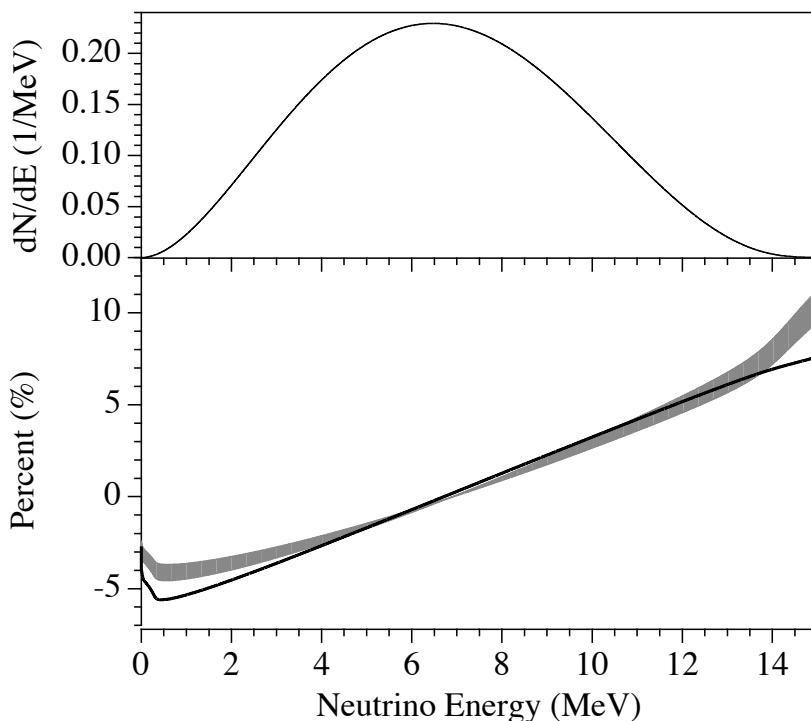
Figure 6.5. (Top panel) The normalized neutrino spectrum deduced in this work. (Bottom panel) The magnitude of the effect of the recoil order matrix elements on the neutrino spectrum. The gray region shows the $\pm 1\sigma$ band of the results obtained in this work. The black line was obtained using the recommended values from Ref. [105], which have been used in previous determinations of the neutrino spectrum.

assign to $b(E_x)$ and $d(E_x)$ a further 7% uncertainty, added in quadrature with previously stated uncertainties. Further electromagnetic effects, such as the difference in decay energies of [8]Li and [8]B and final state electromagnetic interactions, are discussed in Ref. [59] and are proportional to the second forbidden axial terms, j_2 and j_3. These effects contribute up to 4%, when the largest shell model values for j_2 and j_3 are assumed. We thus add, in quadrature, a further 4% uncertainty to $b(E_x)$ and $d(E_x)$.

Fig. 6.4 shows the ratio of $b(E_x)$ to $c(E_x)$ over the range of allowed excitation energies in [8]Be. At high excitation energies, $c(E_x)$ increases rapidly while $b(E_x)$ decreases, as can be seen in Fig. 6.1. In terms of the R-matrix approach, this is explained by comparing the Gamow-Teller strength of the high-lying doublet to the strength of the first excited state at 3.0 MeV, $\mathcal{M}_A/\mathcal{M}_1 =-$

11.8(8). For the weak magnetism transition, the ratio is much smaller, $\mathcal{M}_A/\mathcal{M}_1$=1.4(1.6) [48], and the doublet transition strength plays a smaller role. At excitation energies above 3.0 MeV, the result is a constructive interference of the $\mathcal{M}_A$ and the $\mathcal{M}_1$ terms for $c(E_x)$. Conversely, for excitation energies below 3 MeV, the terms interfere destructively, causing $c(E_x)$ to drop off more rapidly than $b(E_x)$ and increasing the ratio $b(E_x)/c(E_x)$.

The induced pseudoscalar matrix element may be estimated by applying the partially conserved axial current hypothesis, which indicates

$$h(E_x) \approx \frac{4M^2}{m_\pi^2} c(E_x).$$ (6.11)

The induced pseudoscalar appears only in the last term of 6.2 which is suppressed by a factor m_e^2/M^2. The induced pseudoscalar contribution to the β and neutrino energy spectra is thus of order m_e^2/m_π^2, and is ignored.

The magnitude of recoil order effects on the ^{8}B neutrino spectrum determined by the present treatment is compared to the previous treatment [105] in Fig. 6.5.

Chapter 7

The ^{8}B Neutrino and Positron Spectra

The techniques of Chapter 6 were used to create ^{8}B neutrino and positron spectra based on the strength function inferred from the α particle measurement. In addition, radiative effects were accounted for. Radiative corrections to nuclear β decay were first explicitly formulated in [109], and are exact to O(α), where α is the electromagnetic fine structure constant. Further corrections, dependent on the structure of the nucleus, occur at the O($\alpha^2 \ln \frac{m_n}{E_0}$) level. These model dependent corrections are insignificant when compared to the experimental uncertainties in the neutrino spectrum and are not included. Radiative corrections for the case where the neutrino is detected while the positron remains unobserved were calculated explicitly in Ref. [110], and affect the ^{8}B neutrino spectrum at the level of 1%.

The β^+ decay strength function determined in Chapter 5 was applied, using Eq. 6.2, to determine the positron and neutrino spectra of ^{8}B.

The neutrino and positron spectra are presented numerically, with uncertainties, in Appendix A. The neutrino spectrum is compared graphically to the neutrino spectrum of Ortiz et al. [49] in Fig. 7.1. Only uncertainties resulting from the alpha spectrum measurement are indicated in the figure. Fig. 7.1 is slightly different from the analogous figure in our previous publication [50] due to the improved treatment of recoil order effects.
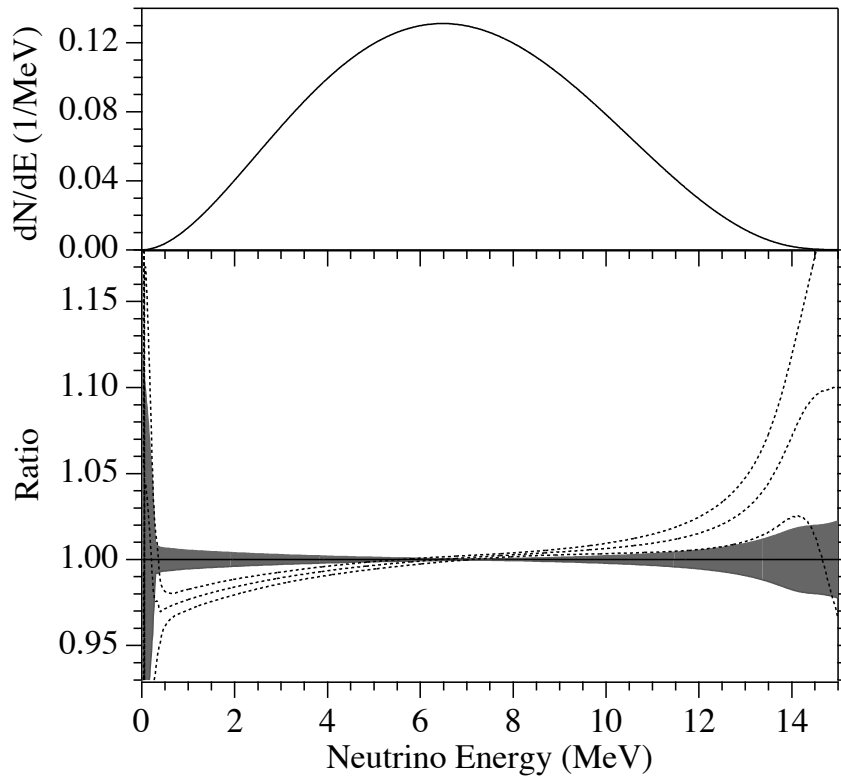
Figure 7.1. (Top panel) The normalized neutrino energy spectrum deduced from this measurement. (Bottom panel) The dashed lines represent the ratio between the neutrino spectrum recommended by Ortiz *et al.*, and the $\pm 1\sigma$ experimental uncertainties, [49] to the spectrum deduced in this work. The black band represents the $\pm 1\sigma$ experimental uncertainties of the spectrum spectrum deduced here. The uncertainties shown are the result of propagating the experimental uncertainties in the measured α spectrum to the neutrino spectrum. Uncertainties from recoil order effects are not included. The Ortiz *et al.* spectrum was smoothed to account for binning effects.

Bibliography

[1] G. Gamow. *Z. Phys.*, 51:204, 1928.

[2] S. Karataglidis, B. K. Jennings, and T. D. Shoppa. *Phys. Rev. C*, 455:900, 1998. is one example of an S-factor extrapolation to low energies, in this case for the ^{7}Be proton-capture reaction.

[3] E. E. Salpeter. *Aust. J. Phys.*, 7:373, 1954.

[4] J. N. Bahcall, X. Chen, and M. Kamionkowski. *Phys. Rev. C*, 57:2756, 1998.

[5] J. N. Bahcall. *Neutrino Astrophysics*. Cambridge University Press, reprint edition, 1990.

[6] J. N. Bahcall, A. Serenelli, and S. Basu. *Astrophys. J.*, 621:L85, 2005.

[7] J. N. Bahcall, M. Kamionkowski, and A. Sirlin. *Phys. Rev. D*, 51:6146, 1995.

[8] Ray Davis, Jr., D. S. Harmer, and K. C. Hoffman. *Phys. Rev. Lett.*, 20:1205, 1968.

[9] S. Nakamura, T. Sato, V. Gudkov, and K. Kubodera. *Phys. Rev. C*, 63:034617, 2001.

[10] M. Butler, J.-W. Chen, and X. Kong. *Phys. Rev. C*, 63:035501, 2001.

[11] S. N. Ahmed The SNO collaboration et al. *Phys. Rev. Lett.*, 90:25201, 2003. gives the most recent results from SNO.

[12] S. Nakamura, T. Satoa, S. Ando, T. S. Park, F. Myhrer, V. Gudkov, and K. Kubodera. *Nucl. Phys. A*, 707:561, 2002.

[13] B. T. Cleveland et al. *Astophys. J.*, 496:505, 1998. gives the final results of the Homestake experiment.

[14] J. Bahcall. *Phys. Rev. Lett.*, 12:300, 1964.

[15] Y. Fukuda Kamiokande collaboration et al. *Phys. Rev. Lett.*, 77:1683, 1996. gives the final results of the Kamiokande solar neutrino experiment.

[16] The Gallex collaboration. *Phys. Lett. B*, 447:158, 1999.

[17] J. N. Abdurashitov et al. *nucl-ex/0509031*, 2005.

[18] S. Fukuda Super-Kamiokande collaboration et al. *Phys. Rev. Lett.*, 86:5651, 2001. gives the most recent results of the Super-Kamiokande solar neutrino experiment.

[19] S. Fukuda Super-Kamiokande collaboration et al. *Phys. Rev. Lett.*, 81:1158, 1998.

[20] The GNO collaboration. *Phys. Lett. B*, 616:174, 2005.

[21] The GNO collaboration. *Phys. Lett. B*, 490:16, 2000.

[22] J. N. Bahcall, N. A. Bahcall, and G. Shaviv. *Phys. Rev. Lett.*, 20:1209, 1968.

[23] J. N. Bahcall, M. C. Gonzalez-Garcia, and C. Peña-Garay. *J. High Energy Phys.*, 7:54, 2002. offers a review of the results, and contains references to the experiments.

[24] K. Eguchi et al. *Phys. Rev. Lett.*, 90:021802, 2003.

[25] M. A. Tortolla M. Maltoni, T. Schwtz and J. W. F. Valle. *Phys. Rev. D*, 68:113010, 2003. offers a review of the interpretation of solar neutrino data, including the recent SNO data from [11], as well as data from the KamLAND experiment [15].

[26] D. W. Liu Super-Kamiokande collaboration et al. *Phys. Rev. Lett.*, 93:021802, 2004.

[27] A. Goobar, S. Hannestad, E. Morts. Mrtsell, and H. Tu. *arXiv:astro-ph/0602155*, 2006.

[28] C. Quiqq. *Gauge Theories of the Strong, Weak, and Electromagnetic Interactions.* Addison-Wesley, 2nd edition, 1997.

[29] M. E. Peskin and D. V. Scroeder. *An Introduction to Quantum Field Theory.* Perseus Books, 1995.

[30] C. N. Yang and R. L. Mills. *Phys. Rev.*, 96:191, 1954.

[31] J. N. Bahcall and S. C. Frautschi. *Phys. Lett.*, B29:263, 1969.

[32] L. Wolfenstein. *Phys. Rev. D*, 17:2369, 1978.

[33] L. Wolfenstein. *Phys. Rev. D*, 20:2634, 1979.

[34] S. P. Mikheyev and A. Y. Smirnov. *Sov. J. Nucl. Phys.*, 42:913, 1986.

[35] S. P. Mikheyev and A. Y. Smirnov. *JETP*, 64:4, 1986.

[36] S. P. Mikheyev and A. Y. Smirnov. *Nuovo Cimento*, 9C:17, 1986.

[37] T. D. Lee and C. N. Yang. *Phys. Rev.*, 104:254, 1956.

[38] C. S. Wu, E. Ambler, R. W. Hayward, D. D. Hoppes, and R. P. Hudson. *Phys. Rev.*, 105:1413, 1957.

[39] W. P. Alford and D. R¿ Hamilton. *Phys. Rev.*, 95:1351, 1954.

[40] B. M. Rustad and S. L. Ruby. *Phys. Rev.*, 89:880, 1953.

[41] N. E. Booth et al. *Nucl. Phys.*, 11:341, 1959.

[42] J.H. Christenson, J.W. Cronin, V.L. Fitch, and R. Turlay. *Phys. Rev. Lett.*, 13:138, 1964.

[43] B. R. Holstein. *Rev. Mod. Phys.*, 46:789, 1974.

[44] R. P. Feynman and M. Gell-Mann. *Phys. Rev.*, 109:193, 1958.

[45] R. E. Warner, A. Okihana, M. Fujiwara, N. Matsuoka, S. Kakigi, S. Hayashi, K. Fukunaga, J. Kasagi, and M. Tosaki. *Phys. Rev. C*, 45:2328, 1992.

[46] E. K. Warburton. *Phys. Rev. C*, 33:303, 1986. contains an R-matrix analysis of available data on the ^{8}B and ^{8}Li β-delayed alpha spectra, as well as d-wave alpha-alpha scattering up to 34 MeV.

[47] B. J. Farmer and C. M. Class. *Nucl. Phys.*, 15:626, 1960.

[48] L. De Braeckeleer et al. *Phys. Rev. C*, 51:2778, 1995.

[49] C. E. Ortiz, A. Garcia, R. A. Waltz, M. Bhattacharya, and A. K. Komives. *Phys. Rev. Lett.*, 85:2909, 2000. contains a description of the experiment and presents the results in graphical format. Details concerning the data analysis which are not explicitly discussed in the Letter are available in C. Ortiz, Ph.D. thesis, Notre Dame (2000).

[50] W. T. Winter, S. J. Freedman, K. E. Rehm, I. Ahmad, J. P. Greene, A. Heinz, D. Henderson, R. V. F. Janssens, C. L. Jiang, E. F. Moore, G. Mukherjee, R. C. Pardo, T. Pennington, G. Savard, J. P. Schiffer, D. Seweryniak, G. Zinkann, and M. Paul. *Phys. Rev. Lett.*, 91:252501, 2003.

[51] F. Ajzenberg-Selove. *Nucl. Phys.*, A490:1, 1988.

[52] F. K. Goward and J. J. Wilkins. *Proc. Roy. Soc. London*, 228:376, 1955.

[53] C. P. Browne and J. R. Erskine. *Phys. Rev.*, 143:683, 1966.

[54] A. M. Nathan, G. T. Garvey, P. Paul, and A. K. Warburton. *Phys. Rev. Lett.*, 35:1137, 1975.

[55] P. Paul, M. Suffert, and Ph. Gorodetzky. *Phys. Lett.*, 71B:71, 1977.

[56] T. J. Bowles and G. T. Garvey. *Phys. Rev. C*, 18:1447, 1978.

[57] R. E. Tribble and G. T. Garvey. *Phys. Rev. Lett.*, 32:314, 1974.

[58] R. E. Tribble and G. T. Garvey. *Phys. Rev. C*, 12:967, 1975.

[59] R. D. McKeown, G. T. Garvey, and C. A. Gagliardi. *Phys. Rev. C*, 22:738, 1980.

[60] F. C. Barker. *Aust. Journ. Phys.*, 22:293, 1969.

[61] F. C. Barker. *Aust. Jour. Phys.*, 42:25, 1989.

[62] M. Bhattacharya and E. G. Adelberger. *Phys. Rev. C*, 65:055502, 2002.

[63] A. M. Lane and R. G. Thomas. *Rev. Mod. Phys.*, 30:257, 1958. offers a comprehensive review of the R-matrix theory.

[64] F. C. Barker. *Nucl. Phys.*, 83:418, 1966.

[65] F. Hinterberger et al. *Nucl. Phys.*, A299:397, 1978.

[66] S. Cohen and D. Kurath. *Nucl. Phys.*, 73:1, 1965.

[67] D. H. Wilkinson and B. E. F. Macefield. *Nucl. Phys.*, A232:58, 1974.

[68] J. A. Wheeler. *Phys. Rev.*, 59:27, 1941. presents an example of an (unsatisfactory) early attempt to theoretically describe the shape of the ^{8}Be resonance.

[69] G. J. Clark, P. B. Treacy, and S. N. Tucker. *Aust. J. Phys*, 22:663, 1969.

[70] D. H. Wilkinson and D. E. Alburger. *Phys. Rev. Lett.*, 26:1127, 1971.

[71] L. De Braeckeleer and D. Wright. unpublished data.

[72] J. N. Bahcall, E. Lisi, D. E. Alburger, L. De Braeckeleer, S. J. Freedman, and J. Napolitano. *Phys. Rev. C*, 54:411, 1996.

[73] M. Bhattacharya, E. G. Adelberger, and H. E. Swanson. *Phys. Rev. C*, 73:055802, 2006.

[74] P. Riehs. *Acta Phys. Austriaca*, 27:205, 1969.

[75] O. Nachtmann. *Z. Phys.*, 215:505, 1968.

[76] R. Dobrozemsky, E. Kerschbaum, G. Moraw, H. Paul, C. Stratowa, and P. Weinzierl. *Phys. Rev. D*, 11:510, 1975. describes an early measurement of the recoil proton spectrum following neutron decay. This experiment was chosen since it was performed in parallel with some theoretical work of the author of Ref. [75].

[77] H. Eichner, K. H. Lauterjung, H. Meinhardt, B. Schimmer, and U. Schimdt-Rohr. *Z. Naturforsch*, 21A:908, 1966.

[78] D. Schardt and K. Riisager. *Z. Phys. A*, 345:265, 1993.

[79] D. E. Alburger, P. F. Donovan, and D. H. Wilkinson. *Phys. Rev.*, 132:334, 1963.

[80] F. C. Gilbert. *Phys. Rev.*, 93:499, 1953.

[81] W. H. Barkas. *Phys. Rev.*, 89:1019, 1953.

[82] F. Ajzenberg and T. Lauritsen. *Rev. Mod. Phys.*, 24:336, 1952.

[83] C. M. Class and S. S. Hanna. *Phys. Rev.*, 89:877, 1953.

[84] D. St P. Bunbury. *Phys. Rev.*, 90:1121, 1953.

[85] T. A. Griffy and L. C. Beidenharn. *Nucl. Phys.*, 15:636, 1960.

[86] D. Powers and W. Whaling. *Phys. Rev.*, 126:61, 1962.

[87] W. T. Winter, S. J. Freedman, K. E. Rehm, and J. P. Schiffer. *Phys. Rev. C*, 73:025503, 2006.

[88] F. Ajzenberg-Selove. *Nucl. Phys.*, A475:1, 1987.

[89] Argonne National Laboratory website. http://www.anl.gov.

[90] maintained by Brookhaven National Laboratory National Nuclear Data Center website. http://www.nndc.bnl.gov.

[91] R. E. Marrs, D. Bodansky, and E. G. Adelberger. *Nucl. Phys.*, 8:427, 1973.

[92] C. R. McClenahan and R. E. Segel. *Phys. Rev. C*, 11:370, 1975.

[93] B. Harss et al. *Rev. Sc. Instrum.*, 71:380, 2000.

[94] W. R. McMurray P. Van der Merwe and I. J. Van Heerden. *Nucl. Phys.*, A103:474, 1967.

[95] K. E. Rehm and F. L. H. Wolfs. *Nucl. Inst. Meth. A*, 273:262, 1988.

[96] J. F. Ziegler. http://www.srim.org.

[97] J. F. Ziegler, J. P. Biersack, and U. Littmark. *The Stopping and Range of Ions in Solids*. Pergamon Press, 1st edition, 1985.

[98] W. Jiang, R. Grotzschel, W. Pilz, B. Schmidt, and W. Moller. *Phys. Rev. B*, 59:226, 1998.

[99] Ortec document. http://www.ortec-online.com/detectors/chargedparticle/introduction/radi%ation.htm.

[100] EGS software. http://www.irs.inms.nrc.ca/inms/irs/EGSnrc/EGSnrc.html.

[101] R. B. Firestone. http://isotopes.lbl.gov/education/isotopes.htm.

[102] W. N. Lennard et al. *Nucl. Inst. Meth. A*, 248:454, 1986.

[103] S. Baker and R. D. Cousins. *Nucl. Inst. Meth.*, 221:437, 1984.

[104] J. Napolitano, S. J. Freedman, and J. Camp. *Phys. Rev. C*, 36:298, 1987.

[105] J. N. Bahcall and B. R. Holstein. *Phys. Rev. C*, 33:2121, 1986.

[106] J. R. Hall, D. L. Clark, S. J. Freedman, and S. S. Hanna. *Nucl. Phys.*, A483:1, 1988.

[107] A. N. Boyarkina. *Izv. Akad. Nauk USSR (ser. fiz.)*, 28:327, 1964.

[108] K. Kubodera, J. Delorme, and M. Rho. *Nucl. Phys.*, B66:253, 1973.

[109] A. Sirlin. *Phys. Rev. Lett.*, 164:1767, 1967.

[110] I. S. Batkin and M. K. Sundaresan. *Phys. Rev. D*, 52:5362, 1995.

[111] W. T. Winter, S. J. Freedman, K. E. Rehm, and J. P. Schiffer. http://www.aip.org/pubservs/epaps.html. See EPAPS Document No. E-PRVCAN-73-925601, for numerical tables of the B8 strength function, and the beta and neutrino spectra. This file originally appeared as material supplementary to a publication by the same authors [87].

Appendix A

Numerical Tables of Results

This appendix contains the primary results of this work in numerical form. These results are actively maintained online [111] in computer-readable format, and originally appeared as supplementary material to a previous publication by the author [87]. The following three tables give the ^{8}B β-decay strength function, the ^{8}B neutrino spectrum, and the ^{8}B positron spectrum deduced in this work.

Table A.1: The ^{8}B β^+ decay strength function, as determined by fitting the experimental α spectrum to Eq. 3.14. The strength function is normalized to 1000 when integrated with respect to MeV. Note that the energy spacing of data points varies to allow a more detailed description of the strength function near the peak. Here P(E$_x$)=dN/dE$_x$ is the probability that a given excitation energy range in ^{8}Be is populated by ^{8}B β decay.

E_x	$P(E_x)$	$\Delta P(E_x)$	E_x	$P(E_x)$	$\Delta P(E_x)$	E_x	$P(E_x)$	$\Delta P(E_x)$
0.00	0.00	0.00	2.92	474.95	1.56	5.40	77.98	0.42
0.10	0.00	0.00	2.94	475.32	1.23	5.50	73.98	0.39
0.20	0.00	0.00	2.96	474.90	0.92	5.60	70.27	0.37
0.30	0.02	0.00	2.98	473.71	0.65	5.70	66.81	0.35
0.40	0.08	0.00	3.00	471.81	0.46	5.80	63.59	0.33
0.50	0.21	0.01	3.02	469.23	0.44	5.90	60.57	0.32
0.60	0.44	0.01	3.04	466.03	0.58	6.00	57.74	0.30
0.70	0.83	0.02	3.06	462.24	0.78	6.20	52.59	0.28
0.80	1.44	0.03	3.08	457.94	0.99	6.40	48.01	0.26
0.90	2.35	0.05	3.10	453.16	1.20	6.60	43.91	0.24
1.00	3.64	0.07	3.12	447.95	1.39	6.80	40.22	0.22
1.10	5.43	0.10	3.14	442.38	1.56	7.00	36.89	0.21
1.20	7.88	0.14	3.16	436.48	1.72	7.20	33.86	0.20
1.30	11.16	0.20	3.18	430.31	1.86	7.40	31.09	0.19
							Continued on next page	

136

E_x	$P(E_x)$	$\Delta P(E_x)$	E_x	$P(E_x)$	$\Delta P(E_x)$	E_x	$P(E_x)$	$\Delta P(E_x)$
1.40	15.51	0.28	3.20	423.91	1.98	7.60	28.57	0.18
1.50	21.24	0.39	3.22	417.32	2.09	7.80	26.25	0.17
1.55	24.75	0.45	3.24	410.58	2.18	8.00	24.11	0.16
1.60	28.76	0.53	3.26	403.72	2.25	8.20	22.15	0.15
1.65	33.35	0.62	3.28	396.78	2.32	8.40	20.33	0.15
1.70	38.58	0.72	3.30	389.78	2.37	8.60	18.65	0.14
1.75	44.56	0.84	3.32	382.76	2.41	8.80	17.10	0.14
1.80	51.38	0.97	3.34	375.74	2.43	9.00	15.67	0.13
1.85	59.15	1.13	3.36	368.74	2.45	9.20	14.33	0.12
1.90	67.99	1.31	3.38	361.78	2.46	9.40	13.10	0.12
1.95	78.05	1.52	3.40	354.87	2.46	9.60	11.96	0.11
2.00	89.46	1.76	3.42	348.03	2.46	9.80	10.90	0.11
2.05	102.40	2.02	3.44	341.27	2.45	10.00	9.91	0.10
2.10	117.00	2.32	3.46	334.61	2.43	10.20	9.01	0.10
2.15	133.44	2.66	3.48	328.05	2.41	10.40	8.17	0.09
2.20	151.84	3.02	3.50	321.60	2.39	10.60	7.39	0.09
2.25	172.32	3.42	3.52	315.26	2.36	10.80	6.67	0.08
2.30	194.92	3.83	3.54	309.04	2.33	11.00	6.01	0.08
2.32	204.54	3.99	3.56	302.94	2.30	11.20	5.40	0.08
2.34	214.50	4.16	3.58	296.97	2.26	11.40	4.84	0.07
2.36	224.77	4.32	3.60	291.13	2.23	11.60	4.33	0.07
2.38	235.34	4.48	3.62	285.42	2.19	11.80	3.86	0.06
2.40	246.20	4.63	3.64	279.83	2.15	12.00	3.43	0.06
2.42	257.32	4.78	3.66	274.38	2.11	12.20	3.03	0.05
2.44	268.68	4.92	3.68	269.06	2.07	12.40	2.67	0.05
2.46	280.23	5.04	3.70	263.86	2.03	12.60	2.35	0.05
2.48	291.95	5.15	3.72	258.79	1.99	12.80	2.05	0.04
2.50	303.78	5.25	3.74	253.84	1.95	13.00	1.79	0.04
2.52	315.69	5.32	3.76	249.02	1.91	13.20	1.55	0.04
2.54	327.62	5.38	3.78	244.32	1.86	13.40	1.33	0.03
2.56	339.51	5.41	3.80	239.74	1.82	13.60	1.14	0.03
2.58	351.30	5.42	3.82	235.28	1.79	13.80	0.97	0.03
2.60	362.92	5.39	3.84	230.93	1.75	14.00	0.82	0.02
2.62	374.31	5.34	3.90	218.53	1.63	14.20	0.68	0.02
2.64	385.39	5.26	4.00	199.91	1.46	14.40	0.57	0.02
2.66	396.10	5.15	4.10	183.53	1.30	14.60	0.47	0.02
2.68	406.35	5.01	4.20	169.10	1.17	14.80	0.38	0.02
2.70	416.10	4.84	4.30	156.34	1.05	15.00	0.30	0.01
2.72	425.26	4.63	4.40	145.01	0.94	15.20	0.24	0.01
2.74	433.78	4.40	4.50	134.90	0.86	15.40	0.18	0.01
2.76	441.60	4.15	4.60	125.85	0.78	15.60	0.14	0.01
2.78	448.67	3.87	4.70	117.71	0.71	15.80	0.10	0.01

Table A.1 – continued from previous page

E_x	$P(E_x)$	$\Delta P(E_x)$	E_x	$P(E_x)$	$\Delta P(E_x)$	E_x	$P(E_x)$	$\Delta P(E_x)$
2.80	454.96	3.57	4.80	110.36	0.65	16.00	0.08	0.01
2.82	460.42	3.25	4.90	103.69	0.60	16.20	0.06	0.00
2.84	465.04	2.92	5.00	97.62	0.55	16.40	0.04	0.00
2.86	468.81	2.58	5.10	92.07	0.51	16.60	0.10	0.01
2.88	471.71	2.24	5.20	86.99	0.48	16.80	0.00	0.00
2.90	473.75	1.90	5.30	82.31	0.45			

Table A.2: The neutrino spectrum of ^{8}B and its uncertainties. Here $P(E_\nu)=dN/dE_\nu$ is the probability of a neutrino being emitted in a given energy range. The spectrum is normalized to 1000 when integrated in terms of MeV.

E_ν	$P(E_\nu)$	$\Delta P(E_\nu)$	E_ν	$P(E_\nu)$	$\Delta P(E_\nu)$	E_ν	$P(E_\nu)$	$\Delta P(E_\nu)$
0.10	0.21	0.02	5.30	123.75	0.20	10.50	65.75	-0.26
0.20	0.76	0.04	5.40	124.95	0.19	10.60	63.21	-0.26
0.30	1.51	0.01	5.50	126.04	0.18	10.70	60.67	-0.26
0.40	2.51	0.02	5.60	127.03	0.17	10.80	58.13	-0.26
0.50	3.76	0.03	5.70	127.91	0.16	10.90	55.61	-0.26
0.60	5.24	0.04	5.80	128.68	0.15	11.00	53.10	-0.25
0.70	6.91	0.05	5.90	129.35	0.14	11.10	50.60	-0.25
0.80	8.77	0.06	6.00	129.91	0.12	11.20	48.13	-0.25
0.90	10.80	0.08	6.10	130.37	0.11	11.30	45.69	-0.24
1.00	12.98	0.09	6.20	130.72	0.10	11.40	43.27	-0.24
1.10	15.29	0.10	6.30	130.96	0.09	11.50	40.89	-0.23
1.20	17.74	0.12	6.40	131.10	0.07	11.60	38.54	-0.23
1.30	20.29	0.13	6.50	131.13	0.06	11.70	36.24	-0.22
1.40	22.95	0.14	6.60	131.06	0.04	11.80	33.98	-0.22
1.50	25.70	0.16	6.70	130.89	0.02	11.90	31.77	-0.21
1.60	28.53	0.17	6.80	130.61	0.01	12.00	29.62	-0.20
1.70	31.43	0.18	6.90	130.23	-0.01	12.10	27.51	-0.19
1.80	34.39	0.20	7.00	129.75	-0.03	12.20	25.47	-0.19
1.90	37.40	0.21	7.10	129.17	-0.04	12.30	23.49	-0.18
2.00	40.45	0.22	7.20	128.50	-0.05	12.40	21.58	-0.17
2.10	43.53	0.23	7.30	127.72	-0.06	12.50	19.74	-0.17
2.20	46.64	0.24	7.40	126.86	-0.08	12.60	17.96	-0.16
2.30	49.77	0.25	7.50	125.89	-0.09	12.70	16.27	-0.15
2.40	52.90	0.26	7.60	124.84	-0.10	12.80	14.65	-0.14
2.50	56.04	0.27	7.70	123.70	-0.11	12.90	13.11	-0.13
2.60	59.17	0.27	7.80	122.47	-0.12	13.00	11.65	-0.12
2.70	62.30	0.28	7.90	121.16	-0.13	13.10	10.29	-0.12
2.80	65.40	0.28	8.00	119.76	-0.14	13.20	9.01	-0.11

E_ν	$P(E_\nu)$	$\Delta P(E_\nu)$	E_ν	$P(E_\nu)$	$\Delta P(E_\nu)$	E_ν	$P(E_\nu)$	$\Delta P(E_\nu)$
2.90	68.48	0.29	8.10	118.28	-0.15	13.30	7.81	-0.10
3.00	71.53	0.29	8.20	116.72	-0.16	13.40	6.71	-0.09
3.10	74.55	0.30	8.30	115.09	-0.17	13.50	5.70	-0.08
3.20	77.53	0.30	8.40	113.38	-0.17	13.60	4.79	-0.07
3.30	80.46	0.30	8.50	111.60	-0.19	13.70	3.96	-0.06
3.40	83.34	0.30	8.60	109.75	-0.19	13.80	3.24	-0.05
3.50	86.16	0.30	8.70	107.84	-0.20	13.90	2.60	-0.05
3.60	88.93	0.30	8.80	105.86	-0.21	14.00	2.06	-0.04
3.70	91.64	0.30	8.90	103.83	-0.22	14.10	1.60	-0.03
3.80	94.27	0.30	9.00	101.73	-0.22	14.20	1.23	-0.02
3.90	96.84	0.30	9.10	99.59	-0.23	14.30	0.93	-0.02
4.00	99.33	0.29	9.20	97.39	-0.23	14.40	0.69	-0.01
4.10	101.75	0.29	9.30	95.15	-0.24	14.50	0.51	-0.01
4.20	104.08	0.28	9.40	92.86	-0.24	14.60	0.38	-0.01
4.30	106.33	0.28	9.50	90.53	-0.25	14.70	0.27	-0.01
4.40	108.50	0.27	9.60	88.16	-0.25	14.80	0.20	-0.00
4.50	110.57	0.27	9.70	85.76	-0.25	14.90	0.14	-0.00
4.60	112.56	0.26	9.80	83.33	-0.26	15.00	0.10	-0.00
4.70	114.45	0.25	9.90	80.87	-0.26	15.10	0.07	-0.00
4.80	116.25	0.24	10.00	78.39	-0.26	15.20	0.05	-0.00
4.90	117.95	0.24	10.10	75.89	-0.26	15.30	0.03	-0.00
5.00	119.55	0.23	10.20	73.37	-0.26	15.40	0.02	-0.00
5.10	121.06	0.22	10.30	70.84	-0.26	15.50	0.01	-0.00
5.20	122.46	0.21	10.40	68.30	-0.26			

Table A.3: The positron spectrum of ^{8}B and its uncertainties. Here $P(E_\beta)=dN/dE_\beta$ is the probability of a positron being emitted in a given energy range, where E_β represents the total energy of the positron. The spectrum is normalized to 1000 when integrated in terms of MeV.

E_β	$P(E_\beta)$	$\Delta P(E_\beta)$	E_β	$P(E_\beta)$	$\Delta P(E_\beta)$	E_β	$P(E_\beta)$	$\Delta P(E_\beta)$
0.52	0.64	0.01	5.72	131.30	0.46	10.92	50.72	0.19
0.62	3.61	0.05	5.82	131.81	0.45	11.02	48.32	0.19
0.72	5.89	0.06	5.92	132.22	0.45	11.12	45.95	0.18
0.82	8.19	0.08	6.02	132.51	0.44	11.22	43.62	0.18
0.92	10.64	0.10	6.12	132.69	0.43	11.32	41.32	0.17
1.02	13.22	0.12	6.22	132.76	0.42	11.42	39.05	0.17
1.12	15.92	0.14	6.32	132.72	0.41	11.52	36.83	0.17
1.22	18.74	0.16	6.42	132.57	0.41	11.62	34.66	0.16
1.32	21.65	0.17	6.52	132.32	0.40	11.72	32.53	0.16
1.42	24.67	0.19	6.62	131.96	0.39	11.82	30.45	0.15
							Continued on next page	

E_β	$P(E_\beta)$	$\Delta P(E_\beta)$	E_β	$P(E_\beta)$	$\Delta P(E_\beta)$	E_β	$P(E_\beta)$	$\Delta P(E_\beta)$
1.52	27.76	0.21	6.72	131.49	0.38	11.92	28.43	0.15
1.62	30.92	0.23	6.82	130.93	0.37	12.02	26.46	0.14
1.72	34.15	0.25	6.92	130.26	0.36	12.12	24.56	0.14
1.82	37.42	0.27	7.02	129.49	0.35	12.22	22.71	0.14
1.92	40.74	0.29	7.12	128.63	0.34	12.32	20.93	0.13
2.02	44.08	0.31	7.22	127.67	0.34	12.42	19.22	0.12
2.12	47.44	0.32	7.32	126.61	0.33	12.52	17.57	0.12
2.22	50.81	0.34	7.42	125.47	0.32	12.62	16.00	0.11
2.32	54.19	0.35	7.52	124.24	0.31	12.72	14.50	0.11
2.42	57.56	0.37	7.62	122.92	0.30	12.82	13.07	0.10
2.52	60.92	0.38	7.72	121.52	0.30	12.92	11.73	0.09
2.62	64.26	0.40	7.82	120.04	0.29	13.02	10.45	0.09
2.72	67.57	0.41	7.92	118.48	0.28	13.12	9.26	0.08
2.82	70.85	0.42	8.02	116.84	0.28	13.22	8.15	0.08
2.92	74.09	0.44	8.12	115.14	0.27	13.32	7.12	0.07
3.02	77.28	0.45	8.22	113.36	0.26	13.42	6.17	0.06
3.12	80.41	0.46	8.32	111.51	0.26	13.52	5.30	0.06
3.22	83.49	0.47	8.42	109.60	0.25	13.62	4.51	0.05
3.32	86.51	0.47	8.52	107.63	0.25	13.72	3.79	0.05
3.42	89.46	0.48	8.62	105.60	0.25	13.82	3.16	0.04
3.52	92.33	0.49	8.72	103.52	0.24	13.92	2.60	0.04
3.62	95.13	0.49	8.82	101.39	0.24	14.02	2.11	0.03
3.72	97.85	0.50	8.92	99.20	0.23	14.12	1.69	0.03
3.82	100.49	0.50	9.02	96.98	0.23	14.22	1.34	0.02
3.92	103.04	0.51	9.12	94.71	0.23	14.32	1.04	0.02
4.02	105.49	0.51	9.22	92.40	0.22	14.42	0.80	0.01
4.12	107.85	0.51	9.32	90.06	0.22	14.52	0.61	0.01
4.22	110.12	0.51	9.42	87.68	0.22	14.62	0.45	0.01
4.32	112.29	0.51	9.52	85.28	0.22	14.72	0.33	0.01
4.42	114.35	0.51	9.62	82.86	0.22	14.82	0.25	0.00
4.52	116.31	0.51	9.72	80.41	0.21	14.92	0.18	0.00
4.62	118.17	0.51	9.82	77.95	0.21	15.02	0.13	0.00
4.72	119.92	0.51	9.92	75.47	0.21	15.12	0.09	0.00
4.82	121.56	0.51	10.02	72.98	0.21	15.22	0.06	0.00
4.92	123.09	0.50	10.12	70.49	0.21	15.32	0.04	0.00
5.02	124.51	0.50	10.22	67.99	0.20	15.42	0.03	0.00
5.12	125.82	0.50	10.32	65.49	0.20	15.52	0.02	0.00
5.22	127.01	0.49	10.42	63.00	0.20	15.62	0.01	0.00
5.32	128.10	0.49	10.52	60.51	0.20	15.72	0.01	0.00
5.42	129.07	0.48	10.62	58.04	0.20	15.82	0.01	0.00
5.52	129.93	0.47	10.72	55.58	0.19	15.92	0.00	0.00
5.62	130.67	0.47	10.82	53.14	0.19			